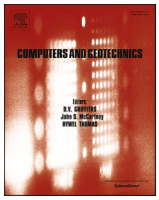
Computers and Geotechnics 202 (2027) 108632



Contents lists available at ScienceDirect

Computers and Geotechnics

journal homepage: www.elsevier.com/locate/compgeo



Research Paper

A physics-informed neural network (PINN) framework for inverse mixed contact-traction tire-load reconstruction and finite-layer pavement response

Dong Feng

Faculty of Civil Engineering, RWTH Aachen University, Mies-van-der-Rohe-Straße 1, 52074 Aachen, Germany

ARTICLE INFO

Keywords:
Physics-informed neural networks (PINNs)
Tire-contact traction
Inverse reconstruction
Dynamic pavement response
Three-dimensional finite elements

ABSTRACT

Tire-pavement interaction produces a spatially heterogeneous boundary traction that cannot be fully represented by uniform vertical pressure, particularly when braking, driving, or lateral slip generates appreciable tangential loading. Existing layered pavement models mainly address forward response prediction and provide limited capability for reconstructing unknown contact tractions and mechanically admissible transient subsurface fields from sparse observations. This study develops a physics-informed neural network (PINN) framework for inverse tire-contact traction reconstruction and dynamic finite-layer pavement response. The tire footprint is represented by a total normal contact pressure and longitudinal and lateral traction components, without imposing a mechanically unidentifiable decomposition of the normal pressure. A three-dimensional transient finite-element reference model provides mechanics-consistent displacement, stress, strain, reaction, and strain-energy fields under a time-dependent moving load. These fields are coupled with neural reconstruction through dynamic equilibrium, constitutive, boundary, interface, force-closure, initial-condition, and regularization constraints. Source realizations are partitioned before training, and held-out contact fields are reconstructed from sparse displacement and stress histories without including their prescribed source values in the inverse loss. The framework therefore provides a unified differentiable setting for contact-traction identification, transient pavement-response reconstruction, source-disjoint evaluation, stability assessment, domain transfer, and robustness analysis.

1. Introduction

Tire-pavement interaction is one of the primary mechanical sources governing the structural performance, serviceability, and long-term deterioration of road infrastructure (Hernandez and Al-Qadi, 2017; Zhao et al., 2024; Michael et al., 2015). When a tire load is transmitted to the pavement surface, a highly localized boundary action is generated and subsequently propagated through the asphalt courses, base layer, sub-base, and subgrade (Rahman et al., 2025; Luo et al., 2025; Liu et al., 2024). The resulting stress and strain fields control many critical mechanical responses, including vertical compressive stress, horizontal tensile strain, shear transfer, surface deflection, interface stress concentration, and strain-energy accumulation (Wang et al., 2022; Behnke and Kaliske, 2015; Zhao and Wang, 2022). For this reason, layered pavement mechanics has long relied on analytical solutions (Feng, 2025; Feng, 2026), semi-analytical formulations (Shen and Wang, 2024), finite-element (FE) models (Feng, 2025; Feng et al., 2026), discrete element (DE) models (Feng et al., 2026; Feng et al., 2026), alternative models (Feng, 2026; Feng, 2026), and multilayer elastic theories (Ma et al., 2021; Feng, 2026) to evaluate pavement response under repeated loading. These approaches have provided important insight into stress diffusion, load-bearing mechanisms, and the contribution of individual layers to the overall structural response. In particular, they have clarified how the stiffness contrast between asphalt layers and foundation layers affects the depthwise attenuation of stress (Sadiq et al., 2025), the spread of the load-induced deformation field (Huang et al., 2025), and the concentration of shear or tensile response near material interfaces (Nian et al., 2023). However, the reliability of such predictions depends strongly on how the tire-contact boundary source is represented (Yun et al., 2026; Wollny et al., 2016). This is especially critical for near-surface response, where pressure gradients, tread-induced modulation, surface-condition effects, and tangential forces may create localized stress concentrations that cannot be captured by a simple uniform vertical-load assumption.

The contact action between a tire and a pavement surface is intrinsically heterogeneous and multicomponent (Gong et al., 2024; Lee et al., 2013). Even under nominally steady rolling conditions, the normal contact

E-mail address: dong.feng@rwth-aachen.de.

https://doi.org/10.1016/j.compgeo.2026.108632
Received 12 June 2026; Received in revised form 4 September 2026; Accepted 5 September 2026
Available online 12 September 2026
0266-352X/© 2026 The Author(s). Published by Elsevier Ltd. This is an open access article under the CC BY license (http://creativecommons.org/licenses/by/4.0/).

pressure may be non-uniform because of tire carcass deformation, tread geometry, inflation state, wheel load, contact-patch shape, pavement roughness, and surface condition (Park et al., 2005; Behroozinia et al., 2020). Braking, driving, steering, and lateral slip additionally generate longitudinal and lateral tractions that interact with the normal pressure field (Dehnad and Yazdi, 2024; Löwer et al., 2020). Within a single-phase solid-mechanics formulation, however, the subsurface response is governed by the total mechanically transmitted normal pressure (Deng et al., 2025; Fwa, 2021). These normal and tangential components jointly determine the vertical stress bulb, radial and circumferential stresses, shear stress, mean compressive stress, von Mises stress, displacement field, and strain-energy density (Guan et al., 2022; Wang et al., 2024). Their influence is not confined to the surface. Instead, the mixed boundary source modifies how stress propagates downward, how shear is transferred across interfaces, and how deformation localizes in layers with different stiffness levels (Rasol et al., 2021; Zheng et al., 2022). Therefore, a mechanically meaningful pavement response model should describe not only the layered continuum beneath the tire, but also the mixed tire-contact traction field acting on the contact surface.

Despite the maturity of analytical, semi-analytical, and FE approaches, recent advances in data-driven modeling have introduced new possibilities for pavement simulation and response prediction (Feng, 2026; Feng et al., 2026). Machine-learning methods, including surrogate modeling, neural networks, Gaussian-process regression, ensemble learning, and graph-based models, have been increasingly used to approximate pavement responses (Cano-Ortiz et al., 2022; Shahid et al., 2026), accelerate parametric analysis (Mizutani et al., 2026; Bruno et al., 2022), identify material or structural patterns (Xu et al., 2024; Stefanelli et al., 2026), and predict stress, strain, deflection, rutting, or fatigue-related indicators from multi-source inputs (Xu et al., 2025; Wu et al., 2014). Recent studies have also investigated related geotechnical problems, including soil parameter identification, consolidation analysis, and subsurface characterization, further demonstrating the growing interest in data-assisted mechanics and inverse analysis for complex engineering systems (Xie et al., 2026; Xie et al., 2024; Xie et al., 2026). Computational approaches have also been increasingly applied to reconstruct complex material structures and quantify the effects of spatial variability in geotechnical systems (Feng, 2027; Jia et al., 2026; Wang et al., 2026). Related advances in intelligent sensing, multi-view perception, spatial localization, and multimodal information fusion have further demonstrated the capability of data-driven computational methods to extract and integrate complex spatial information in engineering environments (Lv et al., 2025; Yang et al., 2025; Yao et al., 2026). Meanwhile, advanced numerical frameworks have facilitated the analysis of coupled mechanical responses and complex load-transfer mechanisms in geomaterials (Liu et al., 2026; Bao et al., 2026). More broadly, intelligent computational frameworks have also been incorporated into automated design, information integration, and collaborative engineering workflows, illustrating the expanding role of algorithm-assisted methods in complex engineering applications (Chen et al., 2023, 2025). These developments indicate that learning-based models can complement conventional mechanics models when the response space is high-dimensional or when repeated FE simulations are computationally expensive. However, most learning-based pavement models still rely on prescribed input loads and output-oriented fitting, while the unknown tire-contact source is rarely reconstructed as a mechanically constrained field (Fahad and Bektas, 2025; Abd El-Hakim et al., 2025). Purely data-driven predictions may also satisfy statistical accuracy but violate equilibrium, constitutive consistency, traction balance, interface continuity, symmetry requirements, or global force closure (Sheng et al., 2025; Justo-Silva et al., 2021). This limitation becomes more critical for finite-layer pavements under non-uniform normal and tangential tire loading, where the effects of the total normal pressure, longitudinal traction, and lateral traction propagate through the layers with strong stiffness contrast and may generate fully three-dimensional transient responses (Liu et al., 2021; Mirzaiyan et al., 2025). Therefore, a unified inverse framework is required to combine the flexibility of machine learning with the governing constraints of continuum mechanics, so that the boundary source and the depth-resolved pavement response can be reconstructed in a physically admissible and generalizable manner.

This study develops a physics-informed neural network (PINN) (Raissi et al., 2019) framework for inverse tire-contact traction reconstruction and dynamic finite-layer pavement response. As summarized in Fig. 1, the tire-contact boundary is represented by a total normal pressure, a longitudinal traction, and a lateral traction over the footprint. These components act on a three-dimensional finite-layer pavement domain governed by small-strain elasticity, dynamic equilibrium, boundary conditions, initial conditions, and layer-interface compatibility. A three-dimensional transient FE model provides mechanically admissible displacement, stress, strain, strain-energy, and reaction histories under a moving contact load. Sparse observations extracted from these histories are embedded into a PINN inverse model through a composite loss containing data mismatch, dynamic-equilibrium residuals, constitutive residuals, boundary-traction residuals, interface residuals, force closure, and regularization. Source realizations are separated before training so that held-out contact fields are reconstructed without using their source labels in the inverse loss. The reconstructed outputs include the contact-traction field and the depth- and time-resolved pavement response. The main contribution is therefore a mechanics-constrained inverse pipeline that combines three-dimensional transient FE reference mechanics, source-disjoint reconstruction, and physics-informed learning in a unified computational framework.

2. Methodology

The proposed methodology is organized as a coupled mechanics-learning framework for reconstructing mixed tire-contact tractions and predicting the transient response of a finite-layer pavement. The formulation first defines a three-dimensional layered continuum subjected to heterogeneous normal and tangential surface tractions. A transient FE reference model is then constructed to provide mechanically admissible displacement, stress, strain, reaction, and strain-energy histories under a moving contact load. On this basis, a physics-informed inverse model is formulated to infer the unknown contact-traction field and the associated internal response from sparse observations and governing-equation constraints. Source realizations are partitioned before model training so that the reconstruction of held-out sources is evaluated without exposing their contact-field labels to the inverse loss. Finally, the reconstruction operator is extended to scenario-dependent loading and material states, allowing dynamic transfer, stability, generalization, and robustness to be assessed within the same computational setting.

2.1. Finite-layer pavement mechanics and mixed tire-contact traction

The first component establishes the governing continuum description of the finite-layer pavement and its tire-contact boundary traction. The pavement is treated as a three-dimensional layered elastic body, where each layer may have distinct mechanical properties and adjacent layers exchange displacement and traction through bonded interfaces. The tire-pavement interaction is represented by a mixed surface traction containing a total normal pressure and two tangential traction components. This formulation provides a consistent basis for the transient FE reference solution and for inverse reconstruction of the complete contact-traction vector.

Let $\Omega \subset \mathbb{R}^3$ denote a finite-layer pavement domain. The spatial coordinate is $\mathbf{x} = (x, y, z)^{\mathrm{T}}$, where x and y are horizontal coordinates and z is the depth coordinate measured from the road surface. The upper boundary is denoted by Γ_t, the tire-contact region by $\Gamma_c \subset \Gamma_t$, the lateral boundary by Γ_s, the bottom boundary by Γ_b, and the interface between adjacent layers by $\Gamma_I^{(\ell)}$. The layer index is ℓ, and the corresponding subdomain is Ω_ℓ. The displacement vector is $\mathbf{u} = (u_x, u_y, u_z)^{\mathrm{T}}$, the Cauchy stress tensor is $\boldsymbol{\sigma}$, and the infinitesimal strain tensor is $\boldsymbol{\varepsilon}$.

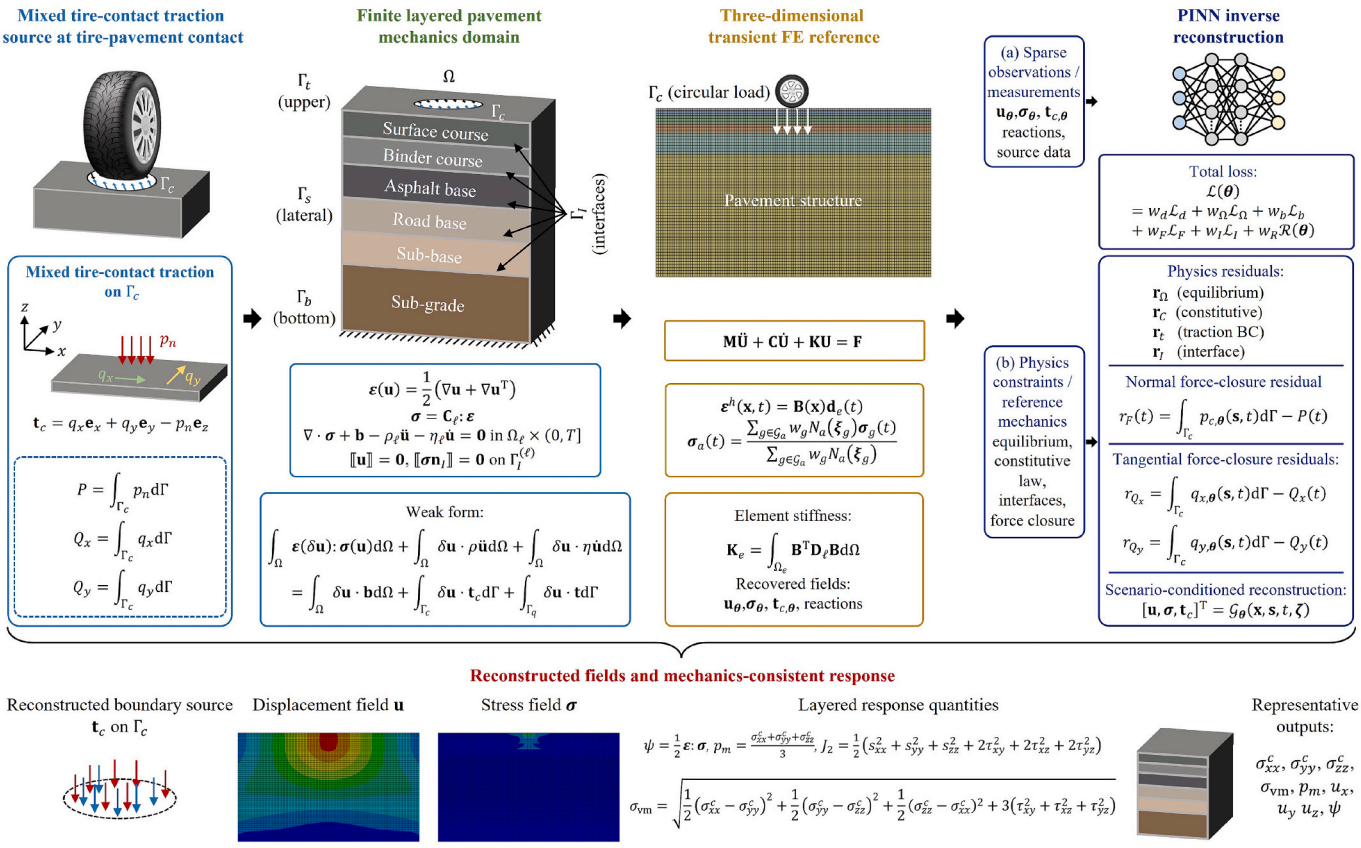


Fig. 1. Conceptual framework of the physics-informed inverse tire-contact traction reconstruction and dynamic finite-layer pavement response model.

The small-strain kinematics are defined as:

$$\boldsymbol{\varepsilon}(\mathbf{u}) = \frac{1}{2}(\nabla\mathbf{u} + \nabla\mathbf{u}^T) = \begin{bmatrix} \frac{\partial u_x}{\partial x} & \frac{1}{2}\left(\frac{\partial u_x}{\partial y} + \frac{\partial u_y}{\partial x}\right) & \frac{1}{2}\left(\frac{\partial u_x}{\partial z} + \frac{\partial u_z}{\partial x}\right) \\ \frac{1}{2}\left(\frac{\partial u_y}{\partial x} + \frac{\partial u_x}{\partial y}\right) & \frac{\partial u_y}{\partial y} & \frac{1}{2}\left(\frac{\partial u_y}{\partial z} + \frac{\partial u_z}{\partial y}\right) \\ \frac{1}{2}\left(\frac{\partial u_z}{\partial x} + \frac{\partial u_x}{\partial z}\right) & \frac{1}{2}\left(\frac{\partial u_z}{\partial y} + \frac{\partial u_y}{\partial z}\right) & \frac{\partial u_z}{\partial z} \end{bmatrix}. \tag{1}$$

Each pavement layer is modeled as a linear isotropic elastic material. Young's modulus and Poisson's ratio of layer ℓ are E_ℓ and ν_ℓ, respectively. The fourth-order elasticity tensor is $\mathbf{C}_\ell$. The constitutive relation is:

$$\boldsymbol{\sigma} = \mathbf{C}_\ell : \boldsymbol{\varepsilon}, \mathbf{x} \in \Omega_\ell. \tag{2}$$

In Voigt notation, the three-dimensional stress–strain law is:

$$\begin{bmatrix} \sigma_{xx} \\ \sigma_{yy} \\ \sigma_{zz} \\ \sigma_{yz} \\ \sigma_{xz} \\ \sigma_{xy} \end{bmatrix} = \frac{E_\ell}{(1+\nu_\ell)(1-2\nu_\ell)} \begin{bmatrix} 1-\nu_\ell & \nu_\ell & \nu_\ell & 0 & 0 & 0 \\ \nu_\ell & 1-\nu_\ell & \nu_\ell & 0 & 0 & 0 \\ \nu_\ell & \nu_\ell & 1-\nu_\ell & 0 & 0 & 0 \\ 0 & 0 & 0 & \frac{1-2\nu_\ell}{2} & 0 & 0 \\ 0 & 0 & 0 & 0 & \frac{1-2\nu_\ell}{2} & 0 \\ 0 & 0 & 0 & 0 & 0 & \frac{1-2\nu_\ell}{2} \end{bmatrix} \begin{bmatrix} \varepsilon_{xx} \\ \varepsilon_{yy} \\ \varepsilon_{zz} \\ \gamma_{yz} \\ \gamma_{xz} \\ \gamma_{xy} \end{bmatrix}, \tag{3}$$

where $\gamma_{ij} = 2\varepsilon_{ij}$ is the engineering shear strain. The transient momentum-balance equation in layer ℓ is:

$$\nabla\cdot\boldsymbol{\sigma} + \mathbf{b} - \rho_\ell\ddot{\mathbf{u}} - \eta_\ell\dot{\mathbf{u}} = 0 \text{ in } \Omega_\ell \times (0,T], \tag{4}$$

where $\mathbf{b}$ is the body force vector, ρ_ℓ is the material density of layer ℓ, η_ℓ is an effective viscous damping coefficient, and the superposed dots denote time derivatives. The damping term provides a compact representation of dissipative effects while retaining the original linear-elastic constitutive law.

The mixed tire-contact traction acting on Γ_c is:

$$\mathbf{t}_c(x,y,t) = q_x(x,y,t)\mathbf{e}_x + q_y(x,y,t)\mathbf{e}_y - p_n(x,y,t)\mathbf{e}_z, (x,y) \in \Gamma_c, \tag{5}$$

where p_n is the total normal contact pressure, q_x is the longitudinal traction, q_y is the lateral traction, and $\mathbf{e}_x$, $\mathbf{e}_y$, and $\mathbf{e}_z$ are the Cartesian basis vectors. The total vertical load and tangential resultants are:

$$P(t) = \int_{\Gamma_c} p_n \mathrm{d}\Gamma,$$
$$Q_x(t) = \int_{\Gamma_c} q_x \mathrm{d}\Gamma, \tag{6}$$
$$Q_y(t) = \int_{\Gamma_c} q_y \mathrm{d}\Gamma.$$

Introducing an admissible virtual displacement $\delta\mathbf{u}$, the dynamic weak form becomes:

$$\int_\Omega \boldsymbol{\varepsilon}(\delta\mathbf{u}) : \boldsymbol{\sigma}(\mathbf{u})\mathrm{d}\Omega + \int_\Omega \delta\mathbf{u}\cdot\rho\ddot{\mathbf{u}}\mathrm{d}\Omega + \int_\Omega \delta\mathbf{u}\cdot\eta\dot{\mathbf{u}}\mathrm{d}\Omega = \int_\Omega \delta\mathbf{u}\cdot\mathbf{b}\mathrm{d}\Omega + \int_{\Gamma_c} \delta\mathbf{u}\cdot\mathbf{t}_c\mathrm{d}\Gamma + \int_{\Gamma_q} \delta\mathbf{u}\cdot\mathbf{t}\mathrm{d}\Gamma \tag{7}$$

where Γ_q is a prescribed-traction boundary. At a bonded layer interface, displacement continuity and traction equilibrium are imposed as:

$$[\![\mathbf{u}]\!] = 0, [\![\boldsymbol{\sigma}\mathbf{n}_I]\!] = 0 \text{ on } \Gamma_I^{(\swarrow)}, \tag{8}$$

where $\mathbf{n}_I$ is the interface normal vector and $[\![\cdot]\!]$ denotes the jump operator across the interface. The transient problem is completed by the initial conditions $\mathbf{u}(\mathbf{x},0) = \mathbf{u}_0(\mathbf{x})$ and $\dot{\mathbf{u}}(\mathbf{x},0) = \mathbf{v}_0(\mathbf{x})$.

2.2. Three-dimensional transient finite-element reference field

The second component constructs a three-dimensional transient FE reference field that serves as the mechanics-resolved baseline for the inverse framework. The three-dimensional formulation is required because longitudinal and lateral contact tractions generate non-axisymmetric stress, displacement, and wave-propagation patterns. The reference model therefore resolves all three displacement components and all six independent stress components over time, while retaining the original finite-layer pavement geometry and bonded layer interfaces.

The transient FE solution supplies equilibrium-consistent displacement, velocity, acceleration, strain, stress, reaction, and strain-energy histories. These quantities are used to generate sparse observation histories, evaluate global force closure, and assess the reconstructed PINN fields. For source-disjoint test cases, the complete reference traction and the unobserved FE fields are withheld from the inverse reconstruction and are used only for subsequent error evaluation.

Within a three-dimensional finite element e, the displacement field is approximated by interpolating the time-dependent nodal degrees of freedom through the element shape functions. The resulting discrete displacement representation is written as:

$$\mathbf{u}^h(\mathbf{x},t) = \mathbf{N}(\mathbf{x})\mathbf{d}_e(t), \tag{9}$$

where $\mathbf{N}$ is the three-dimensional displacement shape-function matrix and $\mathbf{d}_e$ contains the nodal displacement degrees of freedom of element e.

The corresponding infinitesimal strain field is obtained by applying the three-dimensional differential operator to the interpolated displacement field. Introducing the strain–displacement matrix $\mathbf{B}$, the discrete strain relation becomes:

$$\boldsymbol{\varepsilon}^h(\mathbf{x},t) = \mathbf{B}(\mathbf{x})\mathbf{d}_e(t), \quad \mathbf{B} = \mathbf{L}\mathbf{N}, \tag{10}$$

where $\mathbf{L}$ is the three-dimensional differential operator containing the spatial derivatives required to construct the normal and engineering shear strains.

To account for the inertia of each pavement layer, the consistent element mass matrix is obtained by weighting the displacement interpolation with the layer density. It is defined as:

$$\mathbf{M}_e = \int_{\Omega_e} \mathbf{N}^{\mathrm{T}}\rho_{\swarrow}\mathbf{N}\mathrm{d}\Omega. \tag{11}$$

The dissipative contribution introduced in the dynamic governing equation is discretized in an analogous manner. Using the effective viscous damping coefficient of layer $\swarrow$, the element damping matrix is expressed as:

$$\mathbf{C}_e = \int_{\Omega_e} \mathbf{N}^{\mathrm{T}}\eta_{\swarrow}\mathbf{N}\mathrm{d}\Omega. \tag{12}$$

Because a mass-proportional damping representation is adopted, the corresponding equivalent modal damping ratio is frequency dependent and may be expressed as $\xi_l(f) = \alpha_l/(4\pi f)$, where f is the response frequency. Accordingly, α_l is interpreted here as an effective transient dissipation parameter selected with reference to the characteristic frequency range of the moving tire load, rather than as a frequency-independent intrinsic material damping ratio.

The elastic resistance of the finite element is determined from the strain–displacement relation and the three-dimensional constitutive matrix. Accordingly, the element stiffness matrix is evaluated as:

$$\mathbf{K}_e = \int_{\Omega_e} \mathbf{B}^{\mathrm{T}}\mathbf{D}_{\swarrow}\mathbf{B}\mathrm{d}\Omega, \tag{13}$$

where $\mathbf{D}_{\swarrow}$ is the three-dimensional elastic constitutive matrix of layer $\swarrow$.

For a footprint moving at a prescribed velocity, its center and associated traction distribution are defined by:

$$\mathbf{x}_L = \mathbf{x}_0 + \mathbf{v}_L t, \quad \mathbf{t}_c(\mathbf{x}_\parallel, t) = \bar{\mathbf{t}}_c(\mathbf{x}_\parallel - \mathbf{x}_L(t)), \tag{14}$$

where $\mathbf{x}_\parallel = (x,y)^{\mathrm{T}}$ is the pavement-surface coordinate, $\mathbf{x}_0$ is the initial footprint center, $\mathbf{v}_L$ is the prescribed load velocity, and $\bar{\mathbf{t}}_c$ denotes the traction distribution expressed in the local footprint coordinate system.

At each time instant, the moving contact traction is converted into an equivalent element nodal-force vector over the portion of the element boundary intersected by the footprint. The contact-force contribution of element e is therefore:

$$\mathbf{f}_e^c(t) = \int_{\Gamma_{c,e}} \mathbf{N}^{\mathrm{T}}\mathbf{t}_c(\mathbf{x}_\parallel, t)\mathrm{d}\Gamma, \tag{15}$$

where $\Gamma_{c,e}$ denotes the part of the tire-contact boundary associated with element e. Because the integration domain and traction values vary as the footprint moves, $\mathbf{f}_e^c$ is explicitly time dependent.

After assembling the element mass, damping, stiffness, and external-force contributions over the full three-dimensional pavement domain, the semi-discrete transient FE system is obtained as:

$$\mathbf{M}\ddot{\mathbf{U}}(t) + \mathbf{C}\dot{\mathbf{U}}(t) + \mathbf{K}\mathbf{U}(t) = \mathbf{F}(t), \tag{16}$$

where $\mathbf{M}$, $\mathbf{C}$, and $\mathbf{K}$ are the assembled global mass, damping, and stiffness matrices, respectively; $\mathbf{U}(t)$, $\dot{\mathbf{U}}(t)$, and $\ddot{\mathbf{U}}(t)$ are the global displacement, velocity, and acceleration vectors; and $\mathbf{F}(t)$ is the time-dependent global external-force vector.

The dynamic reactions and equilibrium imbalance are evaluated by substituting the calculated nodal response into the assembled equation of motion. The resulting residual vector is written as:

$$\mathbf{R}(t) = \mathbf{M}\ddot{\mathbf{U}}(t) + \mathbf{C}\dot{\mathbf{U}}(t) + \mathbf{K}\mathbf{U}(t) - \mathbf{F}(t), \tag{17}$$

where the entries of $\mathbf{R}(t)$ associated with constrained degrees of freedom provide the dynamic support reactions, whereas the entries associated with free degrees of freedom quantify the numerical equilibrium residual.

The global transient system is advanced in time using the Newmark integration scheme. The displacement and velocity at time t_{n+1} are related to the response quantities at t_n through:

$$\mathbf{U}_{n+1} = \mathbf{U}_n + \Delta t\dot{\mathbf{U}}_n + \Delta t^2\left[\left(\frac{1}{2}-\beta\right)\ddot{\mathbf{U}}_n + \beta\ddot{\mathbf{U}}_{n+1}\right],$$
$$\dot{\mathbf{U}}_{n+1} = \dot{\mathbf{U}}_n + \Delta t\left[(1-\gamma)\ddot{\mathbf{U}}_n + \gamma\ddot{\mathbf{U}}_{n+1}\right]. \tag{18}$$

The standard average-acceleration choice, $\beta = \frac{1}{4}$ and $\gamma = \frac{1}{2}$, provides an unconditionally stable integration scheme for the linear transient problem considered here.

The stresses initially evaluated at element integration points are subsequently projected to the finite-element nodes to facilitate field comparison, visualization, and extraction of sparse observation data. Using weighted nodal averaging, the stress assigned to node a is calculated as:

$$\boldsymbol{\sigma}_a(t) = \frac{\sum_{g\in\mathcal{G}_a} w_g N_a(\boldsymbol{\xi}_g)\boldsymbol{\sigma}_g(t)}{\sum_{g\in\mathcal{G}_a} w_g N_a(\boldsymbol{\xi}_g)}, \tag{19}$$

where $\mathcal{G}_a$ is the set of integration points contributing to node a, $N_a(\boldsymbol{\xi}_g)$ is the nodal shape function evaluated at integration point g, and w_g contains the corresponding quadrature weight and Jacobian determinant. The same projection procedure is applied to the strain and strain-energy–density fields.

For the repeated material-parameter re-evaluations required in the subsequent diagnostic analyses, a reduced-order FE representation was additionally constructed from the free-DOF displacement snapshots of the full-order response library. The column-normalized snapshot matrix was decomposed by singular value decomposition, and the first N_{ROM} left singular vectors were retained as the reduced projection basis, where N_{ROM} denotes the dimension of the reduced FE basis; this reduced representation was used only for repeated diagnostic re-evaluations, whereas the reference fields and training data were generated using the full three-dimensional transient FE model.

For pavement-response interpretation, compressive-positive normal stresses are defined as $\sigma^c_{xx} = -\sigma_{xx}$, $\sigma^c_{yy} = -\sigma_{yy}$, and $\sigma^c_{zz} = -\sigma_{zz}$, whereas the shear components τ_{xy}, τ_{xz}, and τ_{yz} retain their original signs. The three-dimensional reference field therefore supplies $\mathbf{u}$, $\dot{\mathbf{u}}$, $\ddot{\mathbf{u}}$, $\boldsymbol{\varepsilon}$, $\boldsymbol{\sigma}$, all normal and shear stress components, stress invariants, vertical strain, strain-energy density, applied traction resultants, dynamic reactions, and time-dependent closure measures required by the inverse model. In addition, parameters not specifically described in this section are provided in Appendix B.

2.3. PINN-based inverse reconstruction and loss structure

The third component introduces the physics-informed neural reconstruction model. The inverse problem seeks a differentiable operator that maps space–time coordinates and footprint coordinates to the reconstructed displacement field, stress field, and tire-contact traction. As shown in Fig. 2, unlike a purely data-driven surrogate, the model is constrained by three-dimensional dynamic equilibrium, the layerwise constitutive relation, time-dependent traction boundary conditions, interface compatibility, and global force closure. These constraints are embedded into a composite loss together with sparse observation mismatch and regularization terms. The resulting formulation allows incomplete response histories to guide reconstruction while excluding mechanically inadmissible solutions.

The PINN approximation is introduced as a differentiable inverse reconstruction operator that maps the spatial coordinate in the pavement body, the footprint coordinate on the contact boundary, and time to the reconstructed displacement field, stress field, and tire-contact traction field. Let $\boldsymbol{\theta}$ denote the trainable parameter vector of the neural representation. The reconstruction operator is defined as:

$$\mathcal{G}_{\boldsymbol{\theta}}(\mathbf{x},\mathbf{s},t) = \begin{bmatrix} \mathbf{u}_{\boldsymbol{\theta}}(\mathbf{x},t) \\ \boldsymbol{\sigma}_{\boldsymbol{\theta}}(\mathbf{x},t) \\ \mathbf{t}_{c,\boldsymbol{\theta}}(\mathbf{s},t) \end{bmatrix}, \mathbf{x}\in\Omega,\ \mathbf{s}\in\Gamma_c. \tag{20}$$

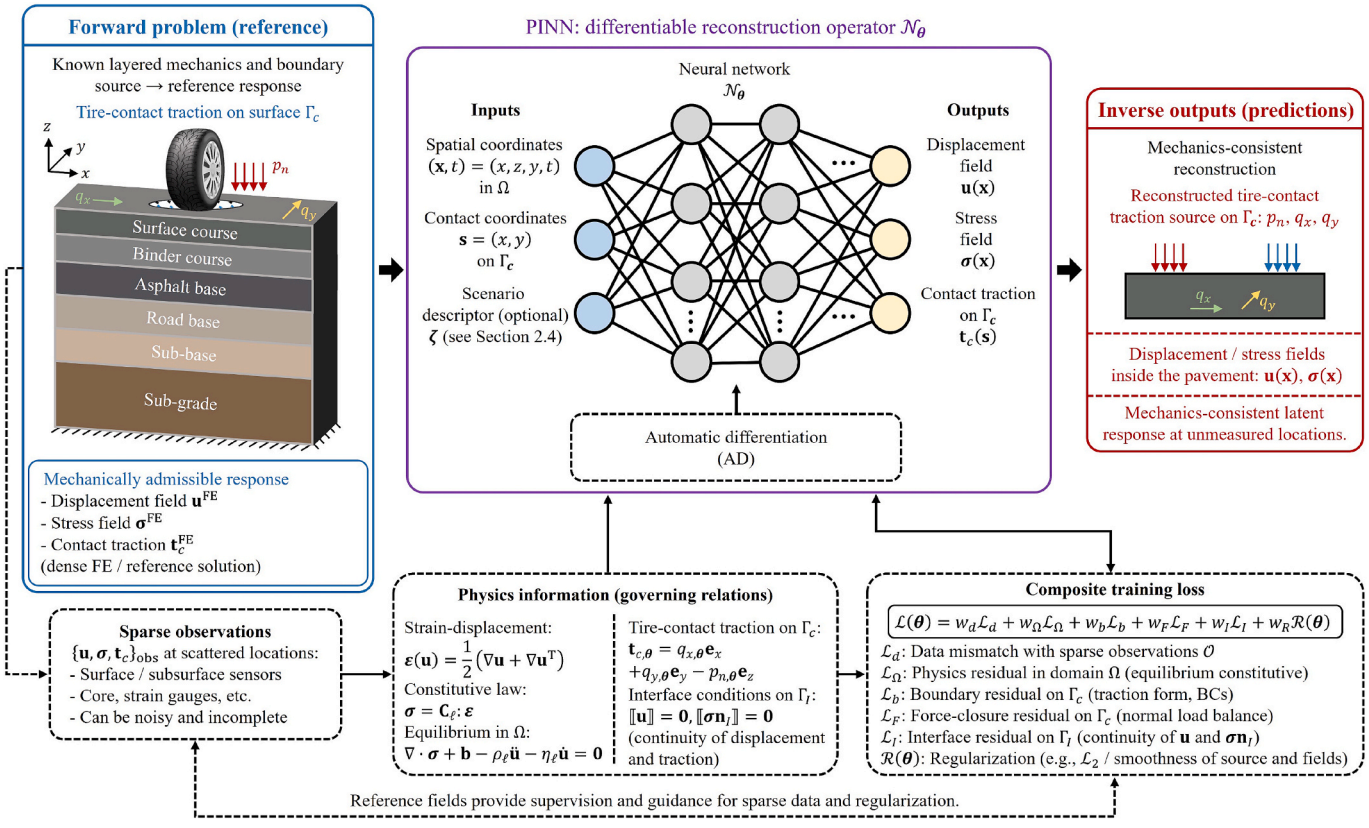


Fig. 2. Mechanics-constrained inverse PINN for 3D transient tire-contact traction reconstruction.

This definition makes the inverse problem explicit: the network not only approximates an internal pavement response but also reconstructs the boundary-source field that generates that response. The reconstructed mixed contact-traction source is:

$$\mathbf{t}_{c,\theta} = q_{x,\theta}\mathbf{e}_x + q_{y,\theta}\mathbf{e}_y - p_{n,\theta}\mathbf{e}_z. \tag{21}$$

The governing-equation residual is:

$$\mathbf{r}_\Omega = \nabla\cdot\boldsymbol{\sigma}_\theta + \mathbf{b} - \rho_l\frac{\partial^2\mathbf{u}_\theta}{\partial t^2} - \eta_l\frac{\partial\mathbf{u}_\theta}{\partial t}. \tag{22}$$

The constitutive residual is:

$$\mathbf{r}_C = \boldsymbol{\sigma}_\theta - \mathbf{C}_{\diagup} : \boldsymbol{\varepsilon}(\mathbf{u}_\theta), \mathbf{x} \in \Omega_{\diagup}. \tag{23}$$

The three-dimensional dynamic-equilibrium residuals are:

$$\begin{aligned} r_x &= \frac{\partial\sigma_{xx}}{\partial x} + \frac{\partial\sigma_{xy}}{\partial y} + \frac{\partial\sigma_{xz}}{\partial z} + b_x - \rho_l\frac{\partial^2 u_x}{\partial t^2} - \eta_l\frac{\partial u_x}{\partial t}, \\ r_y &= \frac{\partial\sigma_{xy}}{\partial x} + \frac{\partial\sigma_{yy}}{\partial y} + \frac{\partial\sigma_{yz}}{\partial z} + b_y - \rho_l\frac{\partial^2 u_y}{\partial t^2} - \eta_l\frac{\partial u_y}{\partial t}, \\ r_z &= \frac{\partial\sigma_{xz}}{\partial x} + \frac{\partial\sigma_{yz}}{\partial y} + \frac{\partial\sigma_{zz}}{\partial z} + b_z - \rho_l\frac{\partial^2 u_z}{\partial t^2} - \eta_l\frac{\partial u_z}{\partial t}. \end{aligned} \tag{24}$$

The boundary-source residual is:

$$\mathbf{r}_t = \boldsymbol{\sigma}_\theta\mathbf{n} - \mathbf{t}_{c,\theta}\text{on}\,\Gamma_c, \tag{25}$$

where $\mathbf{n}$ is the outward unit normal vector on Γ_c.

The normal force-closure residual is:

$$r_F(t) = \int_{\Gamma_c} p_{n,\theta}(\mathbf{s},t)\mathrm{d}\Gamma - \widetilde{P}(t). \tag{26}$$

The tangential force-closure residuals are:

$$\begin{aligned} r_{Q_x}(t) &= \int_{\Gamma_c} q_{x,\theta}(\mathbf{s},t)\mathrm{d}\Gamma - \widetilde{Q}_x(t), \\ r_{Q_y}(t) &= \int_{\Gamma_c} q_{y,\theta}(\mathbf{s},t)\mathrm{d}\Gamma - \widetilde{Q}_y(t). \end{aligned} \tag{27}$$

The interface residual is:

$$\mathbf{r}_I = \begin{bmatrix} [\![\mathbf{u}_\theta]\!] \\ [\![\boldsymbol{\sigma}_\theta\mathbf{n}_I]\!] \end{bmatrix}\text{on}\,\Gamma_I^{(\diagup)}. \tag{28}$$

The quantities $\widetilde{P}(t)$, $\widetilde{Q}_x(t)$, and $\widetilde{Q}_y(t)$ in Eqs. (26) and (27) denote independently observed global wheel-force resultants rather than the exact resultants calculated from the withheld target traction field. In the blind test, these quantities are supplied with measurement uncertainty and therefore act as soft integral constraints rather than prescribed source labels. The information available to the inverse model consists of the sparse displacement and stress histories, the independently known moving speed, contact radius, and material-domain state, and the measured global force resultants. In contrast, the complete spatial fields $p_{n,\theta}(\mathbf{s},t)$, $q_{x,\theta}(\mathbf{s},t)$, and $q_{y,\theta}(\mathbf{s},t)$, their exact source coefficients, and the exact force resultants of the reference solution are withheld and used only for post-reconstruction evaluation. Four source coefficients are estimated for each blind realization; three are softly constrained by the measured normal and tangential resultants, whereas the coefficient controlling normal-pressure heterogeneity has no direct global-resultant observation.

Let $\mathscr{D}_u$ and $\mathscr{D}_\sigma$ be observation sets for displacement and stress, respectively. The data mismatch loss $\mathscr{L}_d$ is:

$$\mathscr{L}_d = \frac{1}{|\mathscr{D}_u|}\sum_{(\mathbf{x}_i,t_i)\in\mathscr{D}_u}\|\mathbf{u}_\theta(\mathbf{x}_i,t_i) - \mathbf{u}_i^{\text{obs}}\|_2^2 + \frac{1}{|\mathscr{D}_\sigma|}\sum_{(\mathbf{x}_j,t_j)\in\mathscr{D}_\sigma}\|\boldsymbol{\sigma}_\theta(\mathbf{x}_j,t_j) - \boldsymbol{\sigma}_j^{\text{obs}}\|_2^2. \tag{29}$$

The physics loss $\mathscr{L}_\Omega$ is:

$$\mathscr{L}_\Omega = \frac{1}{|\mathscr{C}_\Omega|}\sum_{(\mathbf{x}_k,t_k)\in\mathscr{C}_\Omega}\|\mathbf{r}_\Omega(\mathbf{x}_k,t_k)\|_2^2 + \frac{1}{|\mathscr{C}_C|}\sum_{(\mathbf{x}_k,t_k)\in\mathscr{C}_C}\|\mathbf{r}_C(\mathbf{x}_k,t_k)\|_2^2, \tag{30}$$

where $\mathscr{C}_\Omega$ and $\mathscr{C}_C$ are collocation sets. The boundary loss $\mathscr{L}_b$, force-closure loss $\mathscr{L}_F$, and interface loss $\mathscr{L}_I$ are:

$$\mathscr{L}_b = \frac{1}{|\mathscr{C}_b|}\sum_{(\mathbf{s}_m,t_m)\in\mathscr{C}_b}\|\mathbf{r}_t(\mathbf{s}_m,t_m)\|_2^2, \tag{31}$$

$$\mathscr{L}_F = \frac{1}{|\mathscr{C}_F|}\sum_{t_m\in\mathscr{C}_F}\left[r_F^2(t_m) + r_{Q_x}^2(t_m) + r_{Q_y}^2(t_m)\right], \tag{32}$$

$$\mathscr{L}_I = \frac{1}{|\mathscr{C}_I|}\sum_{(\mathbf{x}_n,t_n)\in\mathscr{C}_I}\|\mathbf{r}_I(\mathbf{x}_n,t_n)\|_2^2, \tag{33}$$

where $\mathscr{C}_b$ and $\mathscr{C}_I$ are the boundary and interface collocation sets, respectively, and $\mathscr{C}_F$ is the set of force-closure time points.

The full PINN objective is:

$$\mathscr{L}(\boldsymbol{\theta}) = w_d\mathscr{L}_d + w_\Omega\mathscr{L}_\Omega + w_b\mathscr{L}_b + w_F\mathscr{L}_F + w_I\mathscr{L}_I + w_R\mathscr{R}(\boldsymbol{\theta}), \tag{34}$$

where w_d, w_Ω, w_b, w_F, w_I, and w_R are non-negative weights, and $\mathscr{R}(\boldsymbol{\theta})$ is a regularization functional. The adaptive loss weights are updated by:

$$w_j^{(k+1)} = (1-\alpha_w)w_j^{(k)} + \alpha_w\frac{\overline{\mathscr{L}}^{(k)}}{\mathscr{L}_j^{(k)} + \varepsilon_w}, j \in \{d,\Omega,b,F,I\}, \tag{35}$$

where k is the training index, α_w is a relaxation parameter, ε_w is a stabilizer, and $\overline{\mathscr{L}}^{(k)}$ is the mean of the component losses at training iteration k. The training and evaluation procedure yields component losses, total training loss, validation loss, test loss, loss-balance weights, optimizer update norms, weight-drift measures, force-share measures, and residual-allocation indicators. The corresponding diagnostic definitions are collected in Appendix C.

2.4. Scenario-conditioned reconstruction, transient moving-load response, and stability assessment

The final component extends the inverse reconstruction from a single loading configuration to a scenario-conditioned transient operator. Across the complete forward scenario space, the contact traction and internal response may vary with load level, contact size, normal-pressure heterogeneity, moving-load speed, braking ratio, lateral slip, and material-domain state. These quantities are used to construct distinct loading scenarios and to assess the sensitivity, transferability, and robustness of the proposed framework. However, they do not all constitute prescribed inputs to the blind inverse problem. In particular, the source-related quantities associated with load scale, normal-pressure heterogeneity, braking, and lateral slip are treated as unknowns during blind reconstruction. To distinguish these unknown source descriptors from the independently available operating, geometric, and material information, a known scenario-conditioning vector $\boldsymbol{\zeta}_g$ is introduced for the inverse operator. Unlike a shifted static-field representation, the moving load enters the transient boundary condition through its time-dependent footprint position, and each speed produces a separate dynamic solution governed by inertia and damping. The same framework also supports stability checks with respect to finite-domain size, source resolution, regularization strength, observation uncertainty, and material perturbation.

The blind inverse reconstruction is therefore conditioned only on the independently available scenario information. Let

$$\boldsymbol{\zeta}_g = [\,\zeta_a \quad \zeta_v \quad \zeta_m\,]^{\mathrm{T}}, \tag{36}$$

denote the known scenario-conditioning vector, where ζ_a represents the

contact radius, ζ_v represents the moving-load speed, and ζ_m represents the material-domain state. In contrast, the load-scale descriptor ζ_P, normal-pressure heterogeneity descriptor ζ_n, braking descriptor ζ_b, and lateral-slip descriptor ζ_s characterize the unknown contact source and are not supplied to the inverse operator at blind-test time. These source quantities are subsequently recovered from the reconstructed source coefficients rather than prescribed as scenario inputs. The reconstructed operator is therefore written as:

$$\mathscr{G}_{\boldsymbol{\theta}}\left(\mathbf{x}, \mathbf{s}, t, \boldsymbol{\zeta}_g, \mathscr{O}_u, \mathscr{O}_\sigma, \widetilde{\mathbf{R}}\right) = \begin{bmatrix} \widehat{\mathbf{u}}(\mathbf{x}, t) \\ \widehat{\boldsymbol{\sigma}}(\mathbf{x}, t) \\ \widehat{\mathbf{t}}_c(\mathbf{s}, t) \\ \widehat{\mathbf{c}} \end{bmatrix}, \tag{37}$$

where $\mathscr{O}_u$ and $\mathscr{O}_\sigma$ denote the sparse displacement and stress observations, respectively, and $\widetilde{\mathbf{R}} = \left[\widetilde{P}, \widetilde{Q}_x, \widetilde{Q}_y\right]^{\mathrm{T}}$ contains the independently observed global force resultants used as soft force-closure constraints. The vector $\widehat{\mathbf{c}} = [\widehat{c}_1, \widehat{c}_2, \widehat{c}_3, \widehat{c}_4]^{\mathrm{T}}$ contains the four reconstructed source coefficients. The corresponding load-scale, normal-pressure-heterogeneity, braking, and lateral-slip descriptors are obtained from these coefficients as $\widehat{\zeta}_P = \widehat{c}_1$, $\widehat{\zeta}_n = \widehat{c}_2/\widehat{c}_1$, $\widehat{\zeta}_b = \widehat{c}_3/\widehat{c}_1$, and $\widehat{\zeta}_s = \widehat{c}_4/\widehat{c}_1$, rather than being prescribed as inputs to the blind inverse problem.

To avoid source leakage, the partition is performed at the level of complete contact-source realizations rather than by randomly dividing observation points from the same FE solution. The training, validation, and blind-test subsets therefore contain mutually distinct combinations of the unknown source descriptors. At blind-test time, the complete target traction fields and their exact source coefficients remain withheld from the inverse operator.

The source-disjoint partition enables the framework to evaluate whether the PINN has learned a transferable mechanics-constrained inverse map rather than a response field tied to a prescribed contact source. The withheld reference traction fields and exact source coefficients are introduced only after reconstruction for quantitative error evaluation.

Stability is evaluated through response sensitivity to finite-domain truncation, source resolution, and regularization strength. For a scalar response quantity $\mathscr{S}$, such as peak von Mises stress, maximum vertical deflection, strain-energy integral, or force-closure residual, the relative truncation sensitivity is:

$$\eta_R = \frac{\left|\mathscr{S}_R - \mathscr{S}_{R_{\mathrm{ref}}}\right|}{\left|\mathscr{S}_{R_{\mathrm{ref}}}\right| + \varepsilon_R}, \tag{38}$$

where R is a finite-domain size parameter, R_{ref} is a reference value, and ε_R is a stabilizer. Source-resolution stability is assessed by monitoring load-resultant closure, tangential closure, and edge-oscillation measures as the source basis is refined. Regularization stability is evaluated by comparing data misfit, physics misfit, and a loss-balance score over a range of regularization weights.

In addition to the finite-domain response sensitivity in Eq. (38), transient boundary effects are assessed explicitly from the propagation and return of elastic waves in the truncated layered domain. For a layer with Young's modulus E_l, Poisson's ratio ν_l, and density ρ_l, the shear-wave velocity and the corresponding one-way and round-trip travel times over a propagation depth H are evaluated as:

$$\begin{aligned} c_{s,l} &= \sqrt{\frac{G_l}{\rho_l}} = \sqrt{\frac{E_l}{2(1+\nu_l)\rho_l}}, \\ t_s &= \frac{H}{c_{s,l}}, \\ t_{rt} &= \frac{2H}{c_{s,l}}. \end{aligned} \tag{39}$$

To distinguish the primary moving-load response from boundary-returned wave components, the standard truncated model is additionally compared with auxiliary models containing a graded viscous buffer and an enlarged domain with the same buffer. The buffer introduces additional damping only within the outer boundary region, leaving the near-field pavement properties unchanged. Reflection sensitivity is quantified from the late-time vertical particle velocity using:

$$v_{\mathrm{RMS}}(z) = \sqrt{\frac{1}{t_2 - t_1}\int_{t_1}^{t_2} v_z^2(z, t)\mathrm{d}t}, \tag{40}$$

where $[t_1, t_2]$ denotes a time window following the principal tire-passage response. The corresponding late-window frequency spectrum is also examined to identify frequency components whose amplitudes are sensitive to the finite-boundary treatment.

For a moving tire footprint, the contact center and boundary traction are defined as:

$$\begin{aligned} \mathbf{x}_L(t) &= \mathbf{x}_0 + \mathbf{v}_L t, \\ \mathbf{t}_c(\mathbf{x}_\parallel, t; \boldsymbol{\zeta}) &= \widetilde{\mathbf{t}}_c(\mathbf{x}_\parallel - \mathbf{x}_L(t); \boldsymbol{\zeta}), , \\ \boldsymbol{\Phi}_z(t; \boldsymbol{\zeta}) &= \mathscr{A}_z[\boldsymbol{\Phi}(\mathbf{x}, t; \boldsymbol{\zeta})\,] \end{aligned} \tag{41}$$

where $\mathscr{A}_z[\cdot]$ denotes a prescribed centerline, sensor-point, or cross-sectional averaging operator at depth z. The response $\Phi_z(t;\boldsymbol{\zeta})$ is extracted from the solution of the dynamic governing equations and is not obtained by translating a previously computed static field. Consequently, moving-load speed influences the response through the time-dependent boundary condition, inertia, damping, and wave transmission within the layered structure.

The framework also includes damage-oriented mechanical proxies, domain-transfer indicators, parameter-combination response maps, and robustness diagnostics. These quantities are not introduced as additional material laws. They are post-processing descriptors derived from the reconstructed stress, strain, displacement, source, and scenario fields. Their definitions are provided in the appendices to preserve a clear separation between the governing mechanics and diagnostic evaluation.

2.5. Algorithmic workflow of the proposed framework

The above formulations are implemented through a computational workflow linking the mixed tire-contact traction, the three-dimensional transient pavement model, the PINN-based inverse reconstruction, and the final mechanics-consistency checks. The transient FE solver first generates mechanically admissible space–time response fields for independently prescribed contact-source realizations. These realizations are divided into source-disjoint training, validation, and test groups before sparse observations are extracted. The PINN is then trained using sparse response histories and the composite objective in Eq. (34), while the target source fields of blind test cases remain withheld. The trained operator reconstructs the total normal pressure, the two tangential tractions, and the internal dynamic response. Field errors, force closure, transient transfer, finite-domain stability, regularization stability, and robustness are subsequently evaluated from direct model outputs. Algorithm 1 summarizes the pseudocode for the implementation.

Algorithm 1: Core procedure of the PINN-based inverse tire-contact traction reconstruction framework

Input: Three-dimensional layered domain $\Omega = \bigcup_\ell \Omega_\ell$, interfaces Γ_I, contact region Γ_c, material parameters $\{E_\ell, \nu_\ell, \rho_\ell, \eta_\ell\}$, sparse response observations $\mathscr{O} = \{\mathbf{u}^{\mathrm{obs}}, \boldsymbol{\sigma}^{\mathrm{obs}}\}$, known scenario-conditioning vector $\boldsymbol{\zeta}_g$, independently observed global force resultants $\widetilde{\mathbf{R}}$, and collocation sets in Ω, Γ_c, and Γ_I.

Output: Reconstructed contact traction $\mathbf{t}_c = \left(q_x, q_y, -p_n\right)^{\mathrm{T}}$, reconstructed fields $\mathbf{u}$, $\boldsymbol{\sigma}$, $\boldsymbol{\varepsilon}$, and strain-energy density ψ, together with mechanics-consistency and stability indicators.

1 : Define the mixed contact-traction source on Γ_c:
2 : $\mathbf{t}_c = q_x\mathbf{e}_x + q_y\mathbf{e}_y - p_n\mathbf{e}_z$.
3 : Assign the layerwise elastic, density, and damping parameters.

(*continued on next page*)

(*continued*)

Algorithm 1: Core procedure of the PINN-based inverse tire-contact traction reconstruction framework

Impose displacement and traction continuity on all bonded interfaces.
Generate the three-dimensional FE mesh.
Assemble the element mass, damping, and stiffness matrices.
Define the moving footprint center $\mathbf{x}_L(t) = \mathbf{x}_0 + \mathbf{v}_L t$.
Assemble the time-dependent contact-force vector from $\mathbf{t}_c(\mathbf{x}_{\|}, t)$.
Solve $\mathbf{M}\ddot{\mathbf{U}}(t) + \mathbf{C}\dot{\mathbf{U}}(t) + \mathbf{K}\mathbf{U}(t) = \mathbf{F}(t)$ over the prescribed time interval.
Recover displacement, velocity, acceleration, strain, stress, reactions, and strain-energy histories.
Verify transient equilibrium and normal and tangential resultant closure.
Generate independent contact-source realizations and divide them into source-disjoint training, validation, and test groups.
Extract sparse response histories without exposing the held-out source fields.
Define $\mathscr{G}_{\boldsymbol{\theta}}\left(\mathbf{x}, \mathbf{s}, t, \boldsymbol{\zeta}_g, \mathscr{O}_u, \mathscr{O}_\sigma, \widetilde{\mathbf{R}}\right) = \begin{bmatrix} \widehat{\mathbf{u}}(\mathbf{x}, t) \\ \widehat{\boldsymbol{\sigma}}(\mathbf{x}, t) \\ \widehat{\mathbf{t}}_c(\mathbf{s}, t) \\ \widehat{\mathbf{c}} \end{bmatrix}$.
Use automatic differentiation to evaluate dynamic-equilibrium, constitutive, boundary, interface, and force-closure residuals.
Form the composite objective in Eq. (34).
Update $\boldsymbol{\theta}$ and the adaptive loss weights until convergence.
Reconstruct p_n, q_x, q_y, and the transient pavement fields for held-out sources.
Compare the reconstructed source and response fields with the corresponding withheld source fields and full FE response fields.
Evaluate finite-domain, source-resolution, and regularization stability, together with dynamic-transfer performance and perturbation robustness.
Return the reconstructed contact traction and mechanics-consistent transient response.

3. Results

The dataset used in this section was constructed from the three-dimensional transient finite-layer pavement model and the mixed tire–pavement contact-traction formulation described in the methodology. The pavement geometry, seasonal material properties, tire load, contact radius, and boundary-source parameters were specified according to Table 1 and Table 2. Several structural and loading parameters were selected with reference to a previous FE-based study of asphalt pavement response under static loading, in which the multilayer response was evaluated using a semi-analytical FE formulation and verified against conventional FE simulations (Liu et al., 2015). In the adopted pavement structure, the road base represents a cement-stabilized load-bearing layer with relatively high stiffness, whereas the sub-base corresponds to a weaker granular supporting layer. The pronounced modulus contrast therefore reflects the different material functions and load-bearing capacities assigned to these two structural courses, and its influence is further assessed through the material-perturbation and robustness analyses. On this basis, winter and summer reference-response libraries were generated separately using the corresponding seasonal modulus combinations, while the same pavement geometry, boundary conditions, and load definitions were retained to ensure a controlled seasonal comparison. Scenario-dependent samples were then constructed by varying the moving speed, contact radius, load scale,

Table 1
Layerwise pavement parameters.

Symbol	Meaning	Value
Ω_ℓ	Layered pavement domains ordered from surface to subgrade	Surface course, binder course, asphalt base course, road base course, sub-base, subgrade
$\mathbf{h}$	Layer-thickness vector	[40, 80, 140, 150, 340, 2000] mm
$\mathbf{z}_I$	Interface-depth vector from pavement surface	[0, 40, 120, 260, 410, 750, 2750] mm
H	Total finite pavement depth	2750 mm
$\mathbf{E}^{\mathrm{w}}$	Winter elastic-modulus vector	[22690, 27283, 17853, 10000, 100, 45] MPa
$\mathbf{E}^{\mathrm{s}}$	Summer elastic-modulus vector	[2902, 6817, 4903, 10000, 100, 45] MPa
$\boldsymbol{\nu}$	Reference Poisson-ratio vector	[0.35, 0.35, 0.35, 0.25, 0.49, 0.49]
$\boldsymbol{\rho}$	Layer-density vector	[2400, 2400, 2350, 2200, 2000, 1900] kg·m^{-3}
$\boldsymbol{\eta}$	Layerwise mass-proportional damping vector	[26, 26, 24, 21, 18, 16] s^{-1}
L_x	Road-panel length	6000 mm
L_y	Road-panel width	6000 mm

Table 2
Model, loading, scenario, and diagnostic parameters.

Symbol	Meaning	Value
T	Transient-analysis duration	0.60 s
Δt	Time increment	0.0025 s
P	Applied tire load	49 kN
a	Circular contact radius	150 mm
p_0	Uniform equivalent contact pressure	$P/(\pi a^2) \approx 0.693$MPa
N_{sc}	Number of scenario samples	120
β_N, γ_N	Newmark integration parameters	1/4, 1/2
x_0	Initial moving-load center coordinate	−1.60 m
$\mathscr{D}_{\mathrm{train}} : \mathscr{D}_{\mathrm{val}} : \mathscr{D}_{\mathrm{test}}$	Training, validation, and test split	Source-disjoint 70%:15%:15%; 84:18:18 scenarios, corresponding to 42:9:9 distinct load cases per season
N_{ROM}	Reduced FE basis dimension	36
$\boldsymbol{\zeta}_g$	Known scenario-conditioning vector	Contact radius, moving-load speed, and seasonal material state
ζ_P	Load-scale range for random scenarios	[0.70, 1.35]
v	Speed range for random scenarios	[20, 120] km·h^{-1}
ζ_b	Braking-ratio range for random scenarios	[−0.20, 0.25]
ζ_s	Lateral-slip range for random scenarios	[−0.08, 0.08]
N_{epoch}	Loss-curve epoch length	50,000
λ_R	Regularization-weight scan	logspace$(-4, 1, 10)$
n_b	Boundary-source basis order scan	2:2:20
ζ_P^{scan}	Load-scale scan for response surfaces	[0.65, 1.45]
a^{scan}	Contact-radius scan	[120, 220] mm
v^{scan}	Speed scan in parameter diagnostics	[20, 120] km·h^{-1}
ζ_b^{scan}	Braking-ratio scan	[0, 0.35]
η_p^{scan}	Normal-pressure heterogeneity coefficient scan	[0,1], 42 samples
v_L	Moving-load transfer speed	60 km·h^{-1}
$\mathbf{x}_q$	Load-center coordinates used for sparse observations	[−0.45, −0.30, −0.15, 0, 0.15, 0.30, 0.45] m
N_t	Moving-load time samples	241
N_p	Number of sparse response probes	6
N_{obs}	Observation points per blind case	$6 \times 7 = 42$
N_{scalar}	Scalar observations per blind case	$42 \times 4 = 168$
$\mathscr{S}_{\mathrm{obs}}$	Observation configurations in the sparsity study	4×5, 4×7, 6×5, 6×7, 8×7, 8×9
$\mathbf{z}_q$	Moving-load diagnostic depths	12 samples in [0.04, 0.95] m
δ_E	Elastic-modulus perturbation range	[−30, 30] %
δ_ν	Poisson-ratio perturbation range	[−8, 8] %
δ_a	Contact-radius perturbation range	[−25, 25] %

total normal-pressure heterogeneity, longitudinal braking ratio, lateral-slip ratio, and seasonal material state. To provide a rigorous blind evaluation of the inverse reconstruction, the training, validation, and reconstruction loads were generated from mutually disjoint parameter combinations, and none of the reconstruction loads was used during network training or model selection. In addition, an independent parameter combination was introduced for comparison with previously published experimental and numerical pavement-response results, providing an external benchmark for the proposed PINN reconstruction framework (Elseifi et al., 2006).

For the numerical analyses, the layerwise mass-proportional damping coefficients were selected with reference to the characteristic tire-passage frequency rather than a fixed low-frequency value. For the representative moving-load condition, the characteristic frequency estimated from the footprint passage duration is approximately $f_c = v/(2a)$, at which the adopted coefficients correspond to equivalent damping ratios of approximately 2.3–3.7%. This range is consistent with damping levels commonly employed in dynamic pavement analyses, where values of approximately 2–5% and comparable layer-dependent damping levels have been reported (Huang et al., 2022; Assogba et al., 2021).

The inverse network employed a single hidden layer with 48 neurons and a hyperbolic-tangent activation function. The network parameters were optimized using the Adam algorithm (Kingma and Ba, 2014) with $\beta_1 = 0.9; \beta_2 = 0.999$, and $\varepsilon = 10^{-8}$. A warm-up and decaying learning-rate strategy was adopted, with the nominal learning rate varying from 7.2×10^{-4} to 1.1×10^{-5} during training. This compact architecture was sufficient for learning the bounded nonlinear correction of the mechanics-based source estimate while limiting unnecessary model complexity. The full-order 3D FE model was discretized using eight-node trilinear hexahedral elements on a nonuniform structured mesh. The adopted mesh contained 19, 15, and 25 nodes in the longitudinal, transverse, and depth directions, respectively, corresponding to 7125 nodes, 6048 elements, and 21,375 mechanical degrees of freedom. The mesh was locally refined around the tire-contact region and moving-load path, with a minimum in-plane spacing of 75 mm, while progressively coarser spacing was used toward the outer boundaries. Through the pavement depth, the six structural layers were subdivided into 2, 3, 4, 3, 4, and 8 elements, respectively, with the layer interfaces coinciding with FE nodal planes.

Based on the parameter settings in Table 1 and Table 2, a series of numerical experiments were conducted to validate the effectiveness of the proposed framework. Fig. 3 presents the finite-layer pavement geometry and the season-dependent stiffness contrast adopted in the numerical dataset. The pavement structure consists of six layers, namely the surface course, binder course, asphalt base course, road base, sub-base, and subgrade. The winter and summer cases share the same layer thicknesses, geometric dimensions, boundary conditions, and contact-loading definitions, while the asphalt layers are assigned different elastic moduli to represent the seasonal stiffness contrast. The asphalt layers exhibit higher stiffness in winter and lower stiffness in summer, whereas the mechanical properties of the underlying supporting layers are kept unchanged. This controlled configuration makes it possible to isolate the influence of asphalt-layer stiffness on stress diffusion, deformation localization, interface transfer, moving-load response, and inverse reconstruction accuracy.

The following results are organized to examine the proposed framework from three complementary perspectives. First, the reconstructed fields are compared with the three-dimensional transient FE reference fields to evaluate the accuracy of the PINN-based inverse reconstruction, including the internal stress, strain, and displacement responses, as well as the total normal-pressure, longitudinal-traction, and lateral-traction components at the tire–pavement interface. The training, validation, and reconstruction cases are generated from mutually disjoint loading combinations so that the blind reconstruction is performed under loads not used for network training or model

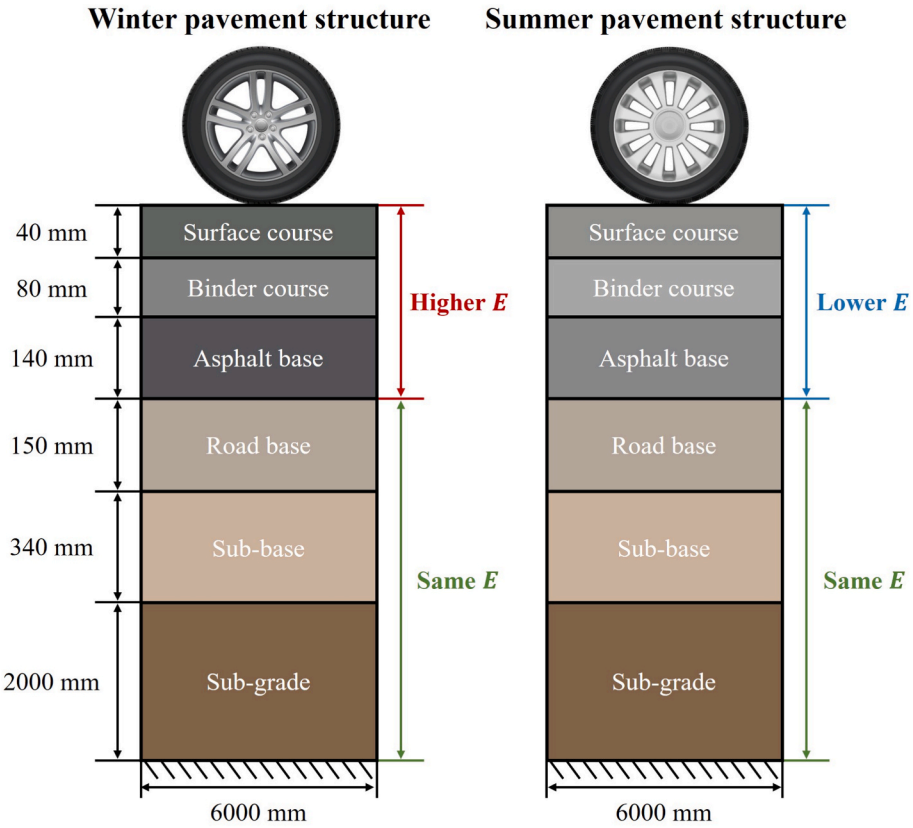


Fig. 3. Finite-layer pavement geometry and season-dependent stiffness contrast under winter and summer conditions.

selection. Second, the winter and summer pavement responses are analyzed under matched contact-loading conditions to reveal how the seasonal stiffness contrast affects stress transfer, strain localization, transient load propagation, layer contributions, interface continuity, and damage-related indicators. Third, parameter scans, identifiability diagnostics, domain-transfer analysis, parameter-combination maps, robustness tests, blind-load reconstruction results, sparsity statistics, and comparison with an independent published experimental–numerical benchmark are presented to assess the stability, physical consistency, and generalization capability of the proposed reconstruction framework under different loading, contact, material, and observation conditions.

3.1. Training behavior, reconstruction accuracy, and independent validation

This subsection evaluates the training behavior, reconstruction accuracy, and independent validation of the proposed inverse PINN framework. The analysis first examines the total and component losses, adaptive loss weights, task-gradient interactions, and scenario-level errors to establish convergence under the source-disjoint data partition. The reconstructed stress, strain, and displacement fields are then compared with the 3D transient FE reference fields, while footprint-level errors are used to evaluate the recovery of the total normal pressure and the longitudinal and lateral traction components. Additional blind-load, sparsity, and physics-agreement diagnostics determine whether previously unseen source combinations can be reconstructed from limited observations. Finally, a comparison with the published experimental and numerical benchmark in Elseifi et al. (2006) provides an external assessment of adaptability beyond the numerical scenarios used for model development.

Fig. 4 summarizes the convergence, adaptive weighting, and multi-objective optimization behavior of the inverse PINN. As shown in Fig. 4 (a), the training, validation, and test losses undergo a rapid initial adjustment and subsequently enter a statistically stationary regime over the remainder of the 5×10^4 training epochs. The persistent small-amplitude fluctuations arise from the changing source-disjoint mini-batches and the nonstationary loss balancing used during optimization, rather than from numerical divergence. Although the validation loss is generally slightly higher, the three curves remain within the same order of magnitude without progressive separation, indicating that the learned inverse mapping retains comparable performance for loads excluded from parameter updating.

The individual loss components in Fig. 4 (b) stabilize at distinct scales. The dynamic-physics residual remains the largest component, whereas the data, boundary, force-closure, and interface terms are maintained at substantially lower levels. In particular, the interface residual reaches the lowest magnitude, indicating effective enforcement of bonded-layer compatibility. These unequal raw loss levels are compensated by the adaptive weights in Fig. 4 (c). After the initial redistribution, the force-closure term receives the largest weight, followed by the boundary term, whereas the data and dynamic-physics weights stabilize at lower values. The resulting weighting pattern does not force all component losses to the same magnitude; instead, it prevents the dominant domain residual from suppressing the more localized boundary, resultant-force, and interface constraints.

Fig. 4 (d) shows that the parameter-update norm and loss-weight drift remain bounded and gradually decrease after the initial transient, while the loss-balance consistency stabilizes at approximately 0.38. This behavior indicates that the adaptive weighting mechanism reaches a persistent operating regime without eliminating the stochastic corrections required by the changing mini-batches. The task-gradient diagnostics in Fig. 4 (e) provide a more direct assessment of multi-objective interaction. The data–physics gradient cosine fluctuates around a small positive level and occasionally becomes negative, whereas the boundary–interface cosine remains predominantly positive. Meanwhile, the conflicting-pair fraction remains appreciable throughout training. Thus, the component objectives are not trivially aligned; rather, the optimizer maintains a controlled compromise

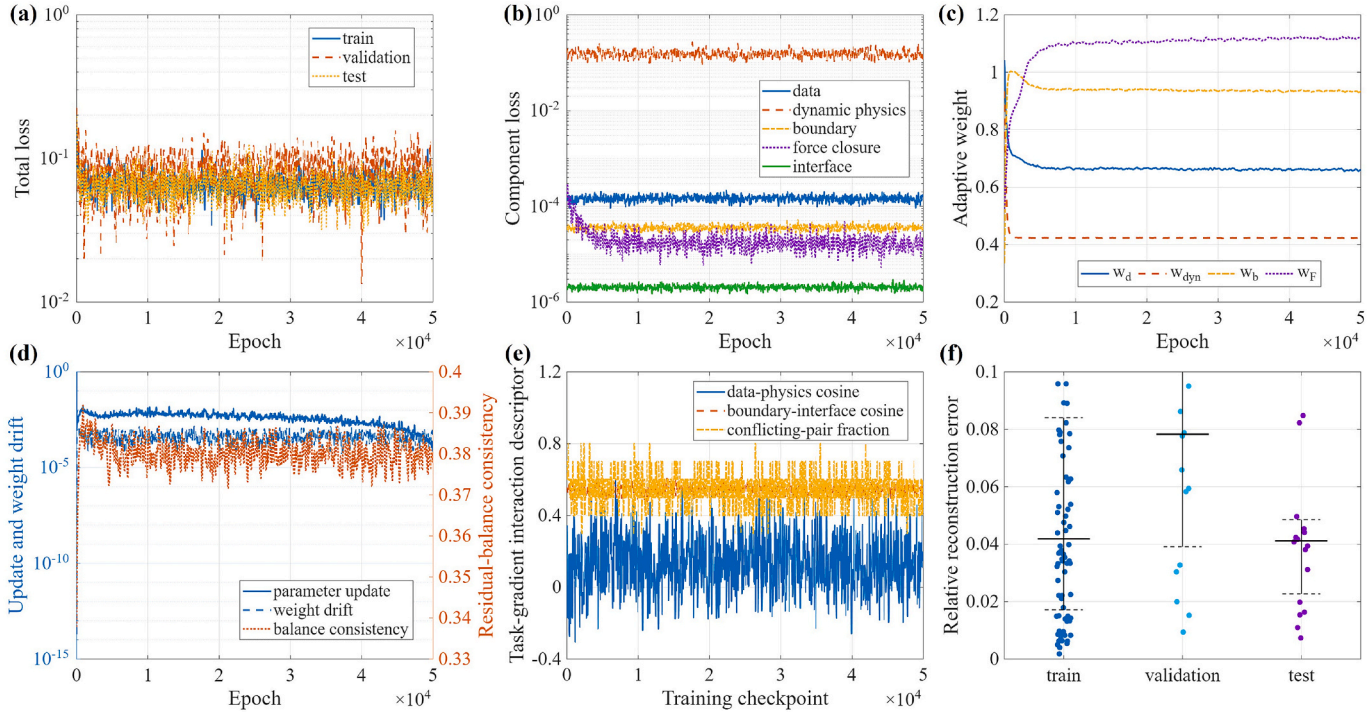


Fig. 4. Training convergence and multi-objective optimization diagnostics of the source-disjoint inverse PINN: (a) total loss $\mathscr{L}$ for the training, validation, and blind-test sets; (b) data, dynamic-physics, boundary, force-closure, and interface loss components; (c) adaptive loss weights w_d, w_{dyn}, w_b, w_F, and w_I; (d) parameter-update norm, loss-weight drift, and loss-balance consistency; (e) data–physics gradient cosine, boundary–interface gradient cosine, and conflicting-gradient-pair fraction; and (f) scenario-level relative reconstruction errors for the training, validation, and blind-test sets.

among partially competing data and mechanics constraints.

The scenario-level errors in Fig. 4 (f) further support the source-disjoint evaluation. The validation group exhibits a higher central error than the training group, while the blind-test distribution remains close to the training distribution for most cases. Most test errors are below approximately 5%, although several more challenging source realizations produce larger deviations. The absence of systematic error growth from training to blind testing indicates that the reconstructed contact-source coefficients are not restricted to the load combinations used during network optimization.

In addition, Table 3 summarizes the computational costs of the proposed framework. Although the PINN requires an offline training stage, this cost is incurred only once and is subsequently amortized over repeated inverse reconstructions. Once trained, the response libraries for the winter and summer cases can be generated efficiently, avoiding repeated FE analyses for each new reconstruction scenario. This computational characteristic makes the proposed framework particularly suitable for applications requiring rapid repeated inference, such as pavement structural health monitoring, condition assessment, and near-real-time load identification.

Fig. 5 compares the PINN-reconstructed vertical compressive stress with the three-dimensional transient FE reference field under the winter and summer material states. The winter and summer responses were evaluated using the same source-disjoint blind reconstruction load, which was not included in the network-training or model-selection datasets. Therefore, the seasonal comparison is not affected by differences in moving speed, contact radius, load scale, normal-pressure heterogeneity, braking ratio, or lateral slip. Here, σ_{zz}^{c} denotes the compressive-positive vertical stress component, obtained by reversing the sign of the tensile-positive vertical stress where necessary. The displayed fields correspond to the central $x - z$ section of the three-dimensional pavement domain.

In both seasons, the FE solution forms a clear compressive stress bulb beneath the tire-contact region, with the largest σ_{zz}^{c} concentrated near the pavement surface and rapidly attenuating with increasing depth and longitudinal distance from the load center. The near-surface stress approaches the upper limit of the displayed color scale, approximately 0.80 MPa, whereas the response becomes progressively smoother and weaker in the deeper supporting layers. The highlighted regions further distinguish the highly localized near-contact response from the broader depthwise stress-diffusion zone. These results show that vertical load transfer is governed primarily by the applied normal contact pressure near the surface, while a spatially distributed compressive response is transmitted through the finite-layer pavement system.

The PINN reconstructions in panels (b) and (e) reproduce the corresponding FE fields in panels (a) and (d) with high spatial consistency. The reconstructed fields preserve the position of the maximum compressive stress, the longitudinal spread of the stress bulb, and its gradual attenuation through the pavement depth. This agreement is mechanically important because σ_{zz}^{c} directly characterizes compressive load transfer and contributes to deformation and rutting-related responses in layered pavements. The winter and summer fields exhibit broadly similar spatial patterns because the same pavement geometry and blind contact load are used. Nevertheless, the seasonal modulus contrast produces observable differences in the detailed diffusion and depthwise attenuation of the compressive field, particularly beneath the asphalt layers and near the transition toward the supporting courses.

Table 3
Computational times of the proposed framework.

Computational stage	Time
FE preprocessing (mesh, assembly, factorization)	8.32 s
FE solve time	35.11 s
PINN training time	234.24 s
PINN inference time per case	8.12 s
Winter response-library time	24.12 s
Summer response-library time	23.47 s

Panels (c) and (f) present the normalized reconstruction error of σ_{zz}^{c}, calculated from the pointwise PINN–FE difference and normalized by the maximum absolute FE stress. The error remains within the displayed $\pm 1.0\%$ range over most of the pavement domain. The relatively larger deviations are concentrated near the contact region and along the central load-transfer path, where the vertical-stress gradients are strongest. In the deeper and laterally remote regions, the error is weak and spatially smooth. The results therefore indicate that the PINN reproduces not only the overall magnitude of the FE response but also the mechanically relevant features of the stress field, including near-contact localization, longitudinal diffusion, and depthwise attenuation under a previously unseen reconstruction load.

Fig. 6 presents the lateral–depth distributions of representative pavement responses, complementing the longitudinal sections by resolving the stress and deformation transfer across the pavement width. In the winter state, the vertical compressive stress σ_{zz}^{c} in Fig. 6 (a) forms a compact stress bulb beneath the center of the contact area. Its maximum approaches 0.8 MPa near the pavement surface, followed by rapid attenuation with both depth and lateral distance. The nearly symmetric distribution about $y = 0$ indicates that the normal load component governs the principal compressive transfer in the lateral section.

The lateral stress σ_{yy}^{c} in Fig. 6 (b) exhibits a more complex distribution than σ_{zz}^{c}. A localized compressive region develops directly beneath the loaded area, while weaker regions of opposite sign appear at greater depth. This pattern reflects lateral confinement, Poisson-induced deformation, and stress redistribution across layers with different stiffnesses. The shear field τ_{yz} in Fig. 6 (c) is characterized by two lobes of opposite sign on either side of the load center. The sign reversal across $y = 0$, with peak magnitudes of approximately ± 0.15 MPa, is consistent with the lateral equilibrium of the three-dimensional stress field and identifies the central axis as the transition between the two shear-transfer directions.

For the summer material state, the von Mises stress in Fig. 6 (d) remains concentrated beneath the contact region but extends through a comparatively broad depth interval. Local variations near the asphalt-layer boundaries indicate that the reduced summer stiffness modifies the partition of deviatoric stress between the upper asphalt courses and the supporting layers. The mean compressive stress p_m in Fig. 6 (e) is strongly localized along the central load-transfer path, reaching its highest value near the surface and decreasing rapidly below the asphalt structure. Compared with the deviatoric response, the mean stress field is more directly associated with volumetric compression produced by the applied normal traction.

The vertical deflection in Fig. 6 (f) displays a smooth and laterally symmetric basin, with a maximum value of approximately 0.12 mm near the pavement surface. Its spatial extent is considerably broader than that of the stress concentrations, because displacement represents the accumulated compliance of the entire layered system rather than a local stress measure. Overall, the y-z fields distinguish three response mechanisms: localized normal-stress transfer beneath the contact area, antisymmetric lateral shear transmission across the load axis, and broad deformation spreading through the softened summer pavement structure.

Fig. 7 provides a complementary assessment of reconstruction quality by focusing on absolute error levels, convergence evidence, and interface-continuity diagnostics. The error maps in Fig. 7 (a)–(c) show that the largest discrepancies are confined to the near-contact zone and to regions with strong stress gradients. In the winter case, the absolute error in σ_{zz}^{c} remains small over most of the pavement domain and reaches its maximum close to the loaded surface region, with the displayed scale limited to 1.2×10^{-2} MPa. The summer field in Fig. 7 (b) exhibits an even smaller absolute error range, on the order of 10^{-3} MPa, indicating that the reconstructed vertical compressive field retains high fidelity under the softer seasonal material state. The von Mises error in

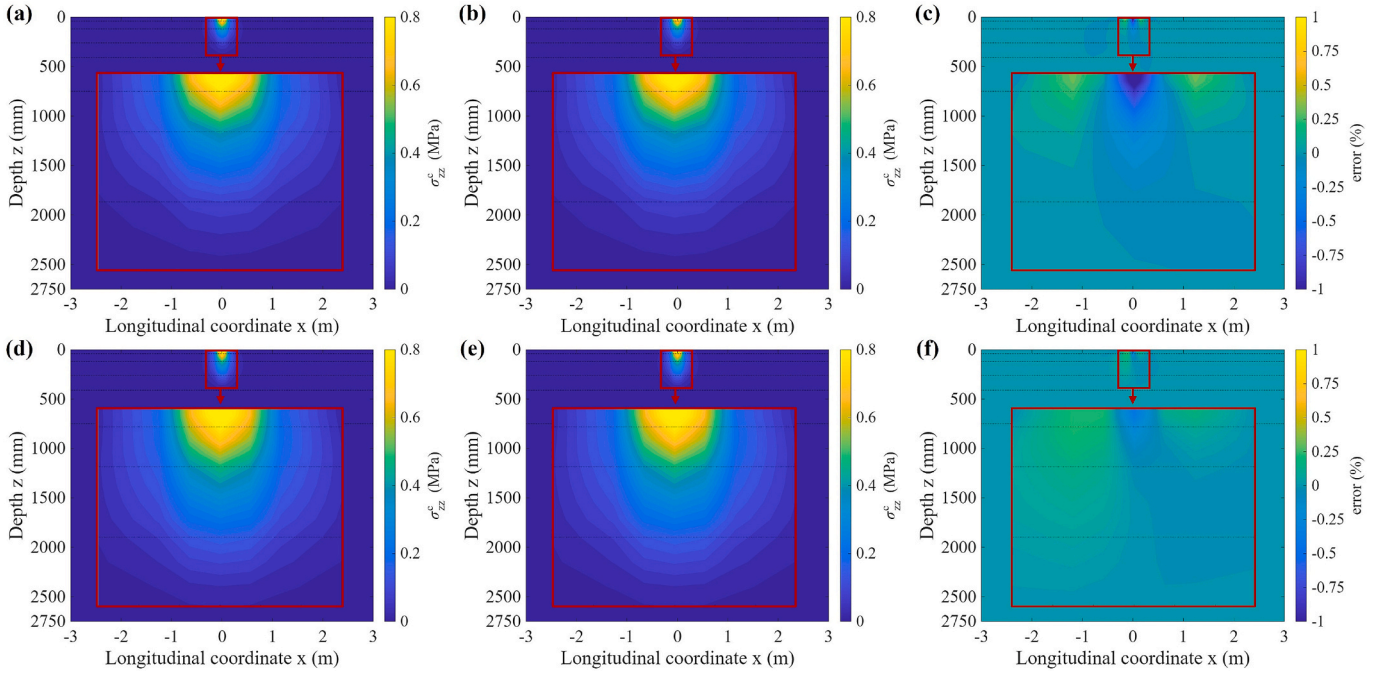


Fig. 5. PINN reconstruction of vertical compressive stress compared with the three-dimensional transient FE reference under the same source-disjoint blind load: (a) FE winter field of vertical compressive stress σ^c_{zz} in the central $x-z$ section, (b) corresponding PINN winter reconstruction, (c) winter normalized reconstruction error, (d) FE summer field of σ^c_{zz} in the central $x-z$ section, (e) corresponding PINN summer reconstruction, and (f) summer normalized reconstruction error. The winter and summer cases share the same pavement geometry and contact-loading parameters but use their respective seasonal material properties.

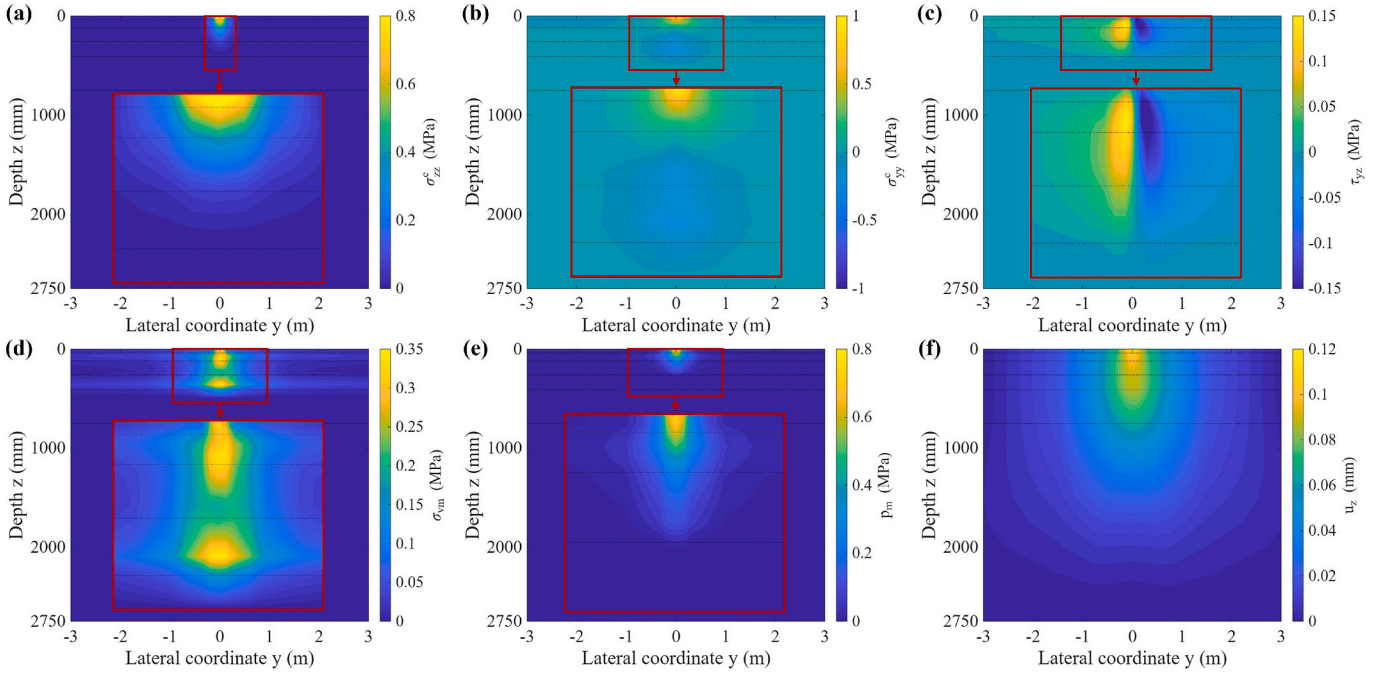


Fig. 6. 3D lateral–depth response fields under matched seasonal loading conditions: (a) winter vertical compressive stress σ^c_{zz}, (b) winter lateral compressive stress σ^c_{yy}, (c) winter lateral–depth shear stress τ_{yz}, (d) summer von Mises stress σ_{vm}, (e) summer mean compressive stress p_m, and (f) summer vertical deflection u_z.

Fig. 7 (c) follows a similarly localized pattern, which confirms that the PINN captures not only the primary compressive transfer but also the multiaxial stress intensity with limited absolute deviation.

The convergence evidence in Fig. 7 (d) indicates that the optimization enters a stable regime after the initial training stage. The local log-loss slope decreases by several orders of magnitude, showing that the rate of further reduction becomes progressively smaller. At the same time, the detrended oscillation amplitude rapidly decays and remains close to zero, implying that the residual fluctuations observed in the loss history do not correspond to persistent large-amplitude instability. Together, these two indicators support the interpretation that the model reaches a practically converged state while retaining the stochastic variability associated with mini-batch optimization and adaptive loss balancing.

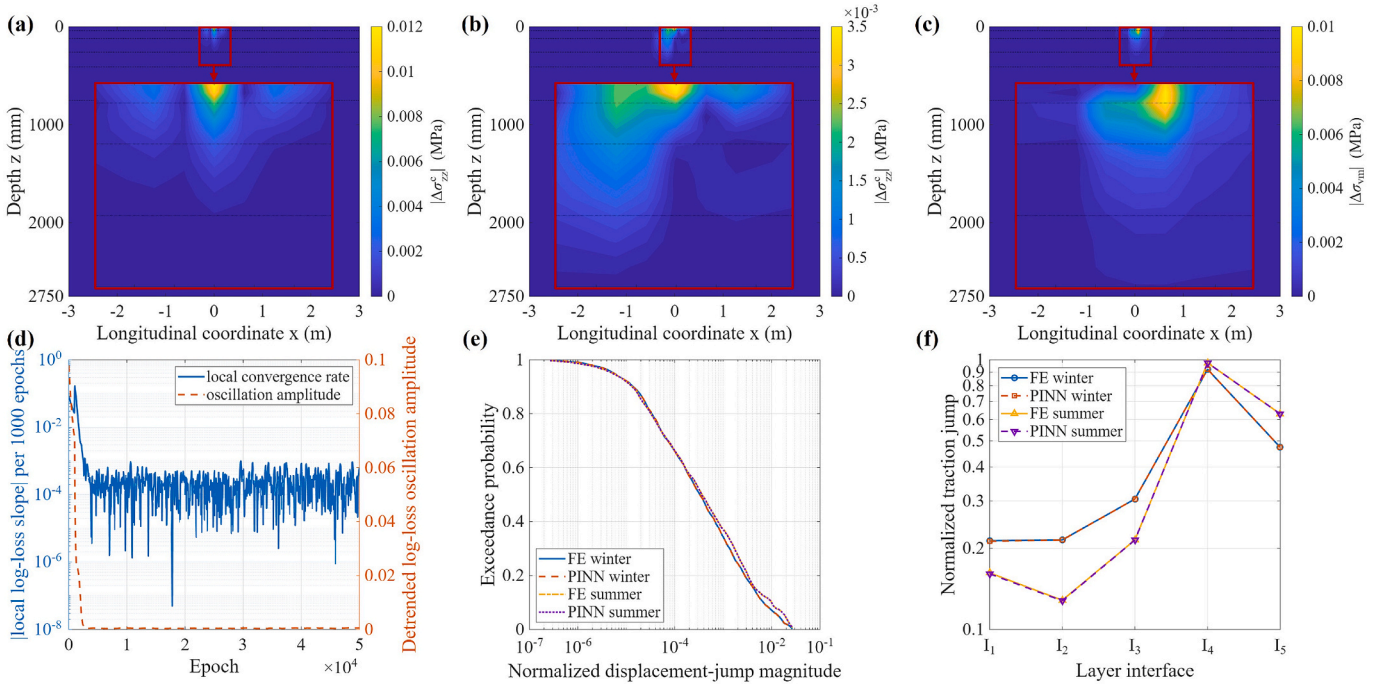


Fig. 7. Absolute reconstruction errors, convergence evidence, and interface continuity diagnostics: (a) winter absolute error in vertical compressive stress $|\Delta\sigma^c_{zz}|$, (b) summer absolute error in vertical compressive stress $|\Delta\sigma^c_{zz}|$, (c) winter absolute error in von Mises stress $|\Delta\sigma_{vm}|$, (d) local convergence rate and detrended loss-oscillation amplitude during PINN training, (e) exceedance probability of normalized displacement jump across bonded interfaces, and (f) normalized traction jump across the bonded interfaces I_1-I_5 associated with Eq. (8).

The interface diagnostics in Fig. 7 (e) and (f) evaluate whether the reconstructed fields remain compatible with the bonded-layer conditions. The exceedance-probability curves of normalized displacement jump in Fig. 7 (e) show close agreement between FE and PINN for both seasons across the full threshold range. The displacement-jump distribution is therefore reproduced not only in an average sense but also in its tail behavior, which is important for assessing rare but mechanically significant mismatch events. The traction-jump results in Fig. 7 (f) further demonstrate that the reconstructed interface tractions follow the FE trend closely across all interfaces. The largest normalized traction jump occurs at I_4, whereas the smaller values at I_1 and I_2 indicate comparatively smaller discontinuities at the upper bonded interfaces.

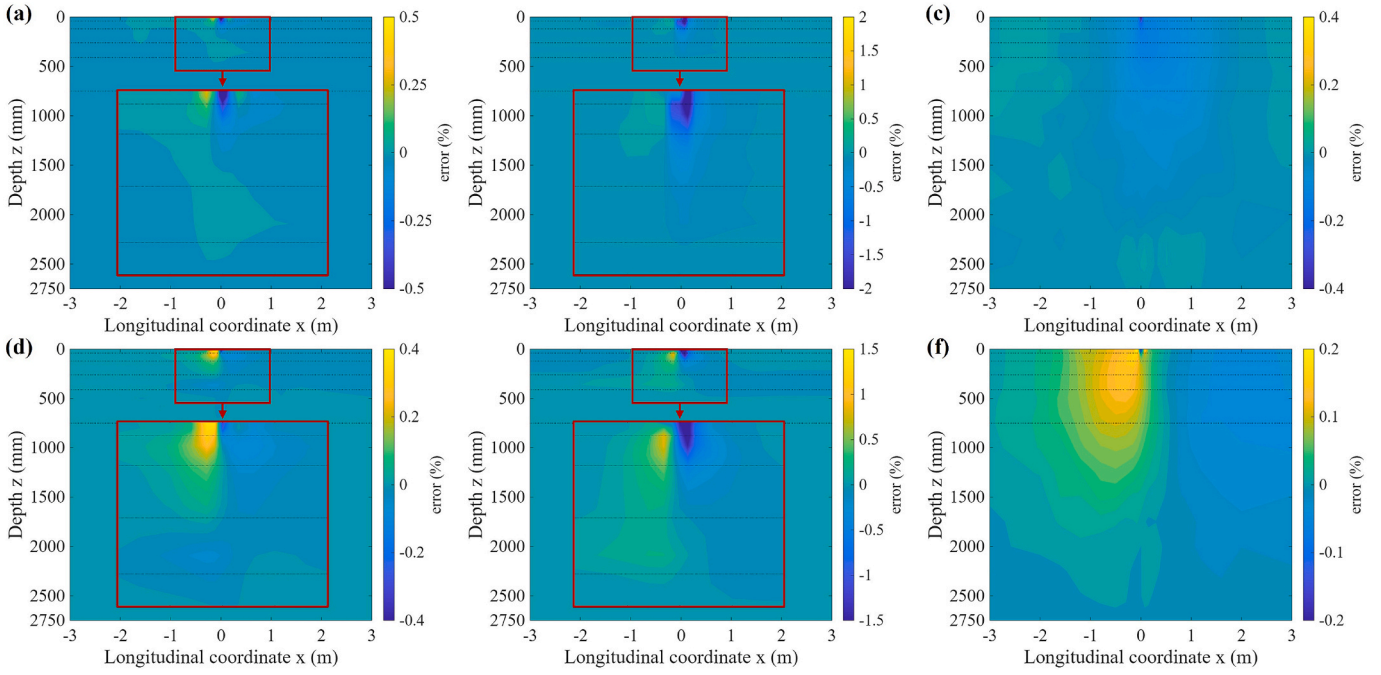


Fig. 8. Spatial reconstruction-error maps for PINN-predicted mechanical fields under the same source-disjoint blind load: (a) winter normalized error of mean compressive stress p_m, (b) winter normalized error of $\sqrt{J_2}$, (c) winter normalized error of vertical deflection u_z, (d) summer normalized error of p_m, (e) summer normalized error of $\sqrt{J_2}$, and (f) summer normalized error of u_z.

The close alignment of the FE and PINN curves confirms that the interface continuity constraints are effectively enforced in the reconstructed displacement and stress fields, rather than being satisfied only in a global or averaged sense.

Fig. 8 evaluates the spatial distribution of PINN reconstruction errors for three representative mechanical quantities: the mean compressive stress p_m, the second-invariant stress intensity $\sqrt{J_2}$, and the vertical deflection u_z. Here, p_m represents the mean compressive component of the three-dimensional normal stress state, whereas $\sqrt{J_2}$ characterizes the intensity of the deviatoric response. The pointwise PINN–FE differences are normalized by the maximum absolute magnitude of the corresponding FE field and expressed as percentages. The winter and summer results are obtained under the same source-disjoint blind load, so their differences primarily reflect the seasonal material states. Overall, the errors remain small, although their magnitude and spatial organization depend on the selected response quantity.

The p_m error fields in panels (a) and (d) are concentrated mainly beneath the contact center and within the upper pavement layers, where the compressive stress varies most rapidly. The winter error remains largely within approximately ±0.5%, while the summer distribution is slightly narrower. The u_z errors in panels (c) and (f) are more diffuse and substantially lower in magnitude, remaining within approximately ± 0.4% and ±0.2%, respectively. This comparatively smooth distribution is consistent with the spatially integrated nature of displacement, which is less sensitive to localized variations than stress-derived quantities.

The $\sqrt{J_2}$ error fields exhibit the most pronounced spatial structure. In panel (b), the winter error reaches approximately ±2.0% near the load axis and extends through the upper and intermediate layers, whereas the summer error in panel (e) remains within approximately ±1.5%. The adjacent positive and negative regions indicate small differences in the reconstructed partition of lateral, vertical, and shear stresses rather than a uniform overprediction or underprediction. These deviations are strongest near the contact zone and layer transitions, where the deviatoric stress state is particularly sensitive to local gradient changes. Despite this increased sensitivity, the errors remain spatially localized, confirming that the PINN preserves the dominant stress-transfer and deformation patterns of the FE reference solution.

Fig. 9 examines the footprint-level reconstruction errors of the mixed tire–pavement contact-traction field. The primary source quantities are the total normal pressure p_n, the resultant traction magnitude, and the longitudinal and lateral traction components q_x and q_y. Here, p_n represents the mechanically identifiable normal traction acting over the contact patch, whereas the resultant magnitude combines the normal and two tangential traction components. The quantities q_x and q_y characterize the longitudinal braking-related and lateral-slip-related contributions, respectively. The errors in panels (a)–(c) remain within approximately ±5%, while the q_y error in panel (d) is confined to a much narrower range of about ±0.2%.

The normal-pressure error in panel (a) exhibits a spatially alternating pattern with negative regions near the footprint center and positive lobes toward the surrounding contact area. This distribution indicates that the resultant normal load is well preserved, while small local differences remain in the reconstructed pressure heterogeneity. The error in the resultant traction magnitude in panel (b) follows a similar spatial organization because the normal component dominates the total contact traction. Nevertheless, the close agreement does not imply identical quantities, since the resultant magnitude also contains the effects of q_x and q_y. The longitudinal-traction error in panel (c) is predominantly negative over the central footprint, suggesting a slight local underestimation of the braking-related traction amplitude. In contrast, the lateral-traction error in panel (d) is much smaller and varies smoothly across the contact region, indicating stable recovery of the weaker lateral source component.

Panels (e) and (f) assess higher-order spatial descriptors derived from the reconstructed traction distribution. The pressure-centroid

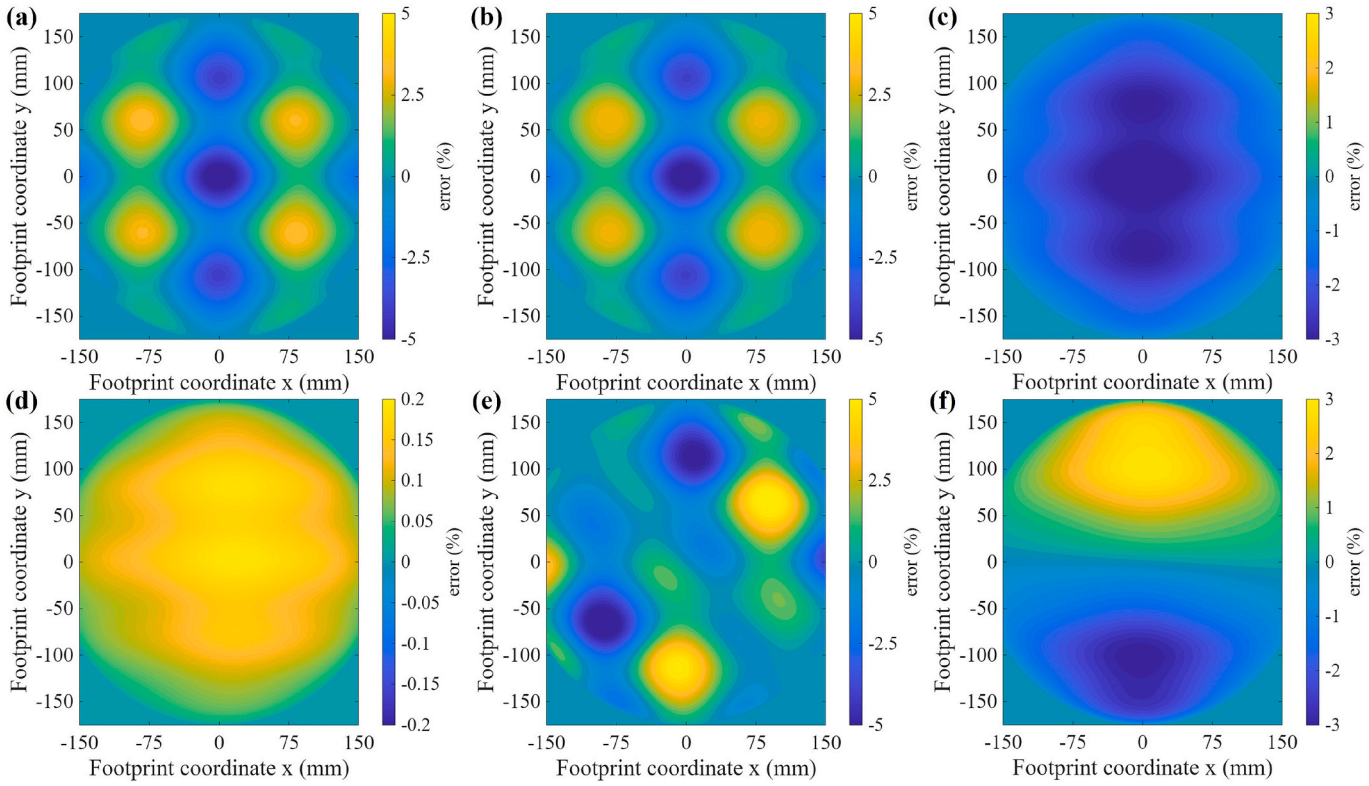


Fig. 9. Mixed tire–pavement contact-traction reconstruction errors over the footprint: (a) error in total normal pressure p_n, (b) error in resultant contact-traction magnitude, (c) error in longitudinal traction q_x, (d) error in lateral traction q_y, (e) error in the pressure-centroid contribution, and (f) error in the local moment-density reconstruction.

contribution in panel (e) displays alternating positive and negative regions, showing that small local pressure errors can produce spatially structured deviations in the first moment of the normal traction. The local moment-density error in panel (f) changes sign across the lateral direction, which is consistent with the directional nature of the in-plane traction moment about the out-of-plane axis. Despite their greater sensitivity to spatial redistribution, both derived quantities remain bounded and free of pronounced boundary artifacts. Overall, Fig. 9 demonstrates that the inverse formulation recovers not only the global contact resultants but also the internal spatial organization and higher-order moment characteristics of the mixed traction source.

Fig. 10 evaluates the proposed inverse framework under a source-disjoint blind load that was excluded from both network training and model selection. The FEM and PINN winter fields in panels (a) and (b) exhibit nearly identical lateral–depth distributions of mean compressive stress p_m. The response is concentrated beneath the contact center, with a near-surface maximum approaching 1.2 MPa and rapid attenuation with depth and lateral distance. The reconstructed field preserves the location, width, and depthwise decay of the compressive core, indicating that the inverse model can recover the internal stress response associated with a previously unseen loading combination.

Panels (c) and (d) provide the corresponding comparison for the summer vertical strain ε_{zz}. Both fields contain a vertically elongated compressive-strain zone beneath the load axis, with the strongest response close to -1.0×10^{-4}. The vertically elongated summer strain zone extends into the supporting layers, consistent with the increased deformation associated with the reduced asphalt-layer stiffness. The close correspondence between the FEM and PINN contours shows that the reconstruction retains both the near-surface strain concentration and the broader depthwise deformation pattern.

The agreement map in panel (e) combines the local consistency of mean stress, lateral–depth shear stress, and vertical displacement. The index remains above approximately 0.996 throughout the section and approaches unity over most of the deeper domain. The relatively lower values are confined mainly to the contact region and upper pavement layers, where stress and displacement gradients are strongest. This spatial pattern indicates that the largest FEM–PINN differences occur in mechanically sensitive zones rather than as a systematic domain-wide bias.

Panel (f) quantifies the observation sparsity associated with different probe-by-phase configurations. Increasing the configuration from 4×5 to 8×9 raises the point sparsity ratio from approximately 0.09% to 0.34%, while the scalar-observation ratio increases from about 0.38% to 1.35%. Even the densest configuration therefore uses only a small fraction of the total mechanical degrees of freedom. These sparsity levels are consistent with the practical constraint that instrumented pavements generally rely on a limited number of embedded sensors rather than dense full-field measurements, owing to installation, durability, and maintenance considerations reported in recent pavement sensing studies (Zheng et al., 2025; Zheng et al., 2026). The blind-load reconstruction obtained under these sparse conditions demonstrates that the response field is constrained by the combined information supplied by the observations and the embedded mechanics, rather than by dense full-field measurements. This result suggests that the proposed framework remains compatible with sensor densities that are achievable in practical pavement structural health monitoring systems.

To further validate the adaptability of the proposed PINN framework, additional comparisons were performed against published experimental data reported in Elseifi et al. (2006). This benchmark is independent of the main numerical dataset and uses a different parameter combination, thereby providing an external assessment of whether the inverse reconstruction framework remains effective beyond the scenarios used for model development. Fig. 11 compares the PINN predictions, the corresponding FEM results, and the benchmark observations at both the field and response levels.

The benchmark reported in Elseifi et al. (2006) was used to provide an additional response-level comparison under moving wheel loading. Although the reference study employed a viscoelastic description of the asphalt layers, the considered response corresponds to a short-duration wheel passage under relatively low stress and strain levels. Within this loading regime, the pavement response remains predominantly within the approximately linear range, so that an elastic representation based

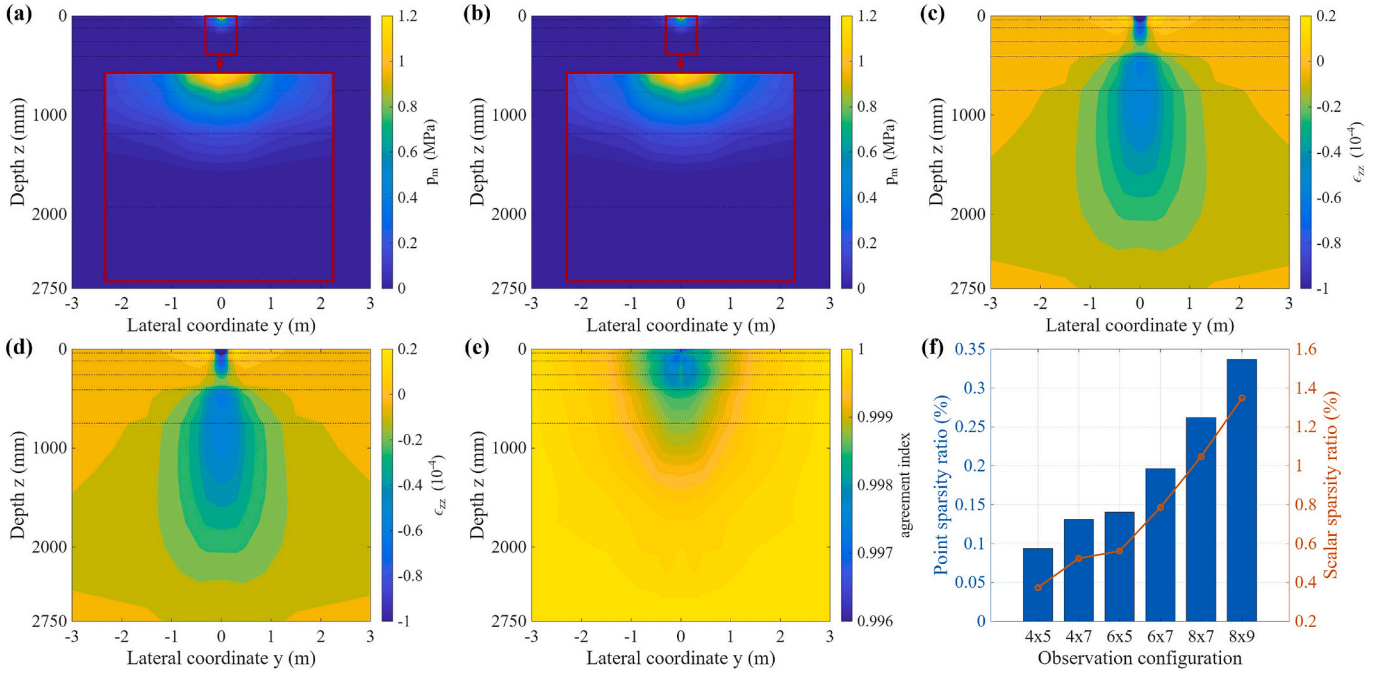


Fig. 10. Source-disjoint blind-load reconstruction, physics-constrained agreement, and observation sparsity: (a) FEM winter mean compressive stress p_m in the central y-z section under an unseen reconstruction load, (b) corresponding PINN reconstruction of p_m, (c) FEM summer vertical strain ε_{zz} under an unseen reconstruction load, (d) corresponding PINN reconstruction of ε_{zz}, (e) spatial distribution of the composite FEM–PINN physics-constrained agreement index, and (f) point and scalar sparsity ratios for different probe-by-phase observation configurations.

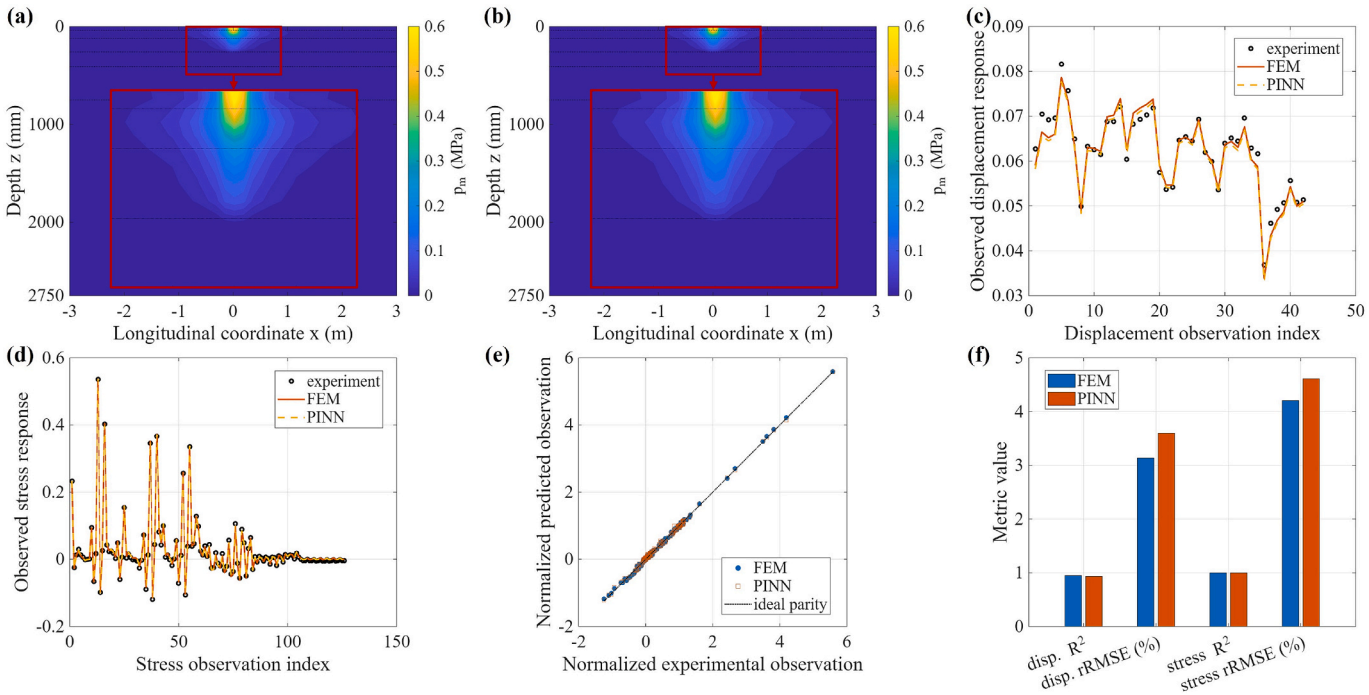


Fig. 11. Comparison of the proposed PINN framework with published experimental–numerical benchmark data: (a) FEM mean compressive stress p_m in the central x-z section for the independent benchmark case, (b) corresponding PINN reconstruction of p_m, (c) digitized experimental and model-computed displacement observations, (d) digitized experimental and model-computed stress observations, (e) parity comparison between normalized experimental observations and the corresponding FEM and PINN predictions, and (f) relative root-mean-square error (rRMSE) and coefficient of determination (R^2) for the displacement and stress responses.

on an effective modulus can reproduce the principal response magnitude and transient trend with only limited deviation from the short-term viscoelastic response. The comparison is therefore used to assess response consistency at the structural level rather than to reproduce the full time-dependent constitutive behavior reported in Elseifi et al. (2006). No additional viscoelastic parameters were introduced for this comparison.

The mean compressive stress fields in Fig. 11 (a) and (b) show that the PINN reconstruction preserves the essential structure of the FEM benchmark solution. In both cases, p_m is strongly concentrated beneath the contact region, with a near-surface maximum approaching 0.6 MPa and a gradual attenuation with depth. The reconstructed field reproduces the depthwise transfer path and the lateral diffusion of the compressive core with only minor visual differences. This agreement indicates that the proposed framework is capable of recovering the dominant internal stress state associated with an external benchmark case that is not part of the original reconstruction scenarios.

The response-level comparisons in Fig. 11 (c) and (d) further support this conclusion. For the displacement observations, both the FEM and PINN curves closely follow the digitized experimental trend over the full observation sequence, including the local peaks and the pronounced reduction in the later observations. A similarly close agreement is obtained for the stress response, where the measured fluctuations and sharp local peaks are reproduced with high fidelity. The parity plot in Fig. 11 (e) shows that both sets of predictions cluster closely around the ideal $y = x$ line over a broad normalized range, confirming that the agreement is not limited to either low- or high-response regions.

The quantitative metrics in Fig. 11 (f) indicate that both models achieve high explanatory power, with R^2 values remaining close to unity for both displacement and stress. The relative errors are also small, remaining on the order of only a few percent. The FEM benchmark is marginally more accurate, which is expected because it acts as the direct forward reference for the published case. Nevertheless, the PINN achieves a closely comparable level of accuracy while reconstructing the response through the inverse framework. Taken together, these results show that the proposed PINN retains good predictive consistency when confronted with independent published experimental–numerical data, thereby supporting its adaptability and external validity.

3.2. *Seasonal layered pavement response and mixed contact traction transfer mechanisms*

This subsection interprets the seasonal pavement response and the transfer of mixed contact traction through the layered structure. The winter and summer material states are evaluated under matched blind-loading conditions so that differences in stress diffusion, strain localization, shear redistribution, vertical deflection, and energy storage can be attributed primarily to the asphalt stiffness contrast. Finite-domain, contact-source-basis, interface, moving-load, and layer-integral diagnostics are then used to quantify boundary attenuation, transient pulse broadening, interlayer transfer, and the partition of stress and deformation among the pavement layers. Damage-related proxies further illustrate how the seasonal material states redistribute fatigue and rutting tendencies through the pavement depth.

Fig. 12 shows the winter pavement response under the reconstructed mixed tire–pavement contact traction, for which the relatively high asphalt-layer stiffness produces a confined near-surface stress-transfer region. The mean compressive stress p_m in panel (a) is strongly concentrated beneath the contact center and attenuates rapidly with increasing depth and longitudinal distance. The maximum value approaches 0.8 MPa near the surface, whereas the response becomes substantially weaker below the upper pavement structure. The longitudinal compressive stress σ^c_{xx} in panel (b) exhibits a more complex signed distribution, including a localized compressive region beneath the load and a weaker stress-redistribution zone at greater depth. This difference indicates that the mean compressive response is governed primarily by the direct normal-load transfer, while σ^c_{xx} additionally reflects longitudinal confinement and layer-dependent stress

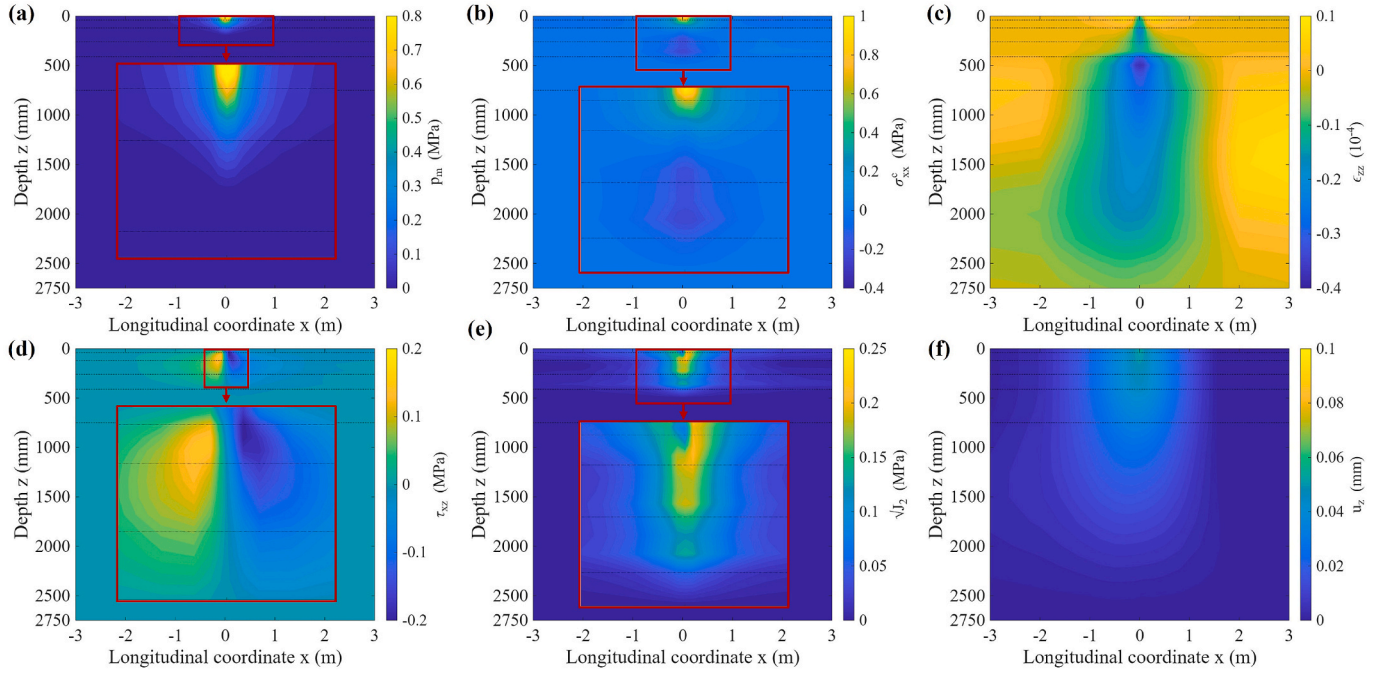


Fig. 12. Winter finite-layer pavement response under reconstructed mixed tire–pavement contact traction in the central x-z section: (a) mean compressive stress p_m, (b) longitudinal compressive stress σ^c_{xx}, (c) vertical strain ε_{zz}, (d) longitudinal–depth shear stress τ_{xz}, (e) second-invariant stress intensity $\sqrt{J_2}$, and (f) vertical deflection u_z.

redistribution.

The vertical strain ε_{zz} in panel (c) forms an elongated compressive zone beneath the tire footprint, with the strongest response extending below the upper asphalt layers rather than remaining confined to the pavement surface. This pattern reflects the stiffness contrast between the asphalt courses and the more compliant supporting layers: the near-surface structure sustains relatively high stress, whereas deformation accumulates progressively with depth. The shear stress τ_{xz} in panel (d) changes sign across the central loading path and develops two opposing lobes within the upper-to-intermediate depth range. This distribution is consistent with longitudinal shear transfer around the boundary of the compressive stress bulb and highlights the role of the tangential contact component in redistributing load away from the contact center.

The second-invariant stress intensity $\sqrt{J_2}$ in panel (e) identifies a vertically extended deviatoric-stress corridor beneath the load, with local amplification near the upper layers and around stiffness transi-

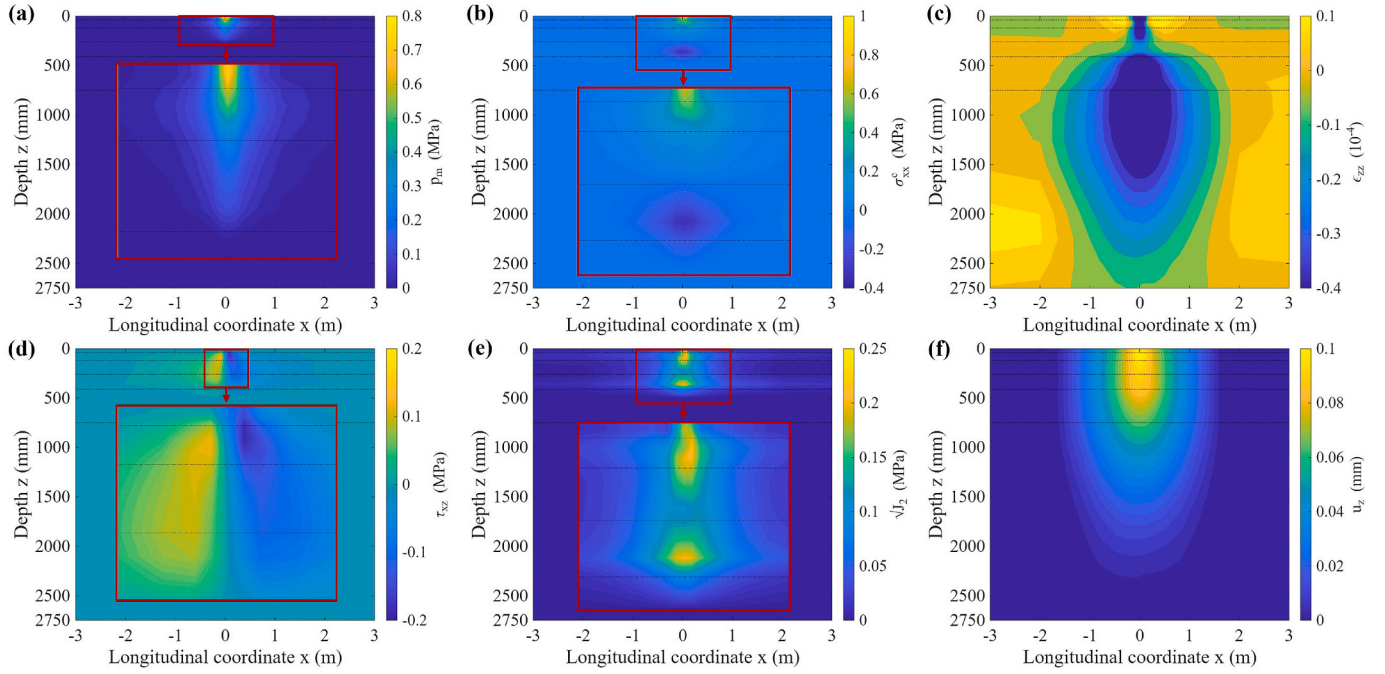


Fig. 13. Summer finite-layer pavement response under the same source-disjoint mixed tire–pavement contact load used for the winter case: (a) mean compressive stress p_m, (b) longitudinal compressive stress σ^c_{xx}, (c) vertical strain ε_{zz}, (d) longitudinal–depth shear stress τ_{xz}, (e) second-invariant stress intensity $\sqrt{J_2}$, and (f) vertical deflection u_z, all shown in the central x-z section.

tions. Its distribution is more spatially structured than p_m, because it incorporates the combined contributions of normal- and shear-stress differences. Panel (f) shows a smooth vertical-deflection basin centered beneath the load, with a maximum of approximately 0.1 mm and gradual attenuation toward the longitudinal boundaries and lower layers. Overall, the winter response is characterized by strong near-contact stress localization, limited deformation, and a coherent transition from localized surface loading to distributed stress and strain transfer through the layered pavement system.

Fig. 13 presents the summer response of the finite-layer pavement under the same source-disjoint mixed tire–pavement contact load used for the winter case in Fig. 12, but with the lower asphalt-layer moduli assigned to the summer material state. The mean compressive stress p_m in panel (a) remains concentrated beneath the contact center, while its transfer path extends continuously through the upper pavement structure. Although the near-surface magnitude is comparable to that of the winter case because the external loading parameters are identical, the softened asphalt courses alter the depthwise diffusion of the compressive field. The longitudinal compressive stress σ_{xx}^{c} in panel (b) exhibits a localized compressive region beneath the load and a weaker opposite-signed redistribution zone at greater depth, reflecting the combined effects of longitudinal confinement and stiffness contrast between adjacent layers.

The vertical strain ε_{zz} in panel (c) develops a substantially broader and more intense compressive zone than in the winter state. Its strongest negative values extend from the asphalt layers into the supporting structure, demonstrating that the reduced summer stiffness produces greater deformation under the same applied contact traction. The longitudinal–depth shear stress τ_{xz} in panel (d) retains the sign-changing structure across the central load path, but the two shear lobes occupy a wider and deeper region. This broader distribution indicates enhanced transfer of tangential and normal-load effects between the softened upper courses and the underlying layers.

The second-invariant stress intensity $\sqrt{J_2}$ in panel (e) forms a continuous deviatoric-stress corridor beneath the contact center, with local amplification near the surface and around the deeper layer transitions. Compared with the winter result, the summer field shows a more pronounced involvement of the lower supporting structure, indicating that seasonal softening modifies the partition of multiaxial stress through the pavement depth. The vertical deflection u_z in panel (f) forms a broad, smooth basin with a maximum close to 0.1 mm and a gradual decay toward the bottom and longitudinal boundaries. Overall, the summer response is characterized by stronger and deeper strain localization, broader shear redistribution, and more extensive deformation transfer, whereas the winter state exhibits comparatively confined deformation under the matched external load.

Fig. 14 assesses the sensitivity of the mechanical response and inverse reconstruction to finite-domain size, contact-source representation, boundary attenuation, interface transfer, and regularization. Panel (a) shows that the maximum von Mises stress σ_{vm}^{max} changes only slightly as the domain half-width increases from 1.2 to 3.0 m. The relative change in σ_{vm}^{max} decreases progressively toward zero, whereas the relative change in u_z^{max} first increases at intermediate domain sizes and then falls rapidly as the largest domain is approached. This nonmonotonic displacement response reflects the greater sensitivity of the accumulated deformation field to finite-boundary placement. Nevertheless, both measures converge at a half-width of 3.0 m. Panel (c) further shows that the far-boundary displacement ratio remains below approximately 0.10. The winter profile reaches a moderate maximum at intermediate depth, while the summer ratio decreases more continuously toward the bottom boundary, indicating that the selected domain adequately limits boundary contamination.

Panel (b) examines the approximation stability of the contact-source basis. Increasing the basis order from 2 to 20 reduces both the normal- and shear-field reconstruction errors from approximately 15% to below 2%, with the greatest improvement occurring at the lower orders. In contrast, the edge-gradient oscillation index decreases initially but then increases progressively with source complexity. The result therefore reveals a trade-off: higher-order bases improve the representation of the

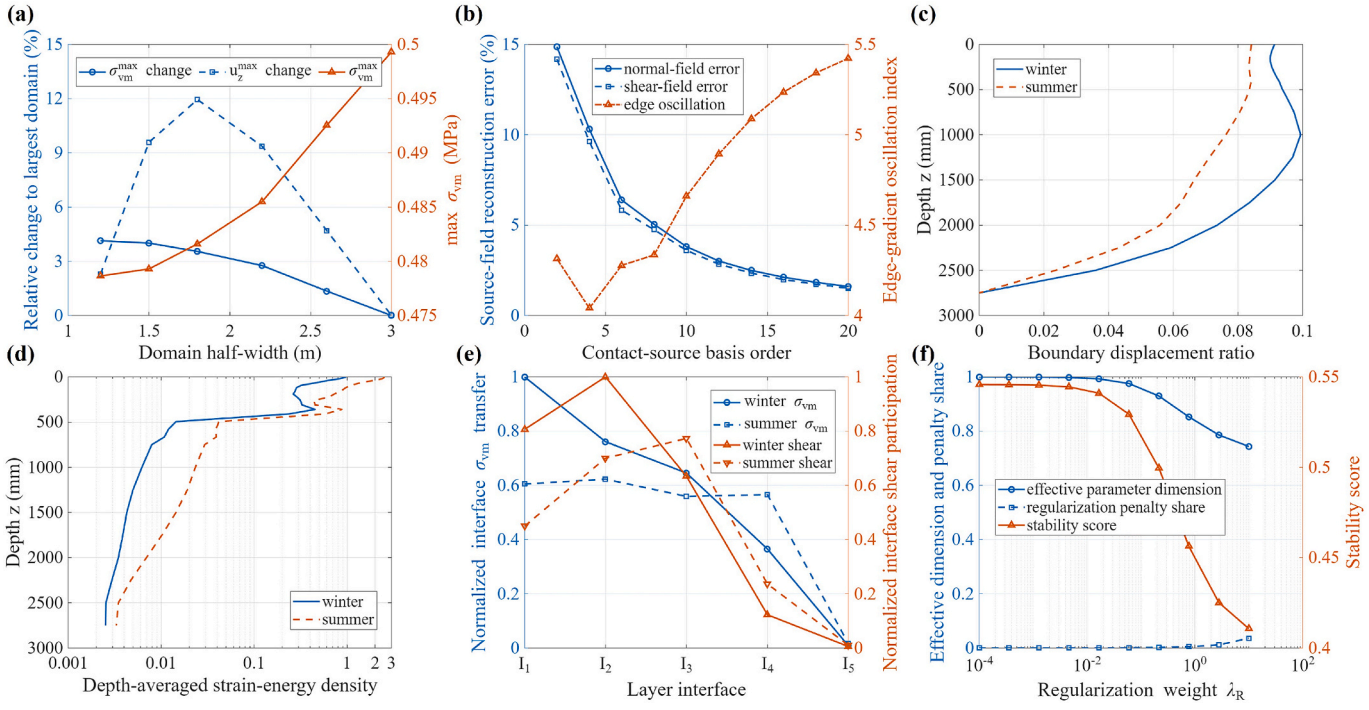


Fig. 14. Finite-domain, contact-source, interface-transfer, and regularization-stability diagnostics: (a) sensitivity of the maximum von Mises stress σ_{vm}^{max} and maximum vertical deflection u_z^{max} to domain half-width, (b) normal- and shear-field reconstruction errors and edge-gradient oscillation for different contact-source basis orders, (c) far-boundary displacement attenuation, (d) depth-averaged strain-energy density, (e) normalized interface transfer of von Mises stress and shear participation, and (f) effective parameter dimension, regularization-penalty share, and stability score as functions of the regularization weight λ_R.

interior traction field but also increase sensitivity to oscillatory gradients near the contact boundary. A moderate basis order consequently provides a more balanced representation than unrestricted enrichment. Panel (d) presents the depth-averaged strain-energy density. Both seasonal profiles are concentrated in the upper pavement structure, but the summer response remains larger over a greater depth, consistent with the stronger deformation penetration produced by the reduced asphalt-layer stiffness.

Panel (e) compares the normalized interface transfer of von Mises stress and shear participation. The winter σ_{vm} transfer decreases continuously from I_1 to I_5, whereas the summer response remains comparatively stable through the upper and intermediate interfaces before dropping sharply at I_5. The shear contribution is largest at I_2 for winter and at I_3 for summer, demonstrating that seasonal stiffness changes shift the dominant shear-transfer region toward deeper interfaces. Panel (f) shows that the effective parameter dimension remains close to unity under weak regularization and decreases as λ_R increases, while the regularization-penalty share rises gradually. The stability score remains nearly unchanged at small λ_R but declines markedly under strong regularization. Excessive penalization therefore suppresses the effective inverse degrees of freedom and reduces reconstruction stability, whereas weak-to-moderate regularization preserves a more favorable balance between parameter flexibility and physics-based control.

The spatial and temporal discretization checks in Fig. 15 (a) and (b) establish the numerical resolution required for the transient FE reference solution. The coarse meshes exhibit appreciable sensitivity and some non-monotonic variation, particularly for the peak vertical compressive stress, reflecting the difficulty of resolving the localized moving contact footprint with insufficient spatial resolution. This sensitivity contracts markedly as the number of degrees of freedom increases, and both the stress and displacement responses approach the refined-mesh reference in the higher-resolution range. A similar pattern is observed for the time increment: relatively large deviations occur for the coarsest temporal discretizations, whereas the response becomes substantially less sensitive once the time increment is reduced to the range used in the main analysis. These results indicate that the adopted FE discretization lies within the converged response regime rather than within the strongly resolution-dependent coarse-mesh range.

The transient histories in Fig. 15 (c) and (d) distinguish the primary moving-load response from the later wave-dominated response. The standard truncation and viscous-buffer solutions remain closely aligned over the principal near-surface displacement pulse, indicating that the mechanically dominant response generated during tire passage is only weakly affected by the additional boundary dissipation. Differences become more apparent in the deep-subgrade particle velocity after the primary pulse has passed, where alternating velocity peaks reveal the arrival and superposition of reflected wave components. The extended-domain case produces a broader response envelope because domain enlargement and additional viscous treatment alter the propagation path and dissipation of these later waves; it is therefore more appropriately interpreted as a conservative boundary-sensitivity comparison than as an identical-domain solution.

This distinction is reinforced by the depthwise and spectral diagnostics in Fig. 15 (e) and (f). The late-window RMS particle velocity generally increases toward the deeper subgrade, showing that boundary sensitivity is concentrated much more strongly in the wave field near the truncated lower region than in the primary surface response. The frequency spectra likewise show that the boundary treatments mainly modify selected late-time frequency components rather than producing a uniform amplification of the complete transient response. Taken together, the results demonstrate that finite-boundary reflections are detectable in the late deep-subgrade response, but their influence is separated from the principal tire-induced response used to characterize the near-surface and structural load-transfer behavior. This wave-based assessment therefore complements the displacement-ratio truncation analysis in Fig. 14 and provides a more direct verification of the

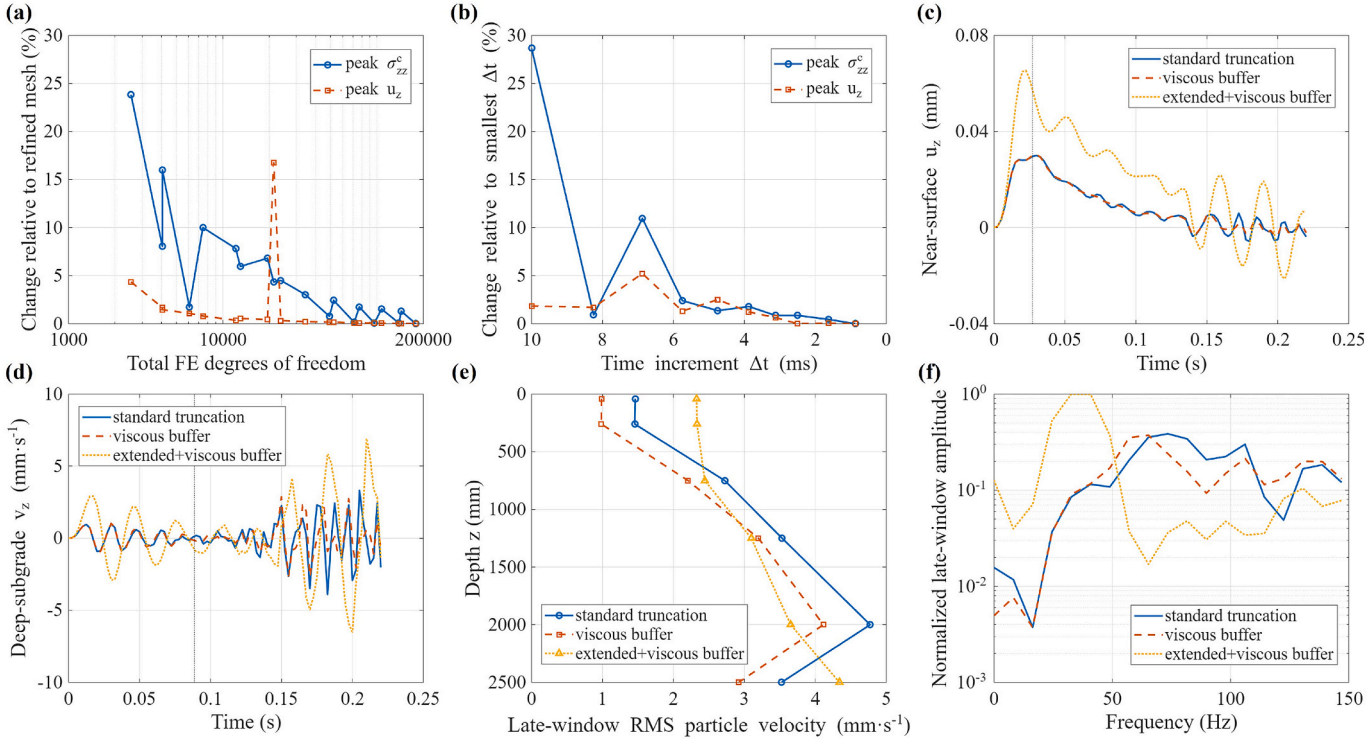


Fig. 15. Finite-element discretization convergence and transient boundary-reflection assessment: (a) spatial-mesh convergence of peak vertical compressive stress and vertical deflection, (b) time-step convergence of the corresponding peak responses, (c) near-surface vertical-displacement histories under standard truncation, a viscous buffer, and an extended domain with a viscous buffer, (d) deep-subgrade vertical particle-velocity histories, (e) depthwise distribution of late-window RMS particle velocity, and (f) normalized late-window frequency spectra of the deep-subgrade response.

transient FE setup.

Fig. 16 characterizes how the different contact-source modes are transferred from the tire footprint into the layered pavement during moving-load passage. Panel (a) presents the response-coupling matrix for the normal, normal-pressure heterogeneity, longitudinal-shear, lateral-shear, and mixed modes. The unit diagonal confirms the self-consistency of each modal response, whereas several off-diagonal entries remain substantial. In particular, the normal and mixed modes exhibit very strong coupling, indicating that the mixed response retains a dominant normal-loading contribution. The normal-pressure heterogeneity mode is also closely coupled with the two shear modes. These results show that the source components are not mechanically independent after transmission through the layered medium, and that their reconstructed signatures must be distinguished through their combined spatial and temporal characteristics.

Panels (b) and (c) quantify the depth-integrated work partition and the depth-shape entropy of the five source modes. The normal and mixed modes provide the largest work contributions in both seasons, each accounting for approximately one-third of the total response. The longitudinal-shear mode forms the next most important contribution, whereas the lateral-shear mode is weaker and the isolated pressure-heterogeneity mode contributes only a small fraction of the integrated work. The entropy results reveal a similarly mode-dependent hierarchy. The normal and mixed modes have the broadest depth distributions, while the two shear modes and the pressure-heterogeneity mode remain more localized. Seasonal softening generally increases the depth-shape entropy of the non-normal modes, indicating that the summer structure permits a wider vertical redistribution of pressure heterogeneity and tangential loading effects.

Panels (d) and (e) describe the attenuation and temporal spreading of the moving-load response. The interface-transfer ratio decreases sharply below the upper interfaces, although local nonmonotonic variations occur where stiffness contrasts redistribute the stress path. The winter and summer curves remain close near the surface but differ at intermediate depths, showing that seasonal stiffness affects the partition of load transfer across individual interfaces rather than producing a uniform scaling of the response. The pulse width at half maximum remains relatively narrow through the upper and middle layers and increases at greater depth. The deepest winter response exhibits the most pronounced broadening, whereas the summer curve remains comparatively compact at the lowest diagnostic positions. Panel (f) further shows that the winter–summer contrast is concentrated primarily between depths of approximately 400 and 900 mm and varies throughout the load-passage interval. The alternating positive and negative bands reflect seasonal differences in pulse timing and amplitude, rather than unstable propagation.

Fig. 17 summarizes the layer-integrated contributions and depth-dependent transfer characteristics of the principal mechanical responses. The layer contribution $\mathscr{I}_\ell[\sigma_{\mathrm{vm}}]$ in panel (a) is obtained by integrating the von Mises stress within each layer and normalizing it by the corresponding integral over the entire pavement depth. The road base provides the largest contribution in both seasons, and its share increases from approximately 0.32 in winter to 0.42 in summer. The binder and asphalt base courses also retain appreciable contributions, whereas those of the sub-base and subgrade remain comparatively small. This distribution indicates that the multiaxial stress activity is transferred beyond the asphalt courses and becomes concentrated within the road-base-supported load path. In contrast, panel (b) shows that the vertical-strain activity $\mathscr{I}_\ell[\varepsilon_{zz}]$ is overwhelmingly concentrated in the subgrade, with the sub-base providing the second-largest contribution and the upper four layers accounting for only a minor fraction. The results distinguish the layers responsible for stress transfer from those accommodating most of the vertical deformation.

Panel (c) presents the centroid depths of four representative mechanisms. The centroid of σ_{zz} is the deepest, at approximately 1.25 m, followed by that of p_m near 1.0 m, whereas the centroids of σ_{vm} and $|\tau_s|$ remain within the upper several hundred millimeters. All four summer centroids are slightly deeper than their winter counterparts, with the most visible shifts occurring for σ_{vm} and $|\tau_s|$. This confirms that seasonal softening promotes downward redistribution of both deviatoric and

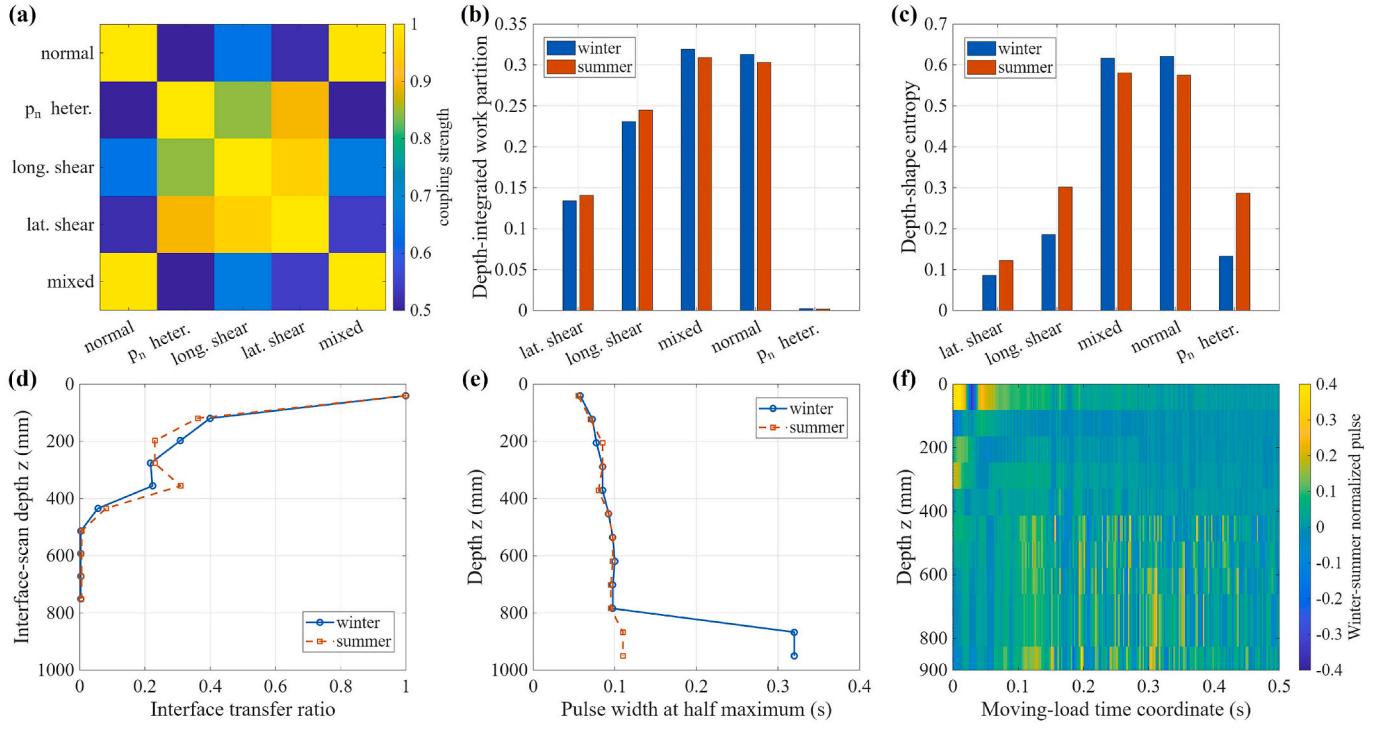


Fig. 16. Contact-source coupling and depth-response diagnostics under moving-load sampling: (a) response-coupling matrix for the normal, normal-pressure heterogeneity, longitudinal-shear, lateral-shear, and mixed source modes; (b) depth-integrated work partition of the source modes; (c) modal depth-shape entropy; (d) interface-transfer attenuation with depth; (e) load-pulse width at half maximum; and (f) winter–summer depth–time contrast of the normalized transient response.

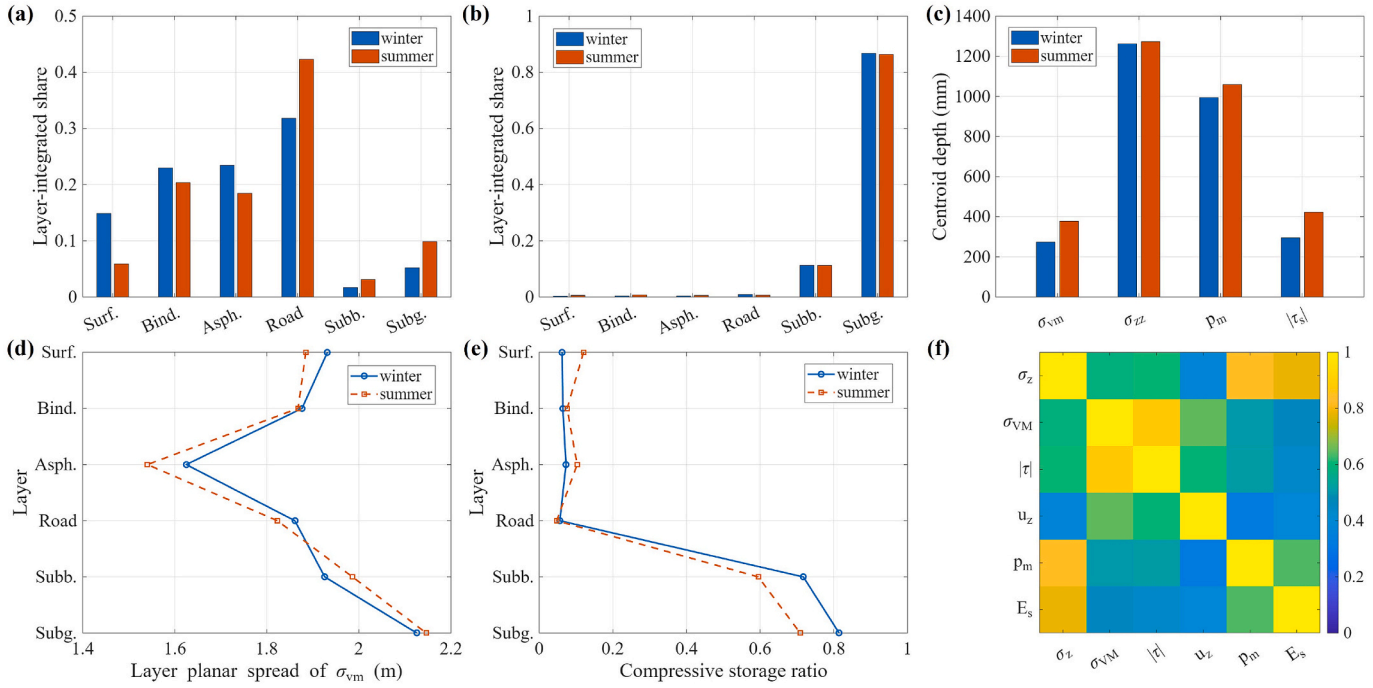


Fig. 17. Layer-integrated descriptors and depth-dependent transfer mechanisms: (a) layer contribution to the von Mises stress integral $\mathscr{I}_\ell[\sigma_{vm}]$, (b) layer contribution to vertical-strain activity $\mathscr{I}_\ell[\varepsilon_{zz}]$, (c) centroid depths of σ_{vm}, σ_{zz}, p_m, and $|\tau_s|$, (d) layerwise planar spread of σ_{vm}, (e) layerwise compressive storage ratio, and (f) correlation structure among the principal mechanical and seasonal-stiffness descriptors.

shear-related responses. Panel (d) further shows that the planar spread of σ_{vm} varies nonmonotonically among layers. It narrows within the asphalt base, then increases through the lower supporting layers and reaches its largest value in the subgrade. The summer response is slightly narrower in the upper and intermediate layers but marginally broader in the sub-base and subgrade.

The compressive storage ratio in panel (e) remains small throughout the asphalt and road-base layers, but increases sharply in the sub-base and subgrade. The winter values in these lower layers are somewhat larger than the summer values, indicating that seasonal softening changes not only the deformation magnitude but also its partition between the supporting courses. The correlation map in panel (f) reveals

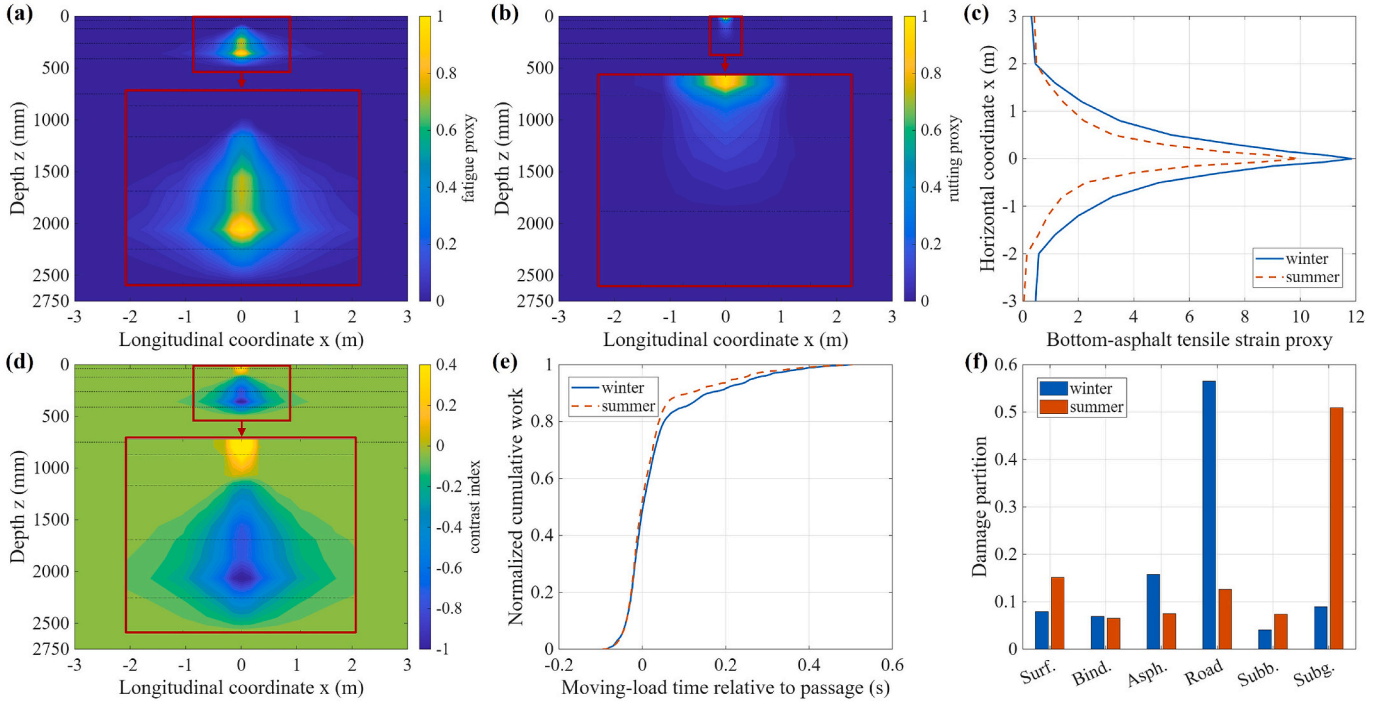


Fig. 18. Mechanistic fatigue, rutting, and seasonal damage-transfer diagnostics: (a) winter fatigue-driving strain–stress proxy, (b) summer rutting-driving compressive proxy, (c) bottom-asphalt tensile-strain corridor, (d) summer-to-winter damage-mechanism contrast, (e) normalized cumulative damage work during one moving-load passage, and (f) layerwise mechanistic damage partition.

strong coupling between σ_{vm} and $|\tau|$, and between σ_{zz} and p_m, reflecting the close association of deviatoric stress with shear transfer and of vertical stress with volumetric compression. The seasonal stiffness descriptor E_s is more strongly related to the normal and compressive stress measures than to u_z, whereas deflection exhibits a more distributed dependence on several descriptors. Overall, Fig. 17 demonstrates a clear mechanical partition: stress intensity is concentrated mainly within the road-base transfer path, vertical-strain activity is stored predominantly in the lower supporting layers, and summer softening shifts several response mechanisms toward greater depths.

Fig. 18 summarizes the seasonal damage mechanisms derived from the reconstructed mechanical fields and demonstrates that the winter and summer states activate distinct deterioration pathways. The winter fatigue-driving strain–stress proxy in panel (a) exhibits a localized upper-layer hotspot together with a deeper vertically connected corridor beneath the load center. The pronounced response around the road-base region indicates that the winter condition promotes fatigue-related stress transmission beyond the asphalt courses rather than confining the damage tendency to the immediate contact zone. In contrast, the summer rutting-driving compressive proxy in panel (b) is concentrated primarily beneath the tire footprint and within the upper pavement structure. This difference is consistent with the seasonal stiffness contrast: the stiffer winter system transfers crack-driving stress more deeply, whereas the softer summer asphalt state favors localized compressive deformation along the near-surface load path.

Panel (c) further distinguishes these mechanisms through the bottom-asphalt tensile-strain corridor. The winter curve reaches a higher maximum near the loading center and remains above the summer curve over most of the longitudinal range, indicating a stronger tensile demand at the bottom of the asphalt structure. The summer response is narrower and lower in magnitude, suggesting that its dominant deterioration tendency is less associated with bottom-up tensile cracking and more closely related to compressive and shear-assisted deformation. This interpretation is supported by panel (d), where the summer-to-winter contrast is predominantly negative along the deeper central corridor but becomes locally positive within the upper transition region. The alternating distribution shows that seasonal softening does not simply amplify the same damage field; instead, it redistributes the dominant mechanism between shallow rutting-related deformation and deeper fatigue-related response.

Panels (e) and (f) provide temporal and layerwise evidence of this redistribution. The normalized cumulative damage work in panel (e) increases rapidly around the load-passage time and then approaches unity more gradually. The winter and summer curves remain close, although the summer response accumulates slightly faster during the early stage, indicating that the seasonal difference lies mainly in the spatial allocation of damage rather than in the total normalized work over one passage. The layerwise partition in panel (f) confirms this distinction. Winter damage is dominated by the road base, with secondary contributions from the asphalt base, whereas summer damage shifts strongly toward the subgrade and, to a lesser extent, the surface course. Overall, the winter state is governed by deeper fatigue-type transfer through the structural layers, while the summer state is characterized by stronger near-surface rutting susceptibility and increased participation of the lower supporting medium.

3.3. Scenario sensitivity, identifiability, domain transfer, and robustness

This subsection examines the behavior of the inverse framework under variations in loading, contact geometry, material state, and observation quality. Parameter scans quantify the effects of load scale, normal-pressure heterogeneity, moving speed, braking ratio, contact radius, and lateral slip, while the identifiability analysis evaluates parameter sensitivity, coupling, inverse conditioning, and the information content of the retained modes. Domain transfer and combined parameter cases are subsequently used to determine whether the learned operator preserves physically consistent winter and summer responses outside the central training configurations. Robustness is finally evaluated under measurement noise, outlier contamination, observation time jitter, elastic modulus and Poisson ratio perturbations, contact radius error, and individual probe removal.

Fig. 19 examines the sensitivity of the reconstructed mixed contact-traction response to load scale, normal-pressure heterogeneity, moving speed, braking, contact radius, and lateral slip. Panels (a) and (b) show that the peak von Mises stress σ_{vm}^{max} increases primarily with load scale in both winter and summer states, while increasing normal-pressure heterogeneity further strengthens the local stress concentration. The load-scale direction remains the dominant control because it directly amplifies all normal and tangential source coefficients, whereas the heterogeneity coefficient redistributes the same nominal normal load within the footprint. The summer response surface exhibits a slightly broader high-stress region at large load scale and strong heterogeneity, reflecting the greater redistribution of multiaxial stress within the softened layered structure.

Panels (c) and (d) present the blind reconstruction error over moving speed v and braking ratio ζ_b. The errors remain low throughout most of the scanned domain, generally within the displayed ranges of approximately 0.2%–1.4% for winter and 0.2%–1.6% for summer. Higher errors occur mainly for parameter combinations that are farther from the central response-library conditions, particularly when speed variation is combined with stronger longitudinal traction. The summer error surface is slightly more variable, indicating that the lower asphalt stiffness increases the sensitivity of the inverse response to changes in transient timing and braking-related shear transfer. Nevertheless, the smooth error distributions show that the reconstructed coefficients vary continuously over the investigated loading domain.

Panel (e) evaluates the winter contact-load severity index over contact radius a and normal-pressure heterogeneity. The severity increases as the pressure field becomes more nonuniform and is generally larger for smaller contact radii, where the applied load is concentrated over a narrower footprint. This index accounts for both the peak-to-mean normal-pressure ratio and the associated peak von Mises response, and therefore characterizes source concentration rather than only the nominal load magnitude. Panel (f) independently quantifies the fraction of summer transient stress work carried by the longitudinal and lateral traction components. The tangential-work fraction increases with both braking ratio and lateral-slip ratio but remains below approximately 3%, confirming that the normal source remains dominant while tangential loading provides a smaller but systematic dynamic contribution. Overall, the parameter scans demonstrate stable reconstruction trends and physically consistent sensitivity to normal-load concentration and tangential excitation.

Fig. 20 examines the practical identifiability of the mixed contact-traction inverse problem and the coupling between loading, geometric, material, and depth-related descriptors. The inverse-parameter curvature matrix $\mathbf{H}_\zeta$ in panel (a) has unit diagonal entries owing to normalization, whereas the off-diagonal structure reveals pronounced pairwise coupling. The strongest negative interaction occurs between load scale and contact radius, reflecting their competing influence on contact-pressure intensity, while normal-pressure heterogeneity is also strongly coupled with braking. The stiffness–depth interaction is positive but more moderate, indicating that changes in material stiffness can be partially compensated by shifts in the effective response depth. Thus, the inverse problem is locally structured but not uniformly separable across all descriptors.

Panel (b) shows that the normalized sensitivity gains are highly anisotropic rather than uniformly distributed. Effective depth provides the dominant sensitivity direction, with a normalized gain of unity, while contact radius forms the second most influential parameter at approximately 0.26. The gains associated with load scale, braking, stiffness, and especially normal-pressure heterogeneity are much smaller. This hierarchy indicates that the reconstructed observation field

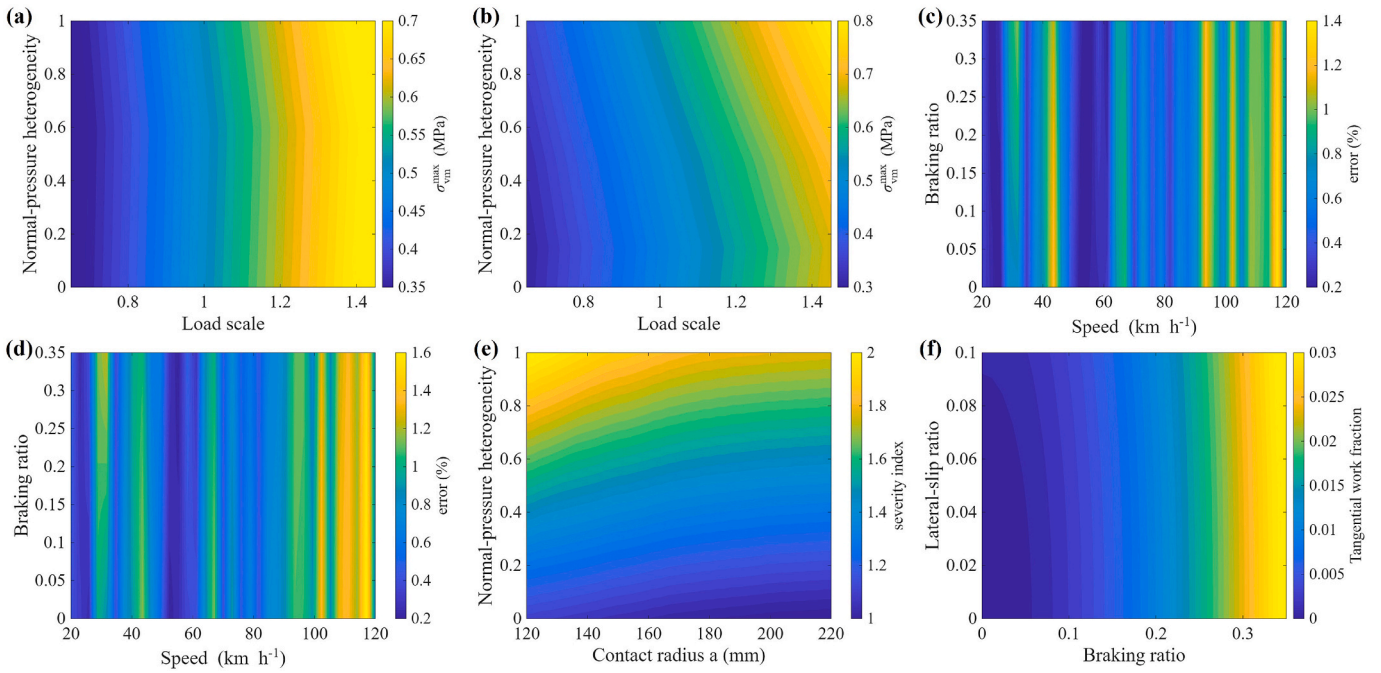


Fig. 19. Parameter scans of mixed contact-traction response and blind generalization: (a) winter peak von Mises stress σ_{vm}^{max} over load scale and normal-pressure heterogeneity, (b) summer σ_{vm}^{max} over the same parameters, (c) winter blind reconstruction error over moving speed v and braking ratio ζ_b, (d) summer blind reconstruction error over v and ζ_b, (e) winter contact-load severity index over contact radius a and normal-pressure heterogeneity, and (f) summer tangential transient-work fraction over braking ratio and lateral-slip ratio.

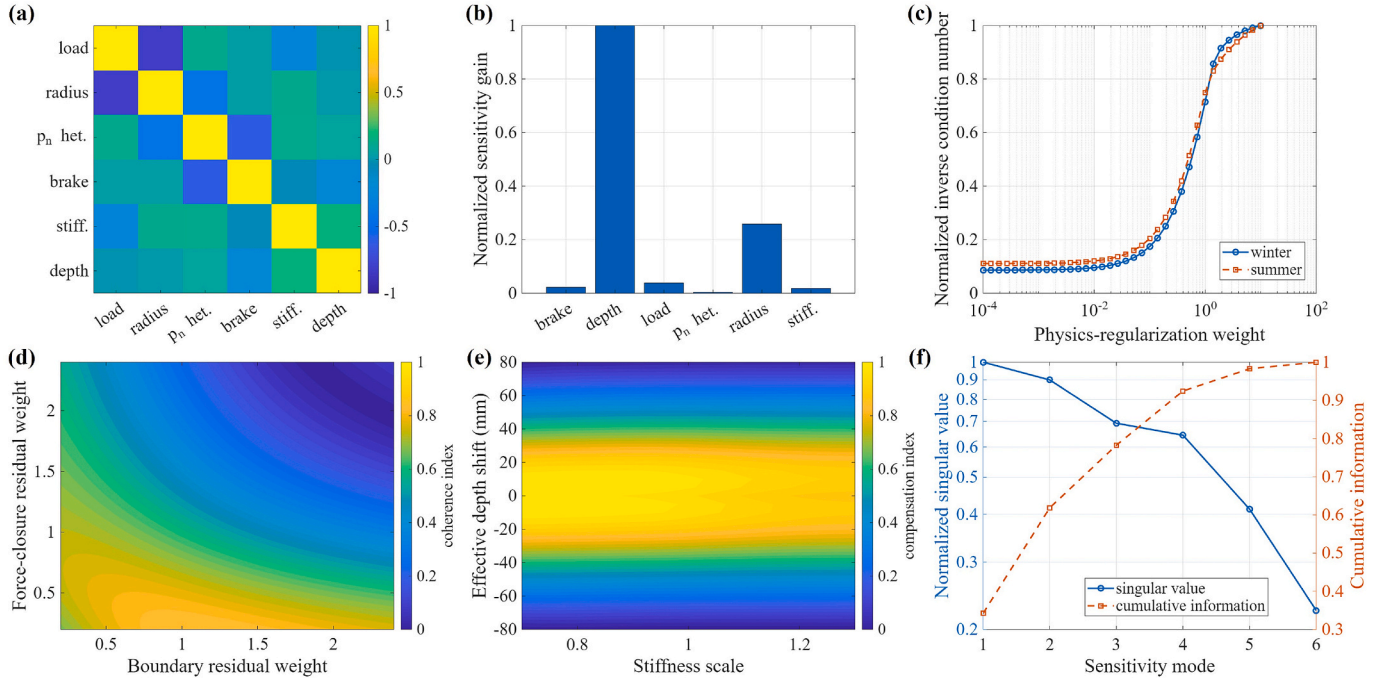


Fig. 20. Inverse identifiability and physics-constraint coupling of the mixed contact-traction reconstruction: (a) inverse-parameter curvature matrix $\mathbf{H}_\zeta$, (b) normalized sensitivity gains of braking ratio, effective depth, load scale, normal-pressure heterogeneity, contact radius, and stiffness scale, (c) regularization-dependent normalized inverse condition number, (d) boundary–force residual coherence over the boundary and force-closure weights, (e) stiffness–depth compensation landscape, and (f) normalized singular-value spectrum and cumulative inverse information.

is most responsive to changes in the depthwise transfer pattern and footprint size, whereas several source descriptors are identified mainly through weaker coupled signatures. Panel (c) further shows that the normalized inverse condition number increases continuously as the physics-regularization weight grows. The winter and summer curves remain close, but both approach unity under strong regularization. Consequently, weak-to-moderate regularization preserves better numerical conditioning, whereas excessive physics weighting progressively compresses the admissible inverse directions and increases ill-conditioning.

Panels (d)–(f) clarify how the loss weights and sensitivity modes shape the inverse solution space. The boundary–force coherence index in panel (d) is highest for relatively weak force-closure weighting combined with a moderate boundary-loss weight. Increasing both weights reduces coherence, indicating that excessive simultaneous enforcement can introduce competition between local boundary matching and global resultant closure. The compensation map in panel (e) contains a broad high-index band around zero effective-depth shift, with only a weaker dependence on stiffness scale. This shows that the principal compensation mechanism is governed by depth misregistration, while moderate stiffness variations can be accommodated without producing a distinct alternative solution branch. Finally, panel (f) shows a gradual decay of the normalized singular values, accompanied by a rapid increase in cumulative information. The first four sensitivity modes contain most of the inverse information, whereas the fifth and sixth modes mainly refine weakly observable parameter combinations. Overall, the figure demonstrates that the inverse problem is identifiable in a reduced information subspace, but its stability depends on controlling parameter coupling and avoiding excessive regularization.

Fig. 21 evaluates the transferability of the reconstruction framework across seasonal mixed contact traction domains, together with its calibration behavior and observation subspace consistency. Panel (a) shows the scenario distribution in a 2D latent space, with the points colored according to the domain score. The samples form a continuous but spatially structured manifold rather than two completely separated seasonal clusters. Cases with low and high domain scores occupy partially overlapping regions, indicating that the winter and summer responses share common load-transfer characteristics while retaining systematic differences associated with the seasonal material state and contact-source descriptors. This partially shared representation supports transfer between seasonal domains because it preserves common mechanical information without removing domain-specific variability.

The calibration results in panel (b) show that the transfer error remains bounded over the tested numbers of calibration samples but does not decrease monotonically. The winter target error is generally higher and exhibits a pronounced local maximum near the middle of the sampling range, whereas the summer target error remains lower and varies within a narrower interval. The subsequent decrease in the winter error indicates that additional samples can correct the effect of a temporarily unrepresentative calibration subset. The result also demonstrates that the mechanical coverage of the selected samples is as important as the total number of calibration samples. Panel (c) presents the latent domain-shift covariance matrix $\mathbf{C}_D$. Its diagonal dominance confirms that load scale, normal-pressure heterogeneity, speed, braking, and season retain distinct shift directions. The moderate off-diagonal terms, particularly those associated with load scale and normal-pressure heterogeneity, reflect the coupled effects of source intensity and footprint redistribution.

Panel (d) compares the standardized reconstructed coefficients with their reference values for load scale, normal-pressure heterogeneity, braking, and lateral slip. Most points remain close to the ideal parity line over the full coefficient range, demonstrating that the source descriptors remain identifiable after transfer between the seasonal domains. The largest deviations occur for several cases with high-amplitude normal-pressure heterogeneity, which is consistent with the relatively low sensitivity of this descriptor in the identifiability analysis. Panel (e) further shows that the dominant contributors to the domain shift differ between seasons. In winter, normal-pressure heterogeneity provides the largest contribution, followed by braking. In summer, the shift is governed mainly by speed and braking. The contribution of load scale remains comparatively small in both seasons, indicating that the transfer discrepancy is controlled more strongly by source redistribution and transient shear effects than by changes in the total load magnitude.

Panel (f) quantifies the affinity between the winter and summer observation subspaces as the retained dimension increases. The displacement affinity decreases rapidly from unity and reaches a

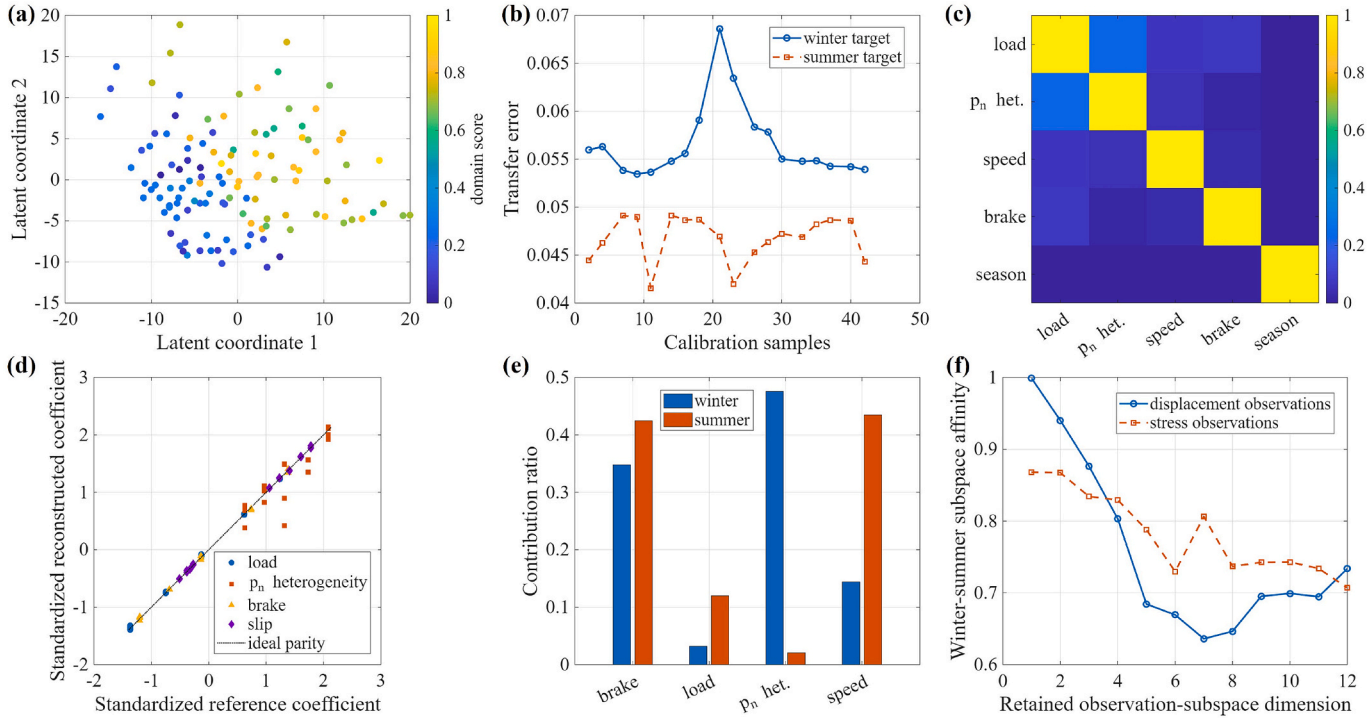


Fig. 21. Domain-transfer and calibration diagnostics of the mixed contact-traction reconstruction: (a) latent-space embedding of seasonal loading scenarios colored by domain score, (b) few-shot winter and summer transfer errors, (c) latent domain-shift covariance matrix $\mathbf{C}_D$ for load scale, normal-pressure heterogeneity, speed, braking, and season, (d) parity comparison of standardized reference and reconstructed source coefficients, (e) winter and summer contributions of braking, load scale, normal-pressure heterogeneity, and speed to the domain shift, and (f) winter–summer affinity of the displacement and stress observation subspaces as a function of retained dimension.

minimum at an intermediate dimension before partially recovering. The stress affinity is lower at the leading dimensions but remains comparatively stable as additional modes are retained. These nonmonotonic trends indicate that the leading modes contain strongly shared seasonal information, whereas several intermediate modes emphasize material-dependent response characteristics. At higher dimensions, both affinities remain close to 0.7, showing that substantial common structure is retained despite the seasonal stiffness contrast. Overall, Fig. 21 demonstrates that the proposed framework transfers effectively across seasonal loading domains, although the dominant shift factors and the benefit of additional calibration samples depend on the mechanical information represented by the selected observations.

Fig. 22 presents the von Mises stress σ_{vm} obtained under six combined contact-traction scenarios for the winter and summer material states. Across all parameter combinations, the von Mises stress intensity remains concentrated beneath the tire footprint and attenuates rapidly with increasing depth and longitudinal distance. The lower road base, sub-base, and subgrade exhibit only weak σ_{vm} activity. This result indicates that the deviatoric response is governed primarily by the local contact traction and the stiffness of the upper pavement layers. Although load scale, normal-pressure heterogeneity, moving speed, braking ratio, contact radius, and lateral slip vary simultaneously, all cases retain a stable and mechanically consistent stress transfer pattern without artificial deep-field oscillations.

The winter cases in panels (a) to (f) generally show greater near-surface stress intensity under the more severe combined loading conditions. C(1) produces the weakest and most confined response, whereas C4 and C6 generate more pronounced stress concentrations beneath the footprint. The stronger response in these cases is associated mainly with the increased load scale, greater normal-pressure heterogeneity, stronger braking, and larger lateral slip contribution. A smaller or moderate contact radius further concentrates the applied traction within the footprint. However, the variation among the cases is not controlled by a single parameter because speed, footprint size, and tangential traction jointly affect the transient stress redistribution. The common color range also shows that the response remains below approximately 0.6 MPa for all winter combinations.

The summer fields in panels (g) to (l) preserve the same near-surface localization, although the magnitude and lateral spread vary among the individual combinations. The stronger summer responses occur mainly in C4 and C6, while C1 and C2 remain relatively weak. Compared with the corresponding winter cases, seasonal softening modifies the shape and penetration of the stress zone, but the influence of the combined loading parameters remains more pronounced than the seasonal change in the overall field pattern. In particular, the higher load scale and normal-pressure heterogeneity in C6 produce the most distinct contact-induced stress concentration in both seasons. Overall, Fig. 22 demonstrates that the proposed framework consistently represents coupled loading effects across different seasonal material states while preserving the expected localization and depthwise attenuation of the deviatoric stress response.

Fig. 23 presents the vertical strain fields ε_{zz} for the same six contact-traction combinations considered in Fig. 22 under the winter and summer material states. In all cases, the response is dominated by a compressive strain region centered beneath the tire footprint and extending into the layered pavement. Compared with the von Mises stress fields, the vertical strain distributions are broader and penetrate farther into the supporting layers. This difference reflects the cumulative compliance of the layered structure, since ε_{zz} is influenced not only by the local contact intensity but also by the deformation capacity of the

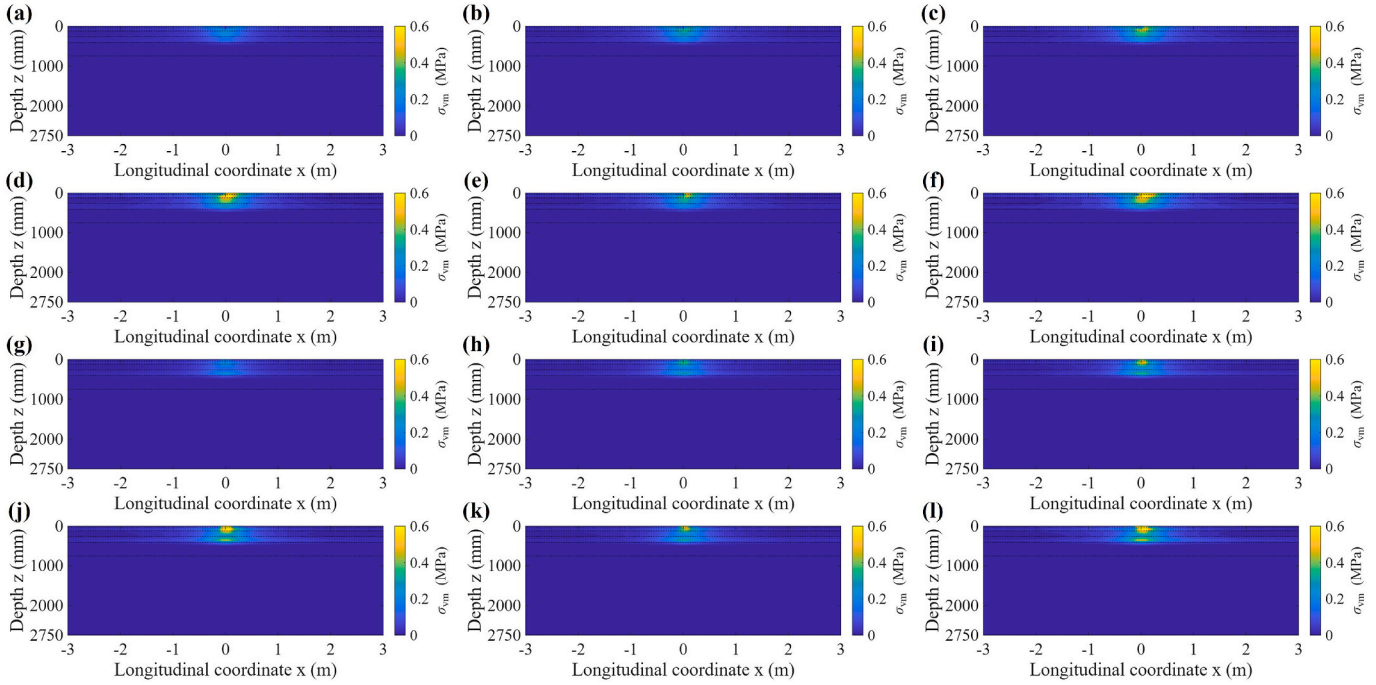


Fig. 22. Parameter-combination maps of von Mises stress σ_{vm} under season-dependent material states: (a)–(f) winter cases C1-C6, and (g)–(l) summer cases C1-C6. The parameter combinations are defined as follows: C1: load scale $= 0.75$, normal-pressure heterogeneity $\eta_p = 0.15$, speed $v = 30\text{km}\cdot\text{h}^{-1}$, braking ratio $\zeta_b = 0.00$, contact radius $a = 170\text{mm}$, and lateral slip ratio $\zeta_s = 0.00$; C2: load scale $= 0.95$, normal-pressure heterogeneity $\eta_p = 0.30$, speed $v = 55\text{km}\cdot\text{h}^{-1}$, braking ratio $\zeta_b = 0.05$, contact radius $a = 150\text{mm}$, and lateral slip ratio $\zeta_s = 0.02$; C3: load scale $= 1.15$, normal-pressure heterogeneity $\eta_p = 0.50$, speed $v = 75\text{km}\cdot\text{h}^{-1}$, braking ratio $\zeta_b = 0.10$, contact radius $a = 145\text{mm}$, and lateral slip ratio $\zeta_s = 0.03$; C4: load scale $= 1.35$, normal-pressure heterogeneity $\eta_p = 0.70$, speed $v = 95\text{km}\cdot\text{h}^{-1}$, braking ratio $\zeta_b = 0.18$, contact radius $a = 140\text{mm}$, and lateral slip ratio $\zeta_s = 0.05$; C5: load scale $= 1.05$, normal-pressure heterogeneity $\eta_p = 0.85$, speed $v = 45\text{km}\cdot\text{h}^{-1}$, braking ratio $\zeta_b = 0.26$, contact radius $a = 155\text{mm}$, and lateral slip ratio $\zeta_s = -0.03$; and C6: load scale $= 1.45$, normal-pressure heterogeneity $\eta_p = 1.00$, speed $v = 115\text{km}\cdot\text{h}^{-1}$, braking ratio $\zeta_b = 0.32$, contact radius $a = 150\text{mm}$, and lateral slip ratio $\zeta_s = 0.07$.

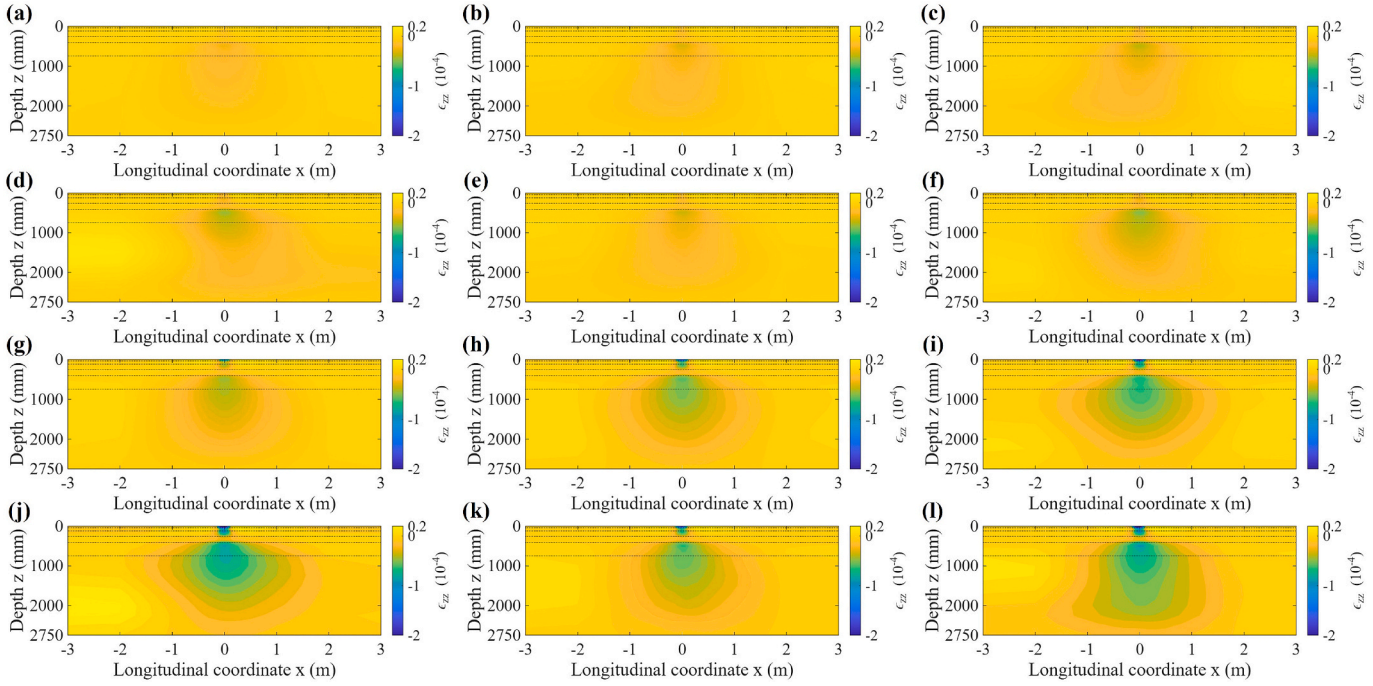


Fig. 23. Parameter-combination maps of vertical strain ϵ_{zz} under winter and summer material states: (a) to (f) winter cases C1 to C6, and (g) to (l) summer cases C1 to C6. The load scale, normal-pressure heterogeneity, speed, braking ratio, contact radius, and lateral slip ratio for C1 to C6 are identical to those defined in Fig. 22.

asphalt courses, road base, sub-base, and subgrade.

The winter fields in panels (a) to (f) remain relatively weak under the common color scale. The compressive strain is concentrated mainly beneath the loading center, while the deeper response varies only moderately among the six combinations. Increasing load scale, normal-pressure heterogeneity, braking ratio, and lateral slip generally enlarges the central compressive zone, although the response does not vary monotonically because speed and contact radius change simultaneously. The stronger combinations produce a somewhat deeper strain basin, but the high winter stiffness continues to restrain the deformation and limits the contrast among the individual scenarios.

The summer cases in panels (g) to (l) show substantially stronger and

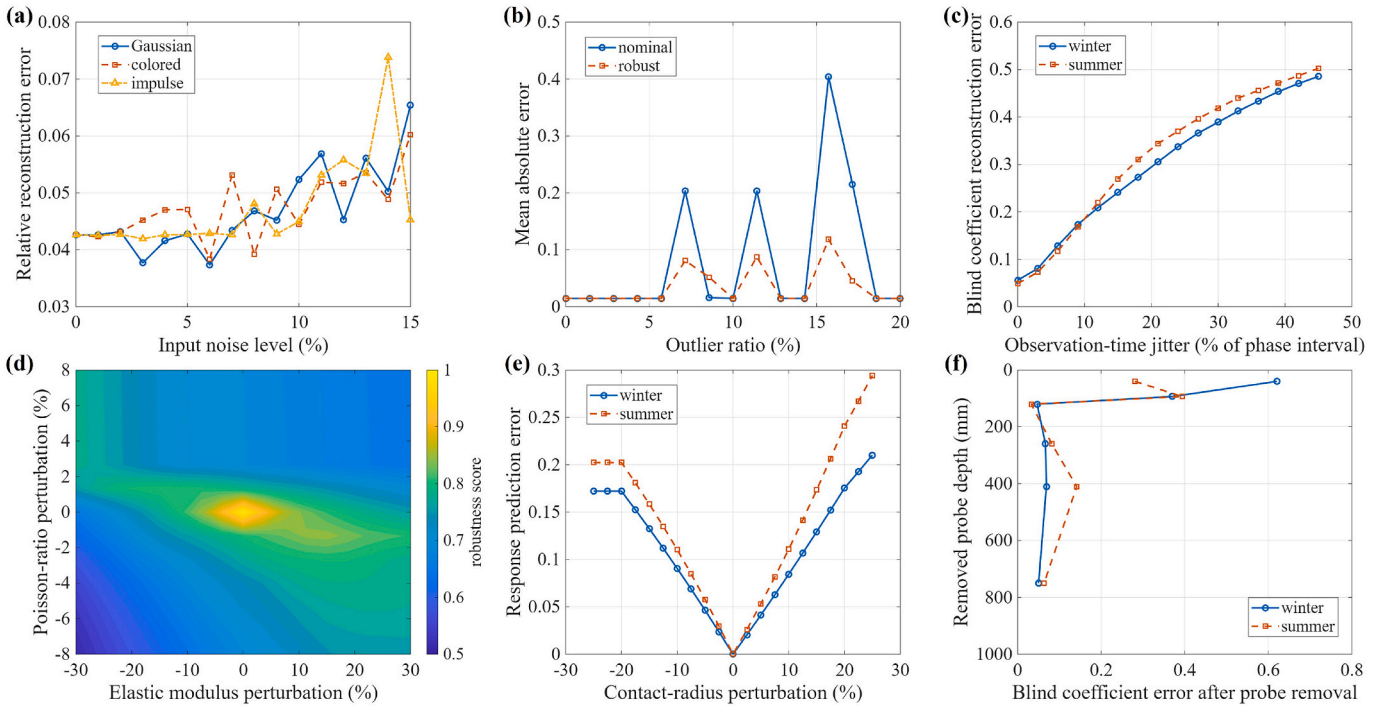


Fig. 24. Robustness diagnostics of the inverse reconstruction under observation and model uncertainty: (a) relative reconstruction error under Gaussian, colored, and impulse noise, (b) outlier sensitivity under nominal and robust residual treatments, (c) blind coefficient reconstruction error under observation time jitter, (d) robustness surface under elastic modulus and Poisson ratio perturbations, (e) response prediction error under contact radius perturbation, and (f) blind coefficient error after individual probe removal at different observation depths.

more extensive compressive strain fields. The central strain bulb expands laterally and vertically as the combined loading severity increases, and the higher-intensity cases approach the lower end of the displayed range. The largest differences are associated with the combined effects of higher load scale, stronger normal-pressure heterogeneity, greater tangential traction, and a more concentrated contact footprint. Compared with the corresponding winter cases, the summer strain penetrates farther into the road base and lower supporting layers, confirming that reduced asphalt stiffness increases the depthwise participation of the pavement system. Thus, while the von Mises response in Fig. 22 remains strongly localized near the surface, Fig. 23 demonstrates that ε_{zz} is more sensitive to seasonal stiffness and provides a clearer measure of deformation transfer under combined mixed contact-traction loading.

Fig. 24 evaluates the robustness of the inverse reconstruction under observation noise, outlier contamination, timing uncertainty, material perturbation, contact radius variation, and sparse probe removal. Panel (a) shows that the relative reconstruction errors remain close to the baseline level under weak noise and generally increase as the input noise approaches 15%. The three noise types produce comparable errors over much of the investigated range, although impulse perturbations cause the largest isolated deviation, reaching approximately 0.074 near the upper noise levels. Gaussian and colored noise lead to more moderate error growth. The nonmonotonic fluctuations indicate that reconstruction sensitivity depends not only on noise amplitude but also on how the perturbation projects onto the mechanically informative observation components.

Panel (b) compares nominal and robust treatments under increasing outlier ratios. The nominal error develops several pronounced peaks when corrupted observations coincide with influential response coordinates, with the largest value exceeding 0.4. Robust residual weighting substantially reduces these peaks and limits the corresponding error to approximately 0.12. The response is not monotonic because the effect of a given outlier ratio depends on the locations of the contaminated observations. Nevertheless, the robust formulation consistently suppresses the influence of localized corruption while retaining the physical constraints used in the inverse reconstruction. Panel (c) shows that observation time misregistration produces a progressive increase in blind coefficient error for both seasonal states. The winter and summer curves remain close at small timing shifts, while the summer error becomes slightly larger at moderate and high jitter levels. This confirms that accurate synchronization between the moving load and the sparse response measurements is important for preserving the transient source signature.

Panel (d) examines the combined influence of elastic modulus and Poisson ratio perturbations. The robustness score is highest near the reference material state and decreases as the assumed parameters move away from the calibrated combination. The surface is mildly asymmetric, indicating that positive and negative changes in stiffness and compressibility do not produce equivalent response distortions. Panel (e) shows a clear minimum in response prediction error at zero contact radius perturbation. Underestimation and overestimation of the radius both increase the error, with the summer case exhibiting consistently greater sensitivity because its softer asphalt layers produce stronger deformation changes when the footprint size is modified.

Panel (f) evaluates the information contribution of individual probes by removing them one at a time. Probe removal at shallow depths produces the largest winter error, while the summer response is particularly sensitive to selected upper and intermediate probes. Removing the deepest probe results in comparatively small errors for both seasons, indicating that the near-surface and intermediate observations contain more direct information about the contact source. The distinct seasonal profiles also show that the optimal sensor arrangement depends on the stiffness state of the layered pavement. Overall, Fig. 24 demonstrates that the proposed framework remains stable under moderate uncertainty, while timing registration, influential outliers, contact radius, and shallow probe availability constitute the principal sources of reconstruction degradation.

4. Conclusions

This study developed a physics-informed neural network (PINN) framework for inverse mixed tire-contact traction reconstruction and dynamic finite-layer pavement response. The tire footprint was represented by a mechanically identifiable total normal pressure together with longitudinal and lateral traction components. A 3D transient FE model was used to generate displacement, stress, strain, reactions, and strain-energy histories under a moving load with inertia and damping. These mechanics were incorporated into the inverse model through data, dynamic-equilibrium, constitutive, boundary, interface, force-closure, and regularization constraints. The training, validation, and blind reconstruction loads were generated from mutually disjoint source combinations, so the held-out contact fields were inferred from sparse response histories without exposing their prescribed source coefficients during training or model selection.

The results showed that the proposed framework reproduced the principal FE stress, strain, and displacement fields with small and spatially localized errors. The reconstructed total normal pressure and tangential tractions retained their footprint-level distribution, resultant characteristics, and higher-order spatial descriptors. Additional blind-load tests confirmed that previously unseen contact sources could be reconstructed while preserving the location, spread, and depthwise attenuation of the internal response. The physics-agreement index remained close to unity over most of the pavement domain, even though the observations represented only a small fraction of the total mechanical degrees of freedom. Comparison with the independent experimental and numerical data published in Elseifi et al. (2006) also produced close agreement in displacement and stress, with coefficients of determination near unity and relative errors of only a few percent.

The seasonal analyses showed that matched winter and summer loads produced similar primary stress-transfer paths but different deformation and damage mechanisms. The stiffer winter state exhibited more confined deformation and stronger fatigue-related stress transfer, whereas the softer summer state produced greater depthwise penetration of vertical strain, broader shear redistribution, greater rutting susceptibility, and increased participation of the supporting layers. Parameter scans, identifiability analysis, and domain-transfer diagnostics demonstrated that load scale, contact radius, normal-pressure heterogeneity, speed, braking, lateral slip, material state, and effective response depth influence the inverse solution through distinct but coupled mechanisms. The framework remained stable under moderate observation noise and material uncertainty, while influential outliers, timing misregistration, contact radius error, and removal of shallow or intermediate probes produced the clearest degradation. These findings establish a mechanics-consistent basis for reconstructing mixed tire-contact tractions and depth-resolved transient pavement responses from sparse observations under previously unseen loading conditions.

Although the present framework adopts a linear-elastic constitutive model to establish and validate the proposed inverse reconstruction methodology, the underlying PINN formulation is not restricted to linear elasticity. Future work will extend the constitutive description to incorporate temperature-dependent viscoelastic behavior and time-dependent material evolution, thereby enabling more realistic prediction of asphalt pavement responses under sustained and cyclic loading. Such an extension will also provide a more rigorous basis for evaluating irreversible energy dissipation and long-term pavement deterioration.

CRediT authorship contribution statement

Dong Feng: Writing – review & editing, Writing – original draft, Visualization, Validation, Software, Resources, Project administration, Methodology, Investigation, Funding acquisition, Formal analysis, Data

curation, Conceptualization.

Declaration of competing interest

The author declares that he has no known competing financial interests or personal relationships that could have appeared to influence the work reported in this paper.

Acknowledgments

This research is supported by the China Scholarship Council (CSC., No. 202308080042). In addition, the author would like to thank two anonymous reviewers for their review of this article; their expert advice greatly improved the quality of this work.

Appendix A. Tire-contact traction reconstruction and footprint descriptors

This appendix defines the quantities used to describe and evaluate the reconstructed tire-contact traction. The mechanically observable source consists of the total normal contact pressure and the longitudinal and lateral traction components. The descriptors evaluate traction magnitude, resultant closure, pressure-centroid position, local moment structure, and source-resolution stability.

Let $\chi_c(\mathbf{s},t)$ denote the footprint indicator function, where $\mathbf{s}=(x,y)^{\mathrm{T}}$ is the local pavement-surface coordinate. The spatially heterogeneous total normal contact pressure is represented as:

$$p_n(\mathbf{s},t)=\chi_c(\mathbf{s},t)A_n(t)g_n(\mathbf{s},t), \tag{A1}$$

where $A_n(t)$ is a time-dependent pressure-normalization factor and $g_n(\mathbf{s},t)$ is a non-negative function describing the spatial modulation of the total normal pressure within the footprint.

To ensure that the distributed normal pressure satisfies the prescribed vertical-load resultant $P(t)$, the normalization factor in Eq. A (1) is calculated from:

$$A_n(t)=\frac{P(t)}{\int_{\Gamma_c}\chi_c(\mathbf{s},t)g_n(\mathbf{s},t)\mathrm{d}\Gamma+\varepsilon_n}, \tag{A2}$$

where ε_n is a small positive stabilizer introduced to avoid division by zero. This normalization preserves the spatial heterogeneity represented by g_n while enforcing the required total normal load.

The longitudinal and lateral traction components are related to the reconstructed total normal pressure through spatially varying effective traction ratios. They are expressed as:

$$\begin{aligned} q_x(\mathbf{s},t)&=\mu_x(\mathbf{s},t)p_n(\mathbf{s},t),\\ q_y(\mathbf{s},t)&=\mu_y(\mathbf{s},t)p_n(\mathbf{s},t), \end{aligned} \tag{A3}$$

where $\mu_x(\mathbf{s},t)$ and $\mu_y(\mathbf{s},t)$ are the effective longitudinal and lateral traction ratios, respectively. These ratios are allowed to vary over the footprint and are reconstructed together with p_n.

To characterize the spatial position of the normal-load resultant, the pressure centroid is defined by the first moment of p_n over the contact region:

$$\mathbf{c}_p(t)=\frac{\int_{\Gamma_c}\mathbf{s}p_n(\mathbf{s},t)\mathrm{d}\Gamma}{\int_{\Gamma_c}p_n(\mathbf{s},t)\mathrm{d}\Gamma+\varepsilon_p}. \tag{A4}$$

The vector $\mathbf{c}_p(t)$ therefore measures the instantaneous displacement of the pressure center relative to the selected footprint coordinate origin.

The local rotational contribution associated with the two tangential traction components is described by the out-of-plane moment density. At each footprint position, this quantity is calculated as:

$$m_z(x,y,t)=xq_y(x,y,t)-yq_x(x,y,t). \tag{A5}$$

This descriptor retains information about the spatial organization of q_x and q_y that cannot be represented solely by their global force resultants.

For a reconstructed contact quantity $\widehat{\phi}$ and its withheld reference value ϕ, the signed normalized contact-source error is defined as:

$$\begin{aligned} E^c_\phi(\mathbf{s},t)&=\frac{\widehat{\phi}(\mathbf{s},t)-\phi(\mathbf{s},t)}{\max\limits_{\Gamma_c\times[0,T]}|\phi|+\varepsilon_\phi},\\ \phi&\in\left\{p_n,q_x,q_y,m_z\right\}. \end{aligned} \tag{A6}$$

The normalization allows errors in source components with different physical magnitudes to be compared on a consistent dimensionless scale.

The ability of the reconstructed normal pressure to reproduce the prescribed vertical resultant is evaluated through the normal source-closure error:

$$\eta^c_P(t)=\frac{\left|\int_{\Gamma_c}\widehat{p}_n(\mathbf{s},t)\mathrm{d}\Gamma-P(t)\right|}{|P(t)|+\varepsilon_P}. \tag{A7}$$

A small value of $\eta^c_P(t)$ indicates that the reconstructed pressure distribution satisfies the global normal-force requirement.

The corresponding closure of the longitudinal and lateral force resultants is evaluated jointly through the tangential source-closure error:

$$\eta_Q^c(t) = \frac{\sqrt{\left(\int_{\Gamma_c} \widehat{q}_x(\mathbf{s},t)\mathrm{d}\Gamma - Q_x(t)\right)^2 + \left(\int_{\Gamma_c} \widehat{q}_y(\mathbf{s},t)\mathrm{d}\Gamma - Q_y(t)\right)^2}}{\sqrt{Q_x^2(t) + Q_y^2(t)} + \varepsilon_Q}. \tag{A8}$$

This combined measure avoids assessing the two tangential directions independently and provides a single indicator of tangential resultant consistency.

In addition to resultant-force closure, the accuracy of the reconstructed pressure location is quantified through the normalized contact-centroid error:

$$\eta_c(t) = \frac{\|\widehat{\mathbf{c}}_p(t) - \mathbf{c}_p(t)\|_2}{\|\mathbf{c}_p(t)\|_2 + \varepsilon_c}, \tag{A9}$$

where $\widehat{\mathbf{c}}_p(t)$ and $\mathbf{c}_p(t)$ are the reconstructed and reference pressure centroids, respectively.

The reconstruction error associated with the spatial moment-density field is evaluated using:

$$E_m^c(x,y,t) = \frac{\widehat{m}_z(x,y,t) - m_z(x,y,t)}{\max\limits_{\Gamma_c\times[0,T]} |m_z| + \varepsilon_m}. \tag{A10}$$

This measure indicates whether the reconstructed tangential traction field preserves the local rotational pattern of the reference contact source.

To evaluate the influence of boundary-source resolution, let n_b denote the number of basis functions used to represent the contact-traction field. For a prescribed basis order n_b, the normal resultant-closure indicator is defined as:

$$\eta_N(n_b) = \frac{\left|\int_{\Gamma_c} \widehat{p}_{n,n_b}\mathrm{d}\Gamma - P\right|}{|P| + \varepsilon_P}. \tag{A11}$$

The variation of $\eta_N(n_b)$ with n_b shows whether refinement of the source representation improves normal-load consistency.

For the same source-basis order, the tangential resultant-closure indicator is calculated from:

$$\eta_T(n_b) = \frac{\sqrt{\left(\int_{\Gamma_c} \widehat{q}_{x,n_b}\mathrm{d}\Gamma - Q_x\right)^2 + \left(\int_{\Gamma_c} \widehat{q}_{y,n_b}\mathrm{d}\Gamma - Q_y\right)^2}}{\sqrt{Q_x^2 + Q_y^2} + \varepsilon_Q}. \tag{A12}$$

This quantity determines whether the selected source basis provides sufficient resolution to recover both tangential force resultants.

Finally, the possibility that source refinement introduces excessive spatial oscillation near the footprint boundary is assessed through the edge-oscillation measure:

$$\eta_E(n_b) = \frac{\int_{\partial\Gamma_c} \|\nabla_s \widehat{\mathbf{t}}_{c,n_b}\|_2 \mathrm{d}s}{\int_{\Gamma_c} \|\widehat{\mathbf{t}}_{c,n_b}\|_2 \mathrm{d}\Gamma + \varepsilon_E}, \tag{A13}$$

where ∇_s denotes the surface-gradient operator and $\widehat{\mathbf{t}}_{c,n_b}$ is the reconstructed contact-traction vector obtained using n_b basis functions. Together, Eqs. A (11)–(13) describe the convergence and stability of the reconstructed source as its spatial resolution is increased.

Appendix B. Three-dimensional mechanical descriptors, layer integrals, transient moving-load transfer, and damage proxies

This appendix defines the three-dimensional and time-dependent mechanical descriptors used to summarize stress intensity, layer contribution, depth transfer, transient moving-load response, and damage-oriented pavement response. All quantities are evaluated directly from the reconstructed or FE-computed displacement, stress, strain, and strain-energy histories.

Using the compressive-positive normal-stress convention adopted in the main text, the mean compressive stress is calculated as:

$$p_m = \frac{\sigma_{xx}^c + \sigma_{yy}^c + \sigma_{zz}^c}{3}. \tag{B1}$$

This quantity represents the spherical compressive contribution of the three-dimensional stress state.

The normal components of the deviatoric stress tensor are obtained by subtracting the mean compressive stress from the corresponding compressive-positive normal stresses:

$$\begin{aligned} s_{xx} &= \sigma_{xx}^c - p_m, \\ s_{yy} &= \sigma_{yy}^c - p_m, . \\ s_{zz} &= \sigma_{zz}^c - p_m \end{aligned} \tag{B2}$$

These components isolate the distortion-related part of the normal stress state from its mean compressive contribution.

Combining the deviatoric normal stresses with all three shear-stress components gives the second invariant of the deviatoric stress tensor:

$$J_2 = \frac{1}{2}\left(s_{xx}^2 + s_{yy}^2 + s_{zz}^2 + 2\tau_{xy}^2 + 2\tau_{xz}^2 + 2\tau_{yz}^2\right). \tag{B3}$$

The invariant J_2 provides a coordinate-independent measure of the local deviatoric stress intensity.

The corresponding three-dimensional von Mises stress is evaluated from the differences between the normal stresses and the three shear components as:

$$\sigma_{\mathrm{vm}} = \sqrt{\frac{1}{2}\left(\sigma_{xx}^{c} - \sigma_{yy}^{c}\right)^{2} + \frac{1}{2}\left(\sigma_{yy}^{c} - \sigma_{zz}^{c}\right)^{2} + \frac{1}{2}\left(\sigma_{zz}^{c} - \sigma_{xx}^{c}\right)^{2} + 3\left(\tau_{xy}^{2} + \tau_{xz}^{2} + \tau_{yz}^{2}\right)}. \tag{B4}$$

This scalar measure is used to characterize the intensity of the multiaxial stress state throughout the layered pavement.

The elastic energy stored locally by the stress and strain fields is represented by the strain-energy density:

$$\psi = \frac{1}{2}\boldsymbol{\varepsilon} : \boldsymbol{\sigma}. \tag{B5}$$

For explicit computation in the three-dimensional Cartesian coordinate system, the strain-energy density is expanded as:

$$\psi = \frac{1}{2}\left(\varepsilon_{xx}\sigma_{xx} + \varepsilon_{yy}\sigma_{yy} + \varepsilon_{zz}\sigma_{zz} + \gamma_{xy}\tau_{xy} + \gamma_{xz}\tau_{xz} + \gamma_{yz}\tau_{yz}\right), \tag{B6}$$

where γ_{xy}, γ_{xz}, and γ_{yz} are the engineering shear strains corresponding to the three shear-stress components.

For a scalar mechanical field $F(\mathbf{x}, t)$, its instantaneous integral over the complete three-dimensional pavement domain is defined as:

$$I_F(t) = \int_{\Omega} F(\mathbf{x}, t)\mathrm{d}\Omega. \tag{B7}$$

Depending on the selected field, $I_F(t)$ may represent the spatially accumulated stress intensity, strain activity, strain energy, or damage-oriented response.

To distinguish the contribution of an individual pavement layer, the same scalar field is integrated only over the corresponding subdomain Ω_{ℓ}:

$$I_{\ell}^{F}(t) = \int_{\Omega_{\ell}} F(\mathbf{x}, t)\mathrm{d}\Omega. \tag{B8}$$

This layer-restricted integral preserves the three-dimensional spatial distribution while isolating the contribution associated with layer ℓ.

The relative contribution of layer ℓ to the total integral of field F is then evaluated through:

$$\Pi_{\ell}^{F}(t) = \frac{I_{\ell}^{F}(t)}{I_F(t) + \varepsilon_I}. \tag{B9}$$

This expression is used for layerwise von Mises stress, vertical-strain activity, strain-energy storage, and damage-proxy contributions.

To determine the representative depth at which a non-negative mechanical response is concentrated, let $F^{+} = \max(F, 0)$. The depth centroid of this positive field is calculated as:

$$z_c^{F}(t) = \frac{\int_{\Omega} z F^{+}(\mathbf{x}, t)\mathrm{d}\Omega}{\int_{\Omega} F^{+}(\mathbf{x}, t)\mathrm{d}\Omega + \varepsilon_F}. \tag{B10}$$

A larger value of z_c^{F} indicates that the selected mechanical response penetrates more deeply into the pavement structure.

The horizontal spread of a positive field within layer ℓ is characterized by its second moment about the corresponding planar centroid. This layerwise spread is defined as:

$$\rho_{\ell}^{F}(t) = \sqrt{\frac{\int_{\Omega_{\ell}} \left[(x - x_c)^2 + (y - y_c)^2\right] F^{+}\mathrm{d}\Omega}{\int_{\Omega_{\ell}} F^{+}\mathrm{d}\Omega + \varepsilon_F}}, \tag{B11}$$

where (x_c, y_c) denotes the planar centroid of the positive response within layer ℓ. The descriptor ρ_{ℓ}^{F} therefore measures the effective lateral extent of the mechanically active region.

The relative storage of vertical compressive response within an individual pavement layer is quantified by comparing its positive vertical compressive stress with the combined stress-intensity and mean-compression measures. The corresponding ratio is:

$$\Lambda_{\ell}(t) = \frac{\mathscr{I}_{\ell}\left[\max\left(\sigma_{zz}^{c}, 0\right)\right]}{\mathscr{I}_{\ell}\left[\sigma_{\mathrm{vm}} + p_m\right] + \varepsilon_{\Lambda}}. \tag{B12}$$

This quantity provides a normalized measure of the extent to which the layer response is dominated by vertical compression.

For depth-dependent interpretation, a scalar field is averaged over the horizontal cross-section $A(z)$ at depth z. The depth-averaged response is defined as:

$$\overline{F}(z, t) = \frac{\int_{A(z)} F(x, y, z, t)\mathrm{d}A}{\int_{A(z)} \mathrm{d}A + \varepsilon_A}. \tag{B13}$$

The resulting function $\overline{F}(z, t)$ retains the depth and time dependence of the three-dimensional response while removing local in-plane variations.

For transient moving-load diagnostics, the response pulse at a selected depth is extracted directly from the cross-sectionally averaged dynamic solution. It is denoted by:

$$\Phi_z(t) = \Phi(z, t). \tag{B14}$$

The quantity Φ may represent a stress, strain, displacement, energy, or another mechanically relevant field. Unlike a translated static response, $\Phi_z(t)$ is obtained from the transient governing equations under the moving boundary traction.

The temporal duration of the response pulse is characterized by its half-maximum width. Let $t_1(z)$ and $t_2(z)$ denote the two times at which the pulse reaches one-half of its maximum value. The pulse width is then defined as:

$$T_{1/2}(z) = t_2(z) - t_1(z),$$
$$\Phi_z(t_1) = \Phi_z(t_2) = \frac{1}{2}\max_t \Phi_z(t) \tag{B15}$$

This measure describes the temporal broadening of the moving-load response as it propagates through the layered pavement.

The characteristic arrival time of the pulse energy is evaluated through its temporal centroid. The pulse-energy centroid delay is calculated as:

$$t_E(z) = \frac{\int t\Phi_z^2(t)\mathrm{d}t}{\int \Phi_z^2(t)\mathrm{d}t + \varepsilon_t}. \tag{B16}$$

Differences in $t_E(z)$ between depths or material states indicate changes in the transient transfer and delay of the moving-load response.

For modal transfer analysis, let $M_j(z)$ denote a non-negative depth profile derived from the transient response associated with source mode j. The considered modes may include the normal-pressure mode, longitudinal-shear mode, lateral-shear mode, or a combined mode. The relative work contribution of mode j is defined as:

$$\Omega_j = \frac{\int_0^H M_j(z)\mathrm{d}z}{\sum_m \int_0^H M_m(z)\mathrm{d}z + \varepsilon_M}. \tag{B17}$$

The modal work partitions provide a normalized comparison of the mechanically accumulated contributions produced by the different contact-traction modes.

To quantify whether a modal response is localized at a small number of depths or broadly distributed throughout the pavement, the normalized modal depth-shape entropy is introduced as:

$$H_j^M = -\frac{1}{\log N_z}\sum_{k=1}^{N_z} \pi_{jk}\log\left(\pi_{jk} + \varepsilon_M\right)$$
$$\pi_{jk} = \frac{M_j(z_k)}{\sum_{n=1}^{N_z} M_j(z_n) + \varepsilon_M}, \tag{B18}$$

A larger H_j^M indicates a more broadly distributed modal response, whereas a smaller value indicates stronger localization over depth.

The proportion of a mode-averaged response retained at a particular layer interface is evaluated using the interface-transfer ratio. For an interface located at depth z_I, this ratio is:

$$T_I(z_I) = \frac{\overline{M}(z_I)}{\max_{z\in[0,H]} \overline{M}(z) + \varepsilon_T}, \tag{B19}$$

where $\overline{M}(z)$ is the mode-averaged depth-transfer response. The decrease of T_I across successive interfaces describes attenuation of the contact-induced response with depth.

A fatigue-oriented mechanical proxy is constructed by combining the maximum horizontal tensile strain with the local von Mises stress. It is defined as:

$$D_f(\mathbf{x}, t) = \max\left(\varepsilon_{xx}, \varepsilon_{yy}, 0\right)\sigma_{\mathrm{vm}}. \tag{B20}$$

This descriptor identifies regions where horizontal tensile deformation and multiaxial stress intensity coexist, without introducing an additional fatigue constitutive law.

A rutting-oriented compressive proxy is obtained by combining the positive vertical compressive strain with the mean compressive stress. The corresponding quantity is:

$$D_r(\mathbf{x}, t) = \max(-\varepsilon_{zz}, 0)p_m. \tag{B21}$$

The proxy D_r highlights locations where substantial vertical compressive deformation occurs under a pronounced compressive stress state.

To distinguish regions dominated by rutting-oriented compression from those dominated by fatigue-oriented tensile response, a normalized mechanism-contrast field is defined as:

$$D_c(\mathbf{x}, t) = \frac{D_r(\mathbf{x}, t)}{\max_{\mathbf{x}\in\Omega} D_r(\mathbf{x}, t) + \varepsilon_D} - \frac{D_f(\mathbf{x}, t)}{\max_{\mathbf{x}\in\Omega} D_f(\mathbf{x}, t) + \varepsilon_D}. \tag{B22}$$

Positive values of D_c indicate a stronger rutting-oriented contribution, whereas negative values indicate a stronger fatigue-oriented contribution.

Finally, the tensile-strain corridor at the bottom of the asphalt region is extracted from the larger of the two horizontal normal-strain components. At the asphalt-bottom depth z_{bot}, it is evaluated as:

$$\varepsilon_{\mathrm{bot}}(x, y, t) = \max\left[\varepsilon_{xx}(x, y, z_{\mathrm{bot}}, t), \varepsilon_{yy}(x, y, z_{\mathrm{bot}}, t)\right]. \tag{B23}$$

This field identifies the spatial and temporal distribution of the governing horizontal tensile strain at the bottom of the asphalt structure.

Appendix C. Training, identifiability, parameter scanning, transfer learning, and robustness indicators

This appendix defines the training and inverse diagnostic quantities used to evaluate convergence, identifiability, parameter sensitivity, domain transfer, and robustness.

For the loss components $\mathscr{L}_j$, the normalized loss share is:

$$\pi_j = \frac{\mathscr{L}_j}{\sum_{m=1}^{M} \mathscr{L}_m + \varepsilon_L}. \tag{C1}$$

The loss-allocation entropy is:

$$\mathscr{H}_L = -\frac{1}{\log M}\sum_{j=1}^{M}\pi_j \log\left(\pi_j+\varepsilon_L\right). \tag{C2}$$

The constraint-dominance indicator is:

$$\mathscr{D}_C = \sum_{j\in\mathscr{J}_C}\pi_j, \tag{C3}$$

where $\mathscr{J}_C$ is the set of physics-related loss components. The force-share indicator is:

$$\chi_F = \frac{\mathscr{L}_F}{\sum_{m=1}^{M}\mathscr{L}_m+\varepsilon_L}. \tag{C4}$$

The optimizer update norm $\Delta_\theta^{(k)}$ and loss-weight drift $\Delta_w^{(k)}$ are:

$$\Delta_\theta^{(k)} = \|\boldsymbol{\theta}^{(k+1)}-\boldsymbol{\theta}^{(k)}\|_2, \tag{C5}$$

$$\Delta_w^{(k)} = \|\mathbf{w}^{(k+1)}-\mathbf{w}^{(k)}\|_2, \tag{C6}$$

where $\mathbf{w}$ collects the adaptive loss weights. The loss-weight-update acceptance ratio is:

$$A_r^{(k)} = \frac{N_{\mathrm{acc}}^{(k)}}{N_{\mathrm{res}}^{(k)}+\varepsilon_A}, \tag{C7}$$

where $N_{\mathrm{acc}}^{(k)}$ is the number of accepted loss-balance updates and $N_{\mathrm{res}}^{(k)}$ is the total number of tested loss-balance updates.

For field reconstruction, the normalized error is:

$$e_\phi = \frac{\|\widehat{\phi}-\phi\|_2}{\|\phi\|_2+\varepsilon_\phi}. \tag{C8}$$

The signed normalized spatial error is:

$$E_\phi(\mathbf{x}) = \frac{\widehat{\phi}(\mathbf{x})-\phi(\mathbf{x})}{\max_\Omega|\phi|+\varepsilon_\phi}. \tag{C9}$$

For inverse identifiability, let $\boldsymbol{\zeta}$ be a vector of inverse parameters and let $\mathbf{J}_\zeta$ be the sensitivity matrix of selected observations with respect to $\boldsymbol{\zeta}$. The regularized curvature matrix is:

$$\mathbf{H}_\zeta = \mathbf{J}_\zeta^{\mathrm{T}}\mathbf{J}_\zeta+\lambda_R\mathbf{I}, \tag{C10}$$

where λ_R is a regularization weight and $\mathbf{I}$ is the identity matrix. The normalized identifiability score is:

$$\kappa_\zeta = \frac{\lambda_{\min}(\mathbf{H}_\zeta)}{\lambda_{\min}(\mathbf{H}_\zeta)+\varepsilon_\kappa}. \tag{C11}$$

The parameter sensitivity gain for parameter ζ_j is:

$$G_j = \frac{(\mathbf{H}_\zeta)_{jj}}{\max_m(\mathbf{H}_\zeta)_{mm}+\varepsilon_G}. \tag{C12}$$

The residual-angle coherence between boundary and force residuals is:

$$C_{bf} = \frac{\mathbf{r}_b\cdot\mathbf{r}_F}{\|\mathbf{r}_b\|_2\|\mathbf{r}_F\|_2+\varepsilon_C}, \tag{C13}$$

where $\mathbf{r}_b$ and $\mathbf{r}_F$ are boundary and force-residual vectors.

To investigate possible compensation between the elastic-modulus scale and the assumed depth location of the observation or response feature, the inverse problem is independently evaluated over the corresponding two-parameter grid. Let $J_{\mathrm{inv}}(\zeta_E,\zeta_z)$ denote the converged inverse objective obtained for the stiffness-scale parameter ζ_E and depth-shift parameter ζ_z. A normalized stiffness-depth compatibility score is then defined as:

$$C_{sd}(\zeta_E,\zeta_z) = 1-\frac{J_{\mathrm{inv}}(\zeta_E,\zeta_z)-J_{\min}}{J_{\max}-J_{\min}+\varepsilon_{sd}}, \tag{C14}$$

where $J_{\min}$ and $J_{\max}$ are the minimum and maximum values of J_{inv} over the evaluated parameter grid, respectively, and ε_{sd} is a small positive stabilizer. A value of C_{sd} close to unity indicates that the corresponding stiffness-depth combination produces a comparatively low inverse objective.

The normalized weak-sensitivity indicator for observation or residual component i and parameter j is:

$$N_{ij} = 1-\frac{\left|(\mathbf{J}_\zeta)_{ij}\right|}{\max_{i,j}\left|(\mathbf{J}_\zeta)_{ij}\right|+\varepsilon_N}. \tag{C15}$$

For parameter scanning, a generic response surface is:

$$\mathscr{S}_{ab} = \mathscr{S}(\zeta_a, \zeta_b), \tag{C16}$$

where ζ_a and ζ_b may represent load scaling, normal-pressure heterogeneity or pressure-concentration index, speed, braking ratio, contact radius, stiffness scale, or depth shift.

To summarize the combined severity of the reconstructed normal and tangential contact actions, a scalar contact-load severity indicator is introduced. The indicator combines the concentration of the total normal pressure with the magnitude of the global tangential resultant and is defined as:

$$R_c = w_n \frac{\max_{\Gamma_c} p_n}{\overline{p}_n + \varepsilon_n} + w_q \frac{\sqrt{Q_x^2 + Q_y^2}}{P + \varepsilon_q}, \qquad w_n + w_q = 1, \tag{C17}$$

where $\overline{p}_n$ is the footprint-averaged total normal pressure, P is the normal-force resultant, and Q_x and Q_y are the longitudinal and lateral force resultants. The coefficients w_n and w_q control the relative contributions of pressure concentration and tangential loading, while ε_n and ε_q are small stabilizers. Both terms are calculated from the reconstructed contact-traction field, so R_c serves only as a compact post-processing descriptor and does not introduce an additional contact constitutive law.

For each prescribed combination of contact, speed, and material parameters, the complete transient stress field is independently obtained from the FE-PINN solution. The corresponding combined von Mises stress field is evaluated directly from the reconstructed three-dimensional stress tensor as:

$$\sigma_{\mathrm{vm}}^{\mathrm{comb}}(\mathbf{x}, t; \boldsymbol{\zeta}) = \mathscr{S}_{\mathrm{vm}}[\boldsymbol{\sigma}_{\boldsymbol{\theta}}(\mathbf{x}, t; \boldsymbol{\zeta})], \tag{C18}$$

where $\boldsymbol{\zeta}$ is the scenario vector and $\mathscr{S}_{\mathrm{vm}}[\cdot]$ denotes the three-dimensional von Mises operator defined from all normal and shear stress components. Thus, every parameter combination produces its own time-dependent stress solution.

The vertical strain associated with the same parameter combination is obtained from the symmetric displacement gradient of the reconstructed transient displacement field. Its vertical component is expressed as:

$$\varepsilon_{zz}^{\mathrm{comb}}(\mathbf{x}, t; \boldsymbol{\zeta}) = \mathbf{e}_z^{\mathrm{T}} \boldsymbol{\varepsilon}[\mathbf{u}_{\boldsymbol{\theta}}(\mathbf{x}, t; \boldsymbol{\zeta})] \mathbf{e}_z, \tag{C19}$$

where $\boldsymbol{\varepsilon}[\mathbf{u}_{\boldsymbol{\theta}}]$ is the infinitesimal strain tensor calculated from the reconstructed displacement field, and $\mathbf{e}_z$ is the unit vector in the depth direction.

For domain transfer, a scenario embedding is:

$$\mathbf{z}_e = \mathbf{T}_{\omega}(\boldsymbol{\zeta}), \tag{C20}$$

where $\mathbf{T}_{\omega}$ is an embedding map. The domain-shift covariance matrix is:

$$\mathbf{C}_D = \frac{1}{N_D - 1} \sum_{i=1}^{N_D} \left(\mathbf{z}_{e,i} - \overline{\mathbf{z}}_e\right)\left(\mathbf{z}_{e,i} - \overline{\mathbf{z}}_e\right)^{\mathrm{T}}. \tag{C21}$$

The few-shot calibration error after n_c calibration samples is:

$$e_{\mathrm{cal}}(n_c) = \frac{\|\widehat{\boldsymbol{\phi}}_{n_c} - \boldsymbol{\phi}\|_2}{\|\boldsymbol{\phi}\|_2 + \varepsilon_{\mathrm{cal}}}. \tag{C22}$$

The domain classification matrix is:

$$\mathbf{M}_D = \left[M_{ij}\right], M_{ij} = \Pr(\widehat{d} = j | d = i), \tag{C23}$$

where d is the reference domain label and $\widehat{d}$ is the predicted domain label. The domain-shift contribution of factor j is:

$$\chi_j^D = \frac{\mathrm{Var}(\zeta_j)}{\sum_m \mathrm{Var}(\zeta_m) + \varepsilon_D}. \tag{C24}$$

An invariant-risk objective is:

$$\mathscr{R}_{\mathrm{inv}} = \sum_{d \in \mathscr{D}} \mathscr{R}_d(\boldsymbol{\theta}) + \lambda_{\mathrm{inv}} \sum_{d \in \mathscr{D}} \left\| \nabla_{\boldsymbol{\theta}} \mathscr{R}_d(\boldsymbol{\theta}) - \frac{1}{|\mathscr{D}|} \sum_{m \in \mathscr{D}} \nabla_{\boldsymbol{\theta}} \mathscr{R}_m(\boldsymbol{\theta}) \right\|_2^2. \tag{C25}$$

For robustness analysis, the perturbation-induced response error is:

$$\eta_{\mathrm{rob}} = \frac{\|\mathscr{G}_{\boldsymbol{\theta}}(\boldsymbol{\zeta} + \delta\boldsymbol{\zeta}) - \mathscr{G}_{\boldsymbol{\theta}}(\boldsymbol{\zeta})\|_2}{\|\mathscr{G}_{\boldsymbol{\theta}}(\boldsymbol{\zeta})\|_2 + \varepsilon_{\mathrm{rob}}}. \tag{C26}$$

The noise-sensitivity curve is:

$$e_{\eta}(\alpha_n) = \frac{\|\widehat{\boldsymbol{\phi}}_{\alpha_n} - \boldsymbol{\phi}\|_2}{\|\boldsymbol{\phi}\|_2 + \varepsilon_{\eta}}, \tag{C27}$$

where α_n is the input noise level. The outlier sensitivity is:

$$e_o(\alpha_o) = \frac{1}{N_o} \sum_{i=1}^{N_o} |\widehat{\phi}_i(\alpha_o) - \phi_i|, \tag{C28}$$

where α_o is the outlier ratio. A robust residual penalty is:

$$\rho_\delta(r) = \begin{cases} \frac{1}{2}r^2, |r| \le \delta \\ \delta\left(|r| - \frac{1}{2}\delta\right), |r| > \delta \end{cases}, \tag{C29}$$

where r is a scalar residual and δ is a transition threshold.

The boundary-source coarsening error is:

$$e_c(\alpha_c) = \frac{\|\widehat{\mathbf{t}}_{c,\alpha_c} - \widehat{\mathbf{t}}_c\|_2}{\|\widehat{\mathbf{t}}_c\|_2 + \varepsilon_c}, \tag{C30}$$

where α_c is a source-coarsening ratio.

Material-parameter robustness is assessed by independently re-evaluating the reconstruction operator after perturbing the elastic modulus and Poisson's ratio. Let $\mathscr{G}_{\boldsymbol{\theta}}^{\delta_E,\delta_\nu}$ denote the reconstructed response obtained under relative perturbations δ_E and δ_ν, and let $\mathscr{G}_{\boldsymbol{\theta}}^{0,0}$ denote the corresponding unperturbed response. A normalized material-robustness score is defined as:

$$S_m(\delta_E, \delta_\nu) = \left[1 + \frac{\|\mathscr{G}_{\boldsymbol{\theta}}^{\delta_E,\delta_\nu} - \mathscr{G}_{\boldsymbol{\theta}}^{0,0}\|_2}{\|\mathscr{G}_{\boldsymbol{\theta}}^{0,0}\|_2 + \varepsilon_m}\right]^{-1}. \tag{C31}$$

The norm may be evaluated over the selected reconstructed contact field, internal response field, or a consistently concatenated set of response quantities. A value of S_m close to unity indicates that the perturbation produces only a small change relative to the reference response, whereas a lower value indicates increased material sensitivity.

The contact-radius perturbation error is:

$$e_a(\delta_a) = \frac{\|\widehat{\boldsymbol{\phi}}_{\delta_a} - \boldsymbol{\phi}\|_2}{\|\boldsymbol{\phi}\|_2 + \varepsilon_a}, \tag{C32}$$

where δ_a is the relative perturbation of the contact radius.

Finally, the compound-perturbation recovery error under adaptive loss reweighting is:

$$e_{\text{comp}}^{(k)} = \frac{\|\widehat{\boldsymbol{\phi}}_{\text{comb}}^{(k)} - \boldsymbol{\phi}\|_2}{\|\boldsymbol{\phi}\|_2 + \varepsilon_{\text{comb}}},$$

$$\widehat{\boldsymbol{\phi}}_{\text{comb}}^{(k)} = \frac{1}{N_e}\sum_{m=1}^{N_e} \widehat{\boldsymbol{\phi}}_m^{(k)}, \tag{C33}$$

and the ensemble spread is:

$$s_{\text{ens}}^{(k)} = \sqrt{\frac{1}{N_e - 1}\sum_{m=1}^{N_e} \|\widehat{\boldsymbol{\phi}}_m^{(k)} - \widehat{\boldsymbol{\phi}}^{(k)}\|_2^2}. \tag{C34}$$

Together, these training, transfer, identifiability, scanning, and robustness descriptors allow all reconstructed fields to be evaluated not only by local error but also by physical closure, inverse conditioning, cross-domain transferability, and perturbation stability.

Data availability

Data will be made available on request.

References

Abd El-Hakim, R.T., Kaloop, M.R., El-Badawy, S.M., Wan, H.J., Ali, E.K., 2025. Machine learning-based models for thermal cracking prediction of flexible pavements. Road Mater. Pavement Des. 26 (6), 1287–1314.

Assogba, O.C., Tan, Y., Sun, Z., Lushinga, N., Bin, Z., 2021. Effect of vehicle speed and overload on dynamic response of semi-rigid base asphalt pavement. Road Mater. Pavement Des. 22 (3), 572–602.

Bao, N., Chen, J., Wang, G., Sun, R., Yan, K., 2026. Pseudo-dynamic lateral earth pressure on stabilizing piles in sandy slopes considering arching effect. J. Rock Mech. Geotech. Eng.

Behnke, R., Kaliske, M., 2015. Thermo-mechanically coupled investigation of steady state rolling tires by numerical simulation and experiment. Int. J. Non Linear Mech. 68, 101–131.

Behroozinia, P., Khaleghian, S., Taheri, S., Mirzaeifar, R., 2020. An investigation towards intelligent tyres using finite element analysis. Int. J. Pavement Eng. 21 (3), 311–321.

Bruno, S., Colonnese, S., Scarano, G., Del Serrone, G., Loprencipe, G., 2022. Pavement distress estimation via signal on graph processing. Sensors (Basel, Switzerland) 22.

Cano-Ortiz, S., Pascual-Muñoz, P., Castro-Fresno, D., 2022. Machine learning algorithms for monitoring pavement performance. Autom. Constr. 139, 104309.

Chen, J., Shao, Z., Zhu, H., Chen, Y., Li, Y., Zeng, Z., Yang, Y., Wu, J., Hu, B., 2023. Sustainable interior design: A new approach to intelligent design and automated manufacturing based on Grasshopper. Comput. Ind. Eng. 183, 109509.

Chen, J., Shu, Q., Lu, Y., Zhang, Y., Wang, Y., 2025. QCTF: A Quantized communication and transferable fusion framework for multi-agent collaborative perception. IEEE Trans. Intell. Transp. Syst. 26 (10), 15013–15027.

Dehnad, M.H., Yazdi, A., 2024. A review of numerical and experimental studies on hydroplaning of vehicles in motion on road surfaces. Results Eng. 23, 102438.

Deng, T., Wang, S., Cheng, D., Zheng, L., Ren, L., 2025. Effects of driving conditions on tire hydroplaning performance. Lubricants 13 (2), 76.

Elseifi, M.A., Al-Qadi, I.L., Yoo, P.J., 2006. Viscoelastic modeling and field validation of flexible pavements. J. Eng. Mech. 132 (2), 172–178.

Fahad, M., Bektas, N., 2025. Data-driven pavement performance: machine learning-based predictive models. Appl. Sci. 15 (7), 3889.

Feng, D., 2025. Multi-scale algorithm for controllable virtual aggregate generation in mesoscale modeling. Int. J. Mech. Sci. 308, 110978.

Feng, D., 2025. A compactor-soil coupling model considering mechanical inertia and its delayed feedback active suspension control. Int. J. Non Linear Mech. 179, 105245.

Feng, D., 2026. Spectral contact networks for granular base load spreading. Int. J. Mech. Sci. 326, 111914.

Feng, D., 2026. A DEM-based particle–force chain informatics framework for data-driven evaluation of pavement pre-compaction. Adv. Eng. Inf. 71, 104402.

Feng, D., 2026. Elastic tailoring of particulate composites via an auxetic spherical interphase and particle-size distribution effects. Mech. Mater. 221, 105805.

Feng, D., 2026. A controllable domain-warped multifractal implicit-radius algorithm for generation of simulation-ready virtual aggregates. Adv. Eng. Softw. 219, 104193.

Feng, D., 2026. A novel four-degree-of-freedom compactor–soil coupling model. Nonlinear Dyn. 114 (8).

Feng, D., 2027. A boundary element method (BEM)-enhanced physics-informed neural network (PINN) framework for thin-walled geocell-reinforced geotechnical foundations. Comput. Geotech. 201, 108588.

Feng, D., Guan, J., Fu, C., Hu, Y., Otto, F., Hernandez, A.G., et al., 2026. Augmentation of 3D virtual aggregate database using deep convolutional Wasserstein generative adversarial networks. Adv. Eng. Inf. 69, 103994.
Feng, D., Fu, C., Awed, A.M., Hernandez, A.G., Liu, P., 2026. A multiscale framework for simulating the indirect tensile response of asphalt mixtures combining DEM and FEM. Powder Technol. 483, 122833.
Feng, D., Fu, C., Zheng, K., Wang, T., Wang, C., 2026. Numerical framework for asphalt pre-compaction optimization using a coarse-graining discrete element method (DEM). Powder Technol. 478, 122486.
Feng, D., Fu, C., Liu, P., 2026. A modified Johnson-Kendall-Roberts contact model for pavement engineering: Consideration of time-dependent surface energy. Powder Technol. 468, 121701.
Fwa, T.F., 2021. Determination and prediction of pavement skid resistance–connecting research and practice. J. Road Eng. 1, 43–62.
Gong, Z., Miao, Y., Lantieri, C., 2024. Review of research on tire–pavement contact behavior. Coatings 14 (2), 157.
Guan, J., Zhou, X., Liu, L., Ran, M., Yan, Y., 2022. Investigation of tri-axial stress sensing and measuring technology for tire-pavement contact surface. Coatings 12 (4), 491.
Hernandez, J.A., Al-Qadi, I.L., 2017. Tire–pavement interaction modelling: hyperelastic tire and elastic pavement. Road Mater. Pavement Des. 18 (5), 1067–1083.
Huang, J., Li, X., Zhang, J., Sun, Y., Ren, J., 2022. Determining the Rayleigh damping parameters of flexible pavements for finite element modeling. J. Vib. Control 28 (21–22), 3181–3194.
Huang, Y., Liu, J., Yang, X., Liu, Z., 2025. Characterization of permanent deformation of asphalt pavement with rigid base. Constr. Build. Mater. 460, 139808.
Jia, B., Wang, S., Huang, Z., 2026. A multi-grid descriptor method for 3D digital rock microstructure reconstruction. Comput. Geosci. 30 (4).
Justo-Silva, R., Ferreira, A., Flintsch, G., 2021. Review on machine learning techniques for developing pavement performance prediction models. Sustainability 13 (9), 5248.
Kingma, Diederik P., Ba, Jimmy, 2014. Adam: A Method for Stochastic Optimization. International Conference on Learning Representations.
Lee, S., Kwak, J., Kim, H., Lee, J., 2013. Properties of roadway particles from interaction between the tire and road pavement. Int.J Automot. Technol. 14 (1), 163–173.
Liu, P., Wang, D., Oeser, M., 2015. Application of semi-analytical finite element method coupled with infinite element for analysis of asphalt pavement structural response. J. Traffic Transporta. Eng. (English Edition) 2 (1), 48–58.
Liu, H., Cai, Y., Zhong, Y., Pan, B., 2021. Thermo-hydro-mechanical response of a multi-layered pavement with imperfect interface based on dual variable and position method. App. Math. Model. 99, 704–729.
Liu, Q., Pei, J., Wang, Z., Hu, D., Huang, G., Meng, Y., et al., 2024. Analysis of tire-pavement interaction modeling and rolling energy consumption based on finite element simulation. Constr. Build. Mater. 425, 136101.
Liu, S., Lin, R., Jia, Y., Wu, Q., Chen, C., 2026. Competitive crack evolution in flawed rocks under thermal–mechanical coupling: a tangential stress and displacement decomposition approach. J. Rock Mech. Geotech. Eng.
Löwer, J., Wagner, P., Unrau, H.-J., Bederna, C., Gauterin, F., 2020. Physical Model of Tire-Road Contact under Wet Conditions. Tribol. Lett. 68 (1).
Luo, Y., Xu, Y., Sun, Z., Wang, L., Li, Y., Wang, H., 2025. Tire-pavement contact behavior: a simplified model for predictive surface contact analysis. Constr. Build. Mater. 491, 142649.
Lv, H., Li, C., Dai, J., Zhang, Y., Fan, Z., Tan, Y., Wang, D., Xie, B., 2025. Lightweight framework for underground pipeline recognition and spatial localization based on multi-view 2D GPR images. IEEE Trans. Geosci. Remote Sens. 63, 5110115.
Ma, X., Quan, W., Si, C., Dong, Z., Dong, Y., 2021. Analytical solution for the mechanical responses of transversely isotropic viscoelastic multi-layered asphalt pavement subjected to moving harmonic load. Soil Dyn. Earthq. Eng. 147, 106822.
Michael, M., Vogel, F., Peters, B., 2015. DEM–FEM coupling simulations of the interactions between a tire tread and granular terrain. Comput. Methods Appl. Mech. Eng. 289, 227–248.
Mirzaiyan, D., Sarzaeim, P., Dave, E.V., 2025. Enhanced pavement design process to incorporate moisture management geotextiles: a comprehensive mechanical-hydro-mechanical modeling and design integration (part B). Transp. Geotech. 55, 101707.
Mizutani, D., Kurabe, A., Saito, T., Nakazato, Y., Nakamura, T., Otake, Y., 2026. Pavement performance prediction via a tabular foundation model. Comput. Aided Civ. Inf. Eng. 49, 100097.
Nian, T., Li, S., Li, P., Li, J., Han, Z., Xue, S., 2023. Mechanical response of interlayer structural shear performance of asphalt pavement with functional layer considering interlayer contact state. Case Stud. Constr. Mater. 18, e01934.
Park, D.-W., Martin, A.E., Masad, E., 2005. Effects of nonuniform tire contact stresses on pavement response. J. Transp. Eng. 131 (11), 873–879.
Rahman, S., Ahmed, A., Erlingsson, S., 2025. Responses of a thin flexible pavement loaded with tires of various dimensions and configurations. Road Mater. Pavement Des. 26 (sup1), 680–699.
Raissi, M., Perdikaris, P., Karniadakis, G.E., 2019. Physics-informed neural networks: a deep learning framework for solving forward and inverse problems involving nonlinear partial differential equations. J. Comput. Phys. 378, 686–707.
Rasol, M., Schmidt, F., Ientile, S., Adelaide, L., Nedjar, B., Kane, M., et al., 2021. Progress and monitoring opportunities of skid resistance in road transport: a critical review and road sensors. Remote Sens. (Basel) 13 (18), 3729.
Sadiq, M.F., Velasquez, R., Aydin, C., Cetin, B., Izevbekhai, B., 2025. Influence of initial stiffness and foundation uniformity on pavement performance. Int. J. Pavement Eng. 26 (1).
Shahid, C.S., Yusoff, N.I.M., Khahro, S.H., Zamzuri, Z.H., Widyatmoko, I., Malik, M.A., et al., 2026. Surrogate-based probabilistic modeling of pavement deterioration under traffic-induced stress. Alex. Eng. J. 138, 37–50.
Shen, K., Wang, H., 2024. Development of high-efficient asphalt pavement modeling software for digital twin of road infrastructure. Adv. Eng. Softw. 198, 103786.
Sheng, J., Liu, L., Liu, Z., Su, Y., Li, L., 2025. Advanced machine learning for predicting asphalt mixture performance: a data-driven approach with model interpretation. Int. J. Pavement Res Technol.
Stefanelli, R., Mavros, G., Martínez-García, M., Knowles, J., Timpone, F., Farroni, F., 2026. Efficient road roughness characterization using Gaussian process regression and 2D imaging. Measurement 277, 121590.
Wang, T., Dong, Z., Xu, K., Ullah, S., Wang, D., Li, Y., 2022. Numerical simulation of mechanical response analysis of asphalt pavement under dynamic loads with non-uniform tire-pavement contact stresses. Constr. Build. Mater. 361, 129711.
Wang, N., Chu, L., Fwa, T.F., 2024. Improved method for evaluation of effect of pavement microtexture on vehicle hydroplaning speed. Constr. Build. Mater. 451, 138727.
Wang, L.e., Zhang, L., Chen, H., Zhang, T., Yi, J., Zhang, J., et al., 2026. Combined effects of anchor geometry and soil spatial variability on the probabilistic pullout capacity of helical anchors. Comput. Geotech. 200, 108482.
Wollny, I., Behnke, R., Villaret, K., Kaliske, M., 2016. Numerical modelling of tyre–pavement interaction phenomena: coupled structural investigations. Road Mater. Pavement Des. 17 (3), 563–578.
Wu, Z., Hu, S., Zhou, F., 2014. Prediction of stress intensity factors in pavement cracking with neural networks based on semi-analytical FEA. Expert Syst. Appl. 41 (4), 1021–1030.
Xie, S., Hu, A., Xiao, Z., Mariani, S., Della, V.G., 2024. PINN-based approach to the consolidation analysis of visco-elastic soft soil around twin tunnels. Tunn. Undergr. Space Technol. 153, 105981.
Xie, S., Min, M., Pu, H., Song, D., Chen, X., Dias, D., 2026. Two-dimensional nonlinear consolidation of soft soils around tunnels considering soil arching effect: an efficient lagged-coefficient ADI finite difference approach. Comput. Geotech. 198, 108266.
Xie, S., Xia, C., Pu, H., Chen, X., Hu, A., Mariani, S., 2026. PINN–FEM-based approach to hydro-mechanical analysis of tunnels in anisotropic strata. Acta Geotech.
Xu, C., Cao, B.T., Yuan, Y., Meschke, G., 2024. A multi-fidelity deep operator network (DeepONet) for fusing simulation and monitoring data: Application to real-time settlement prediction during tunnel construction. Eng. Appl. Artif. Intel. 133, 108156.
Xu, Q., Zhang, C., Geng, S., Wang, S., Li, J., Liu, J., et al., 2025. An explainable ensemble learning framework for flexible pavement roughness prediction under multi-climate stressors. Case Stud. Constr. Mater. 23, e05402.
Yang, G., Jiang, Y., Wang, S., Chen, K., 2025. VinsFusion-line: Binocular vision inertial navigation real-time SLAM system based on line features. Cybern. Syst. 57, 350–375.
Yao, S., Li, Z., Guan, R., Xia, M., Hu, F., Cao, K., Xu, S., Zhu, X., Liu, R.W., Ding, W., 2026. GIF-Calib: Geometry-intensity fusion for 4D radar-camera calibration in autonomous driving vehicles. Inf. Fusion 136, 104510.
Yun, D.i., Liu, Y., Tang, C., Qian, F., Gao, J., Xiao, S., et al., 2026. Boundary characterization at rubber–pavement three-dimensional contact interfaces via in-situ computed tomography. Constr. Build. Mater. 524, 146316.
Zhao, J., Wang, H., 2022. Dynamic pavement response analysis under wide-base tyre considering vehicle-tyre–pavement interaction. Road Mater. Pavement Des. 23 (7), 1650–1666.
Zhao, L., Zhao, H., Cai, J., 2024. Tire-pavement friction modeling considering pavement texture and water film. Int. J. Transp. Sci. Technol. 14, 99–109.
Zheng, B., Tang, J., Chen, J., Zhao, R., Huang, X., 2022. Investigation of adhesion properties of tire-asphalt pavement interface considering hydrodynamic lubrication action of water film on road surface. Materials (Basel, Switzerland) 15.
Zheng, K., Xie, N., Jin, J., Liu, P., 2025. Environmentally friendly lead-free piezoelectric ceramics as pavement sensing element: a multi-scale finite element perspective. Case Stud. Constr. Mater. 23, e05174.
Zheng, K., Gao, T., Liu, P., 2026. A multi-scale framework for the design of lead-free potassium sodium niobate pavement sensor arrangements for vehicle classification. Measurement 271, 120999.